

INTENSE ELECTROSTATIC WAVES NEAR  
THE UPPER HYBRID RESONANCE FREQUENCY

by

William Steven Kurth

An Abstract

Of a thesis submitted in partial fulfillment  
of the requirements for the degree of  
Doctor of Philosophy in Physics  
in the Graduate College of  
The University of Iowa

May, 1979

Thesis supervisor: Professor Donald A. Gurnett

## ABSTRACT

Plasma wave measurements using instruments on the IMP 6 and Hawkeye 1 satellites are utilized in a study of very intense electrostatic waves near the upper hybrid resonance frequency in the region just outside the plasmapause. These intense plasma wave events have electric field strengths of  $\sim 1$  to  $20 \text{ mV m}^{-1}$  and are among the most intense waves seen in the earth's magnetosphere. Detailed studies of more than 140 of these intense electrostatic disturbances reveal that the events occur at all local times and at magnetic latitudes varying from the equator to as high as  $50^\circ$ . The polarization of these waves is such that the wave electric field vector is oriented perpendicular to the geomagnetic field. In most cases the center frequency of the intense waves appears to correspond to an  $(n + 1/2)f_g^-$  harmonic near the upper hybrid resonance frequency.

A survey of plasma measurements made simultaneously using the Hawkeye 1 LEPEDEA shows that the occurrence of the intense electrostatic waves is not strongly correlated with the intensities of  $\sim 1$  to  $20 \text{ keV}$  electrons, but that specific details of the hot electron distribution function are directly related to the wave turbulence. All events at magnetic latitudes less than about  $10^\circ$  show strong pitch angle anisotropy with the greatest electron

intensities at  $\alpha \approx 90^\circ$ . The hot electron distribution function,  $f(v_\perp, v_\parallel)$ , is described for a few events showing two sources of free energy: a temperature anisotropy and a loss-cone distribution. One event shown suggests that a bump-on-tail in  $v_\perp$  may also contribute free energy in some cases. A generation mechanism is proposed which is founded in the theory of electrostatic multi-cyclotron instabilities. Observations are compared with the theory which suggests that a nonconvective instability in the  $(n + 1/2)f_g^-$  band including the cold upper hybrid resonance frequency qualitatively reproduces observations of the intensifications near the upper hybrid resonance frequency for a range of plasma parameters.

The implications of the presence of the intense upper hybrid resonance waves on plasmas in the magnetosphere are discussed. In addition, the presence of large electrostatic waves may be related to the terrestrial radio spectrum. Evidence is presented which suggests the intense electrostatic waves may be a source of non-thermal continuum radiation.

Abstract approved: \_\_\_\_\_

Thesis supervisor

Professor, Physics and Astronomy  
Title and department

Feb 9, 1979  
Date

INTENSE ELECTROSTATIC WAVES NEAR  
THE UPPER HYBRID RESONANCE FREQUENCY

by

William Steven Kurth

A thesis submitted in partial fulfillment  
of the requirements for the degree of  
Doctor of Philosophy in Physics  
in the Graduate College of  
The University of Iowa

May, 1979

Thesis supervisor: Professor Donald A. Gurnett



Graduate College  
The University of Iowa  
Iowa City, Iowa

CERTIFICATE OF APPROVAL

PH.D. THESIS

This is to certify that the Ph.D. thesis of

William Steven Kurth

has been approved by the Examining Committee  
for the thesis requirement for the Doctor of  
Philosophy degree in Physics at the May, 1979  
graduation.

Thesis committee: Donald Burnett  
Thesis supervisor

L. A. Frank  
Member

Stanley D. Sawha  
Member

Alexander Feyer  
Member

Kurt Elzinger  
Member

## ACKNOWLEDGMENTS

This work was possible only with the cooperation and contributions of data and advice of a large number of IMP 6, Hawkeye 1, and ISEE investigators. I thank Professor D. A. Gurnett for the use of plasma wave measurements from IMP 6, Hawkeye 1, and ISEE-1 and -2, and Professor L. A. Frank for the use of plasma measurements from LEPEDEA instruments on Hawkeye and ISEE-1 and -2. I would also like to thank Drs. N. F. Ness and D. H. Fairfield for magnetic field measurements from the NASA/GSFC magnetometer on IMP 6, Professor J. A. Van Allen for magnetic field measurements from the Hawkeye 1 magnetometer, and Dr. C. T. Russell for magnetometer measurements from ISEE-1 and -2. I am especially indebted to Dr. J. D. Craven for his persistence and enthusiasm in the analysis and interpretation of the Hawkeye LEPEDEA measurements. Special appreciation is also extended to Dr. M. Ashour-Abdalla for the time and effort which she graciously devoted to this project and for the knowledge which I have gained through this collaboration. I also wish to thank Professor C. F. Kennel for his advice and support of this work.

I must express my gratitude to Professor D. A. Gurnett for his guidance and support in this thesis. His instruction and the

example he has set for me are invaluable as are the experiences I have gained as his student over the past several years.

I wish to thank Joyce Chrisinger and Jeana Wonderlich for their artistry and efficiency in producing the illustrations for this thesis. I am also deeply indebted to Kathy Goodner for accurately and efficiently typing the manuscript. I commend Richard West for the masterful darkroom work he provided for many of the illustrations and thank him for his continual support in producing finished data products for illustrations and analysis. I also thank W. Livesey for his industry in plotting contours in Figure 21. I appreciate the comments and suggestions of Drs. D. D. Barbosa and R. R. Shaw. I am particularly appreciative of Dr. R. R. Anderson not only for his support of this endeavor, but also his unfailing friendship of many years.

The support of my family, Susan, Steven, and Brandi, has been essential to this work and I am forever indebted to them for the understanding they have shown throughout. To my wife, Susan, who has never faltered in her love and encouragement, I dedicate this thesis.

The research at the University of Iowa was supported by the National Aeronautics and Space Administration through Contracts NAS1-13129, NAS5-11074, NAS5-20093, NAS5-20094, and Grant NGL-16-001-043, and by the U. S. Office of Naval Research through Contract N00014-76-C-0016. The research at the University of California, Los Angeles was supported by NASA NGL-05-007-190 and NSF ATM-76-13792.

## ABSTRACT

Plasma wave measurements using instruments on the IMP 6 and Hawkeye 1 satellites are utilized in a study of very intense electrostatic waves near the upper hybrid resonance frequency in the region just outside the plasmapause. These intense plasma wave events have electric field strengths of  $\sim 1$  to  $20 \text{ mV m}^{-1}$  and are among the most intense waves seen in the earth's magnetosphere. Detailed studies of more than 140 of these intense electrostatic disturbances reveal that the events occur at all local times and at magnetic latitudes varying from the equator to as high as  $50^\circ$ . The polarization of these waves is such that the wave electric field vector is oriented perpendicular to the geomagnetic field. In most cases the center frequency of the intense waves appears to correspond to an  $(n+1/2)f_g^-$  harmonic near the upper hybrid resonance frequency.

A survey of plasma measurements made simultaneously using the Hawkeye 1 LEPDEA shows that the occurrence of the intense electrostatic waves is not strongly correlated with the intensities of  $\sim 1$  to  $20 \text{ keV}$  electrons, but that specific details of the hot electron distribution function are directly related to the wave turbulence. All events at magnetic latitudes less than about  $10^\circ$  show strong pitch angle anisotropy with the greatest electron

intensities at  $\alpha \approx 90^\circ$ . The hot electron distribution function,  $f(v_\perp, v_\parallel)$ , is described for a few events showing two sources of free energy: a temperature anisotropy and a loss-cone distribution. One event shown suggests that a bump-on-tail in  $v_\perp$  may also contribute free energy in some cases. A generation mechanism is proposed which is founded in the theory of electrostatic multi-cyclotron instabilities. Observations are compared with the theory which suggests that a nonconvective instability in the  $(n + 1/2)f_g^-$  band including the cold upper hybrid resonance frequency qualitatively reproduces observations of the intensifications near the upper hybrid resonance frequency for a range of plasma parameters.

The implications of the presence of the intense upper hybrid resonance waves on plasmas in the magnetosphere are discussed. In addition, the presence of large electrostatic waves may be related to the terrestrial radio spectrum. Evidence is presented which suggests the intense electrostatic waves may be a source of non-thermal continuum radiation.

## TABLE OF CONTENTS

	Page
LIST OF PLATES . . . . .	viii
LIST OF FIGURES . . . . .	xi
I. INTRODUCTION . . . . .	1
II. DESCRIPTION OF INTENSE ELECTROSTATIC WAVES BEYOND THE PLASMAPAUSE . . . . .	7
A. Spectral Properties . . . . .	7
B. Regions of Occurrence . . . . .	10
C. Identification of the Wave Mode . . . . .	16
III. PLASMA SIGNATURES ASSOCIATED WITH INTENSE ELECTROSTATIC WAVES . . . . .	24
A. Survey of Plasma Measurements Gained During Intense Electrostatic Wave Events . . . . .	24
B. Electron Distribution Functions Measured During Intense Electrostatic Wave Events . . . . .	29
IV. A COMPARISON OF INTENSE ELECTROSTATIC WAVES OBSERVED NEAR $f_{UHR}$ WITH LINEAR INSTABILITY THEORY . . . . .	35
A. Review of the Theory of Electrostatic Waves Above the Electron Gyrofrequency . . . . .	35
B. Comparison of the Theory of Electrostatic Multi- Harmonic Emissions With Observations of Intense Waves Near $f_{UHR}$ . . . . .	41
V. DISCUSSION . . . . .	54
A. Intense Electrostatic Waves as a Source of Nonthermal Continuum Radiation . . . . .	54
B. The Implication of Intense Electrostatic Waves for the Distributions of Magnetospheric Plasmas . . . . .	58

	Page
VI. SUMMARY AND CONCLUSIONS . . . . .	60
REFERENCES . . . . .	62
APPENDIX A: POLARIZATION DETERMINATION . . . . .	66
APPENDIX B: PLATES . . . . .	75
APPENDIX C: FIGURES . . . . .	86

# LIST OF PLATES

	Page
Plate 1	
A typical example of intense waves near $f_{UHR}$	
can be seen at about 2110 UT. This event occurs	
at about 12.7 hours magnetic local time and at	
a magnetic latitude of $6.9^\circ$ . The band at $f_{UHR}$	
can be traced from within the plasmasphere at	
high frequencies out through the plasmopause and	
into the outer magnetosphere near the lower cut-	
off of the nonthermal continuum radiation. Also	
seen are weak, diffuse electrostatic bands between	
harmonics of the gyrofrequency, below the upper	
hybrid band. . . . .	76
Plate 2	
A plasma energy-time spectrogram obtained during	
the high latitude wave event shown in Figure 11.	
While incomplete pitch angle coverage does not	
allow an analysis of pitch angle anisotropy,	
the time correlation of the electron intensities	
at about 1 keV with the intense electrostatic	
waves seen in Figure 11 is very good. . . . .	78



- Plate 3      A plasma energy-time spectrogram obtained during the intense electrostatic wave event shown in Figure 12. Since this event lies at the equator, nearly complete sampling in pitch angle is possible. Note the very anisotropic electron signature at about 1 keV between 2200 and 2210 UT. . . . . 80
- Plate 4      A demonstration of the intensification near  $f_{\text{UHR}}$  at  $(n + 1/2)f_g^-$  bands. In this outbound pass of the ISEE 1 satellite one can see intensifications as each of the first five  $(n + 1/2)f_g^-$  bands approaches  $f_{\text{UHR}}$  near the lower edge of the non-thermal continuum radiation. This pass is at about 6 hours magnetic local time and near 20° magnetic latitude. . . . . 82
- Plate 5      A striking example showing an intensification as the band at  $f_{\text{UHR}}$  merges with the  $3f_g^-/2$  band. Notice, also, the intensification in the non-thermal continuum radiation at about  $7 R_E$  at the same frequency as the intense electrostatic waves,

suggesting a possible relation between the two.

This intense event occurs at 3.8 hours MLT and

at 38.1° magnetic latitude. . . . . 84

## LIST OF FIGURES

		Page
Figure 1	<p>An example of intense electrostatic waves detected just at the plasmapause by the University of Iowa plasma wave instrument onboard the IMP 6 satellite. The solid black areas have a vertical extent proportional to the logarithm of the average electric field strength during 5.11 second averaging intervals. The dots indicate the peak electric field detected during the same interval. The dashed line labeled <math>f_{UHR}</math> illustrates the expected trend of the upper hybrid frequency as a function of time if one assigns a frequency scale to the ordinate so that the baseline of each channel defines that channel's frequency on the scale. . . . .</p>	87
Figure 2	<p>The electric field spectrum of the intense electrostatic wave event shown in Figure 1. Notice the intense waves are sharply peaked at 56.2 kHz and the peak-to-average ratio is about</p>	

30, indicating large fluctuations in intensity  
on a time scale of a few seconds. . . . . 89

Figure 3 Another example of intense waves as measured by  
the IMP 6 instrument. This event is approxi-  
mately  $0.5 R_E$  outside the plasmapause. The  
magnetic spectrum analyzer data shown in the  
lower panel indicate the presence of a rela-  
tively small magnetic component for this event.  
The ratio of the electric-to-magnetic field  
energy densities in this example is about  
1600. . . . . 91

Figure 4 This is a display of all the intense electro-  
static wave events ( $|\vec{E}| \geq 1 \text{ mV m}^{-1}$ ) detected  
during over five and one-half years of obser-  
vations with the Hawkeye 1 and IMP 6 satellites.  
Each of four quadrants in magnetic local time  
are rotated into the noon-midnight and dawn-  
dusk magnetic meridian planes shown here.  
Notice the wide range of latitudes at which  
the intense waves are detected. The events  
also occur at all local times. . . . . 93

Figure 5 A series of histograms showing the number of intense electrostatic wave events with electric field amplitudes greater than about  $1 \text{ mV m}^{-1}$  as a function of radial distance. Each histogram represents the events detected at each of six different frequencies. The histogram labeled " $\sim 10 \text{ kHz}$ " comprises events from IMP 6's  $10 \text{ kHz}$  channel and Hawkeye's  $13.3\text{-kHz}$  channel and the histogram labeled " $\sim 17 \text{ kHz}$ " combines the events from the  $16.5\text{-}$  and  $17.8\text{-kHz}$  channels from IMP 6 and Hawkeye 1, respectively. Notice the trend towards lower frequencies at greater distances, implying that the instability is closely related to either  $f_{\text{UHR}}$  or  $f_{\text{p}}^{\sim}$ . . . . . 95

Figure 6 A display of plasma wave measurements of an intense wave event detected by Hawkeye 1 with a summary of polarization measurements superimposed over the data. The spin modulation seen in many of the features has been analyzed to determine the orientation of the wave electric field with respect to the geomagnetic field. The shaded regions are regions of frequency and

time where all waves are polarized such that  $\vec{E} \parallel \vec{B}_0$ , consistent with the polarization of nonthermal continuum radiation. The unshaded region indicates frequencies and times, including the intense electrostatic event at 31.1 kHz, when waves with measurable polarization have electric fields oriented perpendicular to  $\vec{B}_0$ . This polarization unambiguously identifies  $f_{\text{UHR}}$  as the characteristic frequency of the intense waves (see text). The hatched region consists of whistler-mode turbulence. . . . . 97

Figure 7 A display of plasma wave measurements of the same event shown in Figure 6, but overlaid with lines at  $f_g^-$  and the lower order  $(n + 1/2)f_g^-$  bands using the ordinate as a frequency scale. The values of  $f_g^-$  are calculated from the measured magnetic field provided by the magnetometer onboard Hawkeye 1. Notice that a large number of the features present in this complex region lie at or near the  $(n + 1/2)f_g^-$  harmonics. In particular, the intense event at 31.1 kHz lies directly at the  $7f_g^-/2$  harmonic . . . . . 99

- Figure 8      A demonstration of the variation of measured electric field strength as a function of  $\delta$ , the angle of the electric dipole antenna. The sketch in the upper portion of the figure demonstrates the relative orientation of the geomagnetic field,  $\vec{B}_0$ , the spacecraft spin axis,  $\vec{\omega}$ , and the electric field to be measured,  $\vec{E}_0$ . A general description of the polarization determination is found in Appendix A. . . . . 101
- Figure 9      A high-resolution frequency-time spectrogram of intense electrostatic waves which occur not only at an  $(n + 1/2)f_g^-$  harmonic, but also near  $f_{UHR}$ . The gyrofrequency for this event is about 1.9 kHz and  $f_{UHR}$  (using the lower frequency cutoff of the continuum radiation for  $f_p^-$ ) is about 15.2 kHz. . . . . 103
- Figure 10     A high-resolution frequency-time spectrogram of intense electrostatic waves detected by the Hawkeye plasma wave receiver. Notice the banded structure of the event at frequencies greater than  $f_g^-$ . The waves are most intense when the

electric dipole antenna is oriented perpendicular to the measured geomagnetic field. Hence, the wave electric field is nearly perpendicular to  $\vec{B}_0$ . . . . . 105

Figure 11 A high latitude intense electrostatic wave event to be compared to the plasma measurements shown in Plate 2. The time correlation between the presence of the intense waves in the 17.8-kHz channel and electron intensities near 1 keV is very good. . . . . 107

Figure 12 An intense electrostatic wave event at 100 kHz located near the magnetic equator. The energy-time spectrogram obtained from plasma measurements during this event is shown in Plate 3. . . . 109

Figure 13 The electron velocity distribution measured during the intense wave event illustrated in Figure 14. Notice the loss cone at small pitch angles, and the temperature anisotropy. The area to the left of the dashed line through contours of constant  $f(v_{\perp}, v_{\parallel})$  is a region of small  $v_{\perp}$  for which the plasma analyzer responses are  $< 100$  counts (sec) $^{-1}$ . . . . . 111



	Page
Figure 14	An electrostatic wave event for which an electron velocity distribution has been measured and shown in Figure 13. The intense signal of interest occurs in the 17.8-kHz channel between about 0415 and 0435 UT. . . . . 113
Figure 15	An electron velocity distribution for the event shown in Figure 16 which shows a very weak loss cone and also is anisotropic. The dashed line is the 100 count (sec) <sup>-1</sup> contour. . . . . 115
Figure 16	An electrostatic wave event for which an electron velocity distribution has been measured and shown in Figure 15. A high resolution frequency-time spectrogram obtained during this event is shown in Figure 10. . . . . 117
Figure 17	A model loss-cone distribution (solid lines) and the measured response of a detector with finite width (dashed lines). Notice the qualitative similarities between the dashed contours and the contours at small pitch angles shown in Figures 13 and 15. . . . . 119

- Figure 18     An electron distribution function exhibiting a weak loss-cone distribution and a temperature anisotropy. The wave event corresponding to this distribution function is shown in Figure 19. The dashed line is the 100 counts (sec)<sup>-1</sup> contour. . . . . 121
- Figure 19     The intense electrostatic wave event for which an electron velocity distribution has been measured and shown in Figure 18. This event, near 2345 UT in the 100-kHz channel, exhibits extreme fluctuations in amplitude on a time scale of minutes. . . . . 123
- Figure 20     The electron distribution function for the wave event shown in Figure 12. The dashed lines are contours of 100 and 50 counts (sec)<sup>-1</sup>. This distribution function is, perhaps, suggestive of a bump-on-tail distribution at  $v_{||} = 0$ . The function also shows a temperature anisotropy. . . . 125
- Figure 21     Regions of nonconvective instability for the first four harmonic bands above  $f_g^-$ . Notice that

for large ( $\geq 1.5$ )  $n_c/n_h$  and sufficiently large  $f_{UHC}$  a single band (the band including  $f_{UHC}$ ) can become nonconvectively unstable. . . . . 127

Figure 22 The electron velocity distribution averaged over pitch angles  $70^\circ < \alpha \leq 90^\circ$  during the intense electrostatic wave event illustrated in Plate 5. Notice that there are two features which might be suggestive of a free energy source for the waves in Plate 5. The features persist from  $\alpha \approx 20^\circ$  through  $\alpha \approx 160^\circ$ . . . . . 129

Figure 23 A demonstration of the qualitative agreement between linear instability theory and observations of intense electrostatic waves near  $f_{UHR}$ . The upper panel is the measured wave spectrum during the intense wave event shown in Plate 1. Notice the weak growth in the lower three bands and the intense peak in the fourth band. The lower panel shows calculations of the maximum spatial growth rate as a function of frequency when  $f_{UHC}$  is in the fourth band. Notice there is relatively weak

convective growth in the lower 3 bands, but the fourth band is nonconvectively unstable. The growth rates shown near the peak of the fourth band are only representative since for a nonconvective instability  $v_g$  goes to zero and  $K_i$  goes to infinity. . . . . 131

Figure 24 A demonstration of an intense electrostatic wave event as a local, compact source of nonthermal continuum radiation. Power flux plotted as a function of radial distance from the earth in the center panel does not show the  $R^{-2}$  dependence expected for a source centered at the earth. However, the plot of power flux as a function of the distance from the intense event centered at  $4.3 R_E$  shows a definite  $(R-R')^{-2}$  dependence. . . 133

## I. INTRODUCTION

This thesis describes very intense electrostatic waves occurring just beyond the plasmopause at frequencies close to the local upper hybrid resonance frequency,  $f_{\text{UHR}}$  ( $f_{\text{UHR}}^2 = (f_p^-)^2 + (f_g^-)^2$  where  $f_p^-$  and  $f_g^-$  are the electron plasma frequency and gyrofrequency, respectively). The importance of these waves is accentuated by their large amplitudes, ranging from about 1 to 20 mV m<sup>-1</sup>, making them some of the most intense waves detected within the magnetosphere of the earth.

Weaker bands of electrostatic waves in the magnetosphere near  $f_{\text{UHR}}$  have been studied previously. Gurnett and Shaw [1973], Mosier et al. [1973], Shaw and Gurnett [1975] and Hubbard and Birmingham [1978a,b] have discussed bands of electrostatic emission at or just outside the plasmopause. The frequencies of those bands varied directly with upper hybrid resonance frequency over a region extending from just inside the plasmopause, across the abrupt decrease in plasma density (frequency) at the plasmopause, and into the outer magnetosphere. This signature appeared in about two-thirds of the IMP 6 plasmopause crossings. The band near  $f_{\text{UHR}}$  at the plasmopause was identified as upper hybrid resonance noise (in the terminology of Gurnett and Shaw [1973]). Outside the plasmopause diffuse electrostatic bands and narrow-band electrostatic noise were

identified with emission frequencies between harmonics of  $f_g^-$  [Shaw and Gurnett, 1975].

The intense electrostatic waves reported in this thesis are probably related to one or more of the bands discussed by Shaw and Gurnett [1975]. In fact, the intense bands studied here often appear to be very intense upper hybrid resonance noise. It is significant that Shaw and Gurnett have suggested the possibility of two distinct populations of events distinguishable by intensity. Evidence for the two populations is presented in their Figure 7 by means of a histogram for the number of electrostatic noise bands at 31.1 kHz as a function of peak electric field spectral density. The primary peak in occurrence frequency is located at about  $10^{-15} \text{ V}^2 \text{ m}^{-2} \text{ Hz}^{-1}$ , with a small secondary peak located near  $10^{-9} \text{ V}^2 \text{ m}^{-2} \text{ Hz}^{-1}$ . The intensities of the bands contributing to the secondary peak are similar to the intensities of the waves reported in this thesis.

In this thesis we treat only the most intense electrostatic waves found near the plasmopause and consider them to represent a class of waves unique from the low intensity bands discussed by Shaw and Gurnett [1975], even though the very intense waves are similar in many respects to the lower amplitude waves. It is useful to present at this early point an archetype of the intense wave events of interest. Plate 1 illustrates many of the features of the intense waves and will be referred to often throughout the thesis. The data comprising this illustration are from the ISEE 1 sweep-frequency-receiver organized to show relative wave

amplitude as a function of frequency and time. Dark blue regions indicate the lowest amplitude waves while red indicates wave amplitudes four to five orders of magnitude greater than the receiver threshold. The intense band at about 30 kHz at 2110 UT is indicative of the waves treated in this work. The peak amplitude of this event is approximately  $7 \text{ mV m}^{-1}$  and is sufficiently large to saturate the receiver resulting in the yellow rectangular area immediately surrounding the event. The intense band coincides with the upper hybrid resonance band which can be traced outward from the plasmasphere near 2200 UT at 300 kHz, across the plasmopause at about 2125 UT and out into the outer magnetosphere. Outside the plasmopause the band at  $f_{\text{UHR}}$  lies near the lower frequency cutoff of the nonthermal continuum radiation which appears as a region of weak, diffuse wave turbulence above about 10 to 30 kHz. Below the band at  $f_{\text{UHR}}$  are weak, banded emissions corresponding to the diffuse electrostatic bands. These bands lie between harmonics of  $f_g^-$  and have amplitudes typically in the  $\mu\text{V m}^{-1}$  range. The intense yellow band between 2015 and 2115 UT is chorus at about  $f_g^-/2$ .

Since the initial report by Shaw and Gurnett [1975] which alluded to the existence of intense electrostatic waves near  $f_{\text{UHR}}$ , there have been other reports of such waves in the literature. Gurnett [1975] shows a very intense electrostatic wave event in his Figure 13 which appears to be associated with nonthermal continuum radiation. Using the passive plasma wave receiver on board GEOS 1 Christiansen et al. [1978] detected a similar intense

band near  $f_p^-$  at about  $6.5 R_E$  and suggested it might be an example of coherent electron cyclotron harmonic emission. Most recently Gurnett et al. [1979] have shown the very intense band illustrated in Plate 1. Until now, no concerted effort has been made to study the occurrence and origin of these waves in a systematic manner. It is the purpose of this thesis to explore the intense electrostatic waves beyond the plasmopause near  $f_{UHR}$  in detail. We shall describe the spectral characteristics, polarization, and the region of occurrence of the waves as well as the association of these electrostatic waves with other wave modes in the magnetosphere such as odd, half-harmonics of the electron gyrofrequency and nonthermal continuum radiation.

The plasma wave receivers on board the IMP 6 and Hawkeye 1 satellites are well suited to study electrostatic waves in the magnetosphere. The satellites were placed in highly eccentric orbits with greatly different initial inclinations of  $89.8^\circ$  and  $28.7^\circ$  (for Hawkeye 1 and IMP 6, respectively), hence, large portions of the magnetosphere have been sampled. (See Figure 1 of Gurnett and Frank [1977] for an illustration of the portions of the magnetosphere sampled by Hawkeye 1 and IMP 6.) Each plasma wave receiver was designed to sample the broad frequency range occupied by characteristic frequencies of magnetospheric plasma. The plasma wave sensors and receivers on board IMP 6 are described by Gurnett and Shaw [1973] and the Hawkeye 1 plasma wave receiver is described



by Kurth et al. [1975]. Recently, measurements have become available from the ISEE 1 and 2 plasma wave receivers which can greatly enhance our understanding of the waves investigated in this paper. Plate 1 is an example of the measurements possible with the ISEE 1 sweep-frequency-receiver which have been included to complement the survey results obtained with the Hawkeye and IMP 6 instruments. The ISEE 1 and 2 plasma wave receivers are described in detail in Gurnett et al. [1978].

The interaction of the intense waves with magnetospheric plasma is important to the understanding of the wave generation mechanism. In support of this study of intense electrostatic waves we shall present the results of a survey of the plasma environment of the intense wave turbulence. Early observations of the plasma in the region just outside the plasmopause are given by Schield and Frank [1970] and DeForest and McIlwain [1971]. These papers describe the earthward edge of the plasma sheet and the injection of hot plasma sheet electrons into the electron trough during magnetic substorms. Anderson [1976] has demonstrated a correlation between intense electrostatic waves above  $f_g^-$  and the injection of 1.2 keV electrons into the region just outside the nightside plasmopause. The present study is not meant to be a comprehensive study of the plasma just beyond the plasmopause, but rather is concerned with the comparison of these plasmas with observations of intense electrostatic waves near  $f_{UHR}$ .

Measurements of the intensities of electrons and positive ions over an energy range from about 50 eV to 40 keV have been gained with LEPEDea plasma instrumentation on board the Hawkeye 1 spacecraft. The nearly rectangular field of view of the plasma analyzer is directed normal to the spacecraft spin axis, with angular dimension  $30^\circ$  parallel to the spin axis and  $8^\circ$  in the plane of rotation. A thin-windowed Geiger-Mueller tube is provided as part of the plasma instrument to determine the directional intensities of electrons and protons at energies  $E \geq 45$  keV and  $\geq 600$  keV, respectively. Instruments similar to the Hawkeye LEPEDea have been flown on the IMP and Injun satellites and are described in detail in Frank [1967].

While the survey of plasmas associated with the intense electrostatic waves has been carried out with the Hawkeye LEPEDea, measurements recently gained with the ISEE 1 and 2 Quadrispherical LEPEDeas are used to augment the Hawkeye findings. The ISEE instruments provide new opportunities to examine virtually the entire three-dimensional velocity distribution function associated with the waves studied here. The Quadrispherical LEPEDeas are described in Frank et al. [1978].

## II. DESCRIPTION OF INTENSE ELECTROSTATIC WAVES BEYOND THE PLASMAPAUSE

### A. Spectral Properties

An example of the intense electrostatic wave events detected by IMP 6 and Hawkeye is shown in Figure 1 to illustrate the main characteristics of the waves. This illustration shows the average and peak electric field strengths sampled in the eight highest frequency spectrum analyzer channels of the IMP 6 plasma wave experiment for a four-hour interval on January 18, 1972. The solid black area for each channel has a vertical extent proportional to the logarithm of the electric field strength averaged over 5.11-sec. intervals. The dots represent the peak electric field strengths detected during each averaging interval. The event present in the 56.2-kHz channel at about 1950 UT and with a peak electric field strength of  $4.0 \text{ mV m}^{-1}$  is typical of the electrostatic wave events discussed in this report. The location of the plasmopause shown in Figure 1 is identified by observing several characteristic changes occurring nearly simultaneously in the plasma wave spectrum and spacecraft-related interference. As the spacecraft exits the plasmasphere a rather abrupt decrease in amplitude of plasmaspheric hiss can be seen in the signal present in the 3.11-kHz channel of Figure 1.

At the same time, an abrupt increase in interference associated with the solar cell arrays on the spacecraft can be detected in the lower frequency channels (not shown). The upper hybrid resonance band is also a convenient aid in determining the location of the plasmopause since an abrupt drop in frequency of this band is indicative of the decrease in plasma density at the plasmopause. (For a discussion of methods useful in determining plasmopause locations by means of various signatures in plasma wave data see Shaw and Gurnett [1975].) The dashed line labeled  $f_{\text{UHR}}$  in Figure 1 provides an estimate of the upper hybrid resonance frequency and serves only to illustrate the anticipated drop of  $f_{\text{UHR}}$  due to the abrupt decrease in density at the plasmopause. In this case, it is apparent that the intense wave event lies very close to the plasmopause.

A consistent feature of the electric field spectrum of the waves studied here is their narrow bandwidth. The spectrum for the event shown in Figure 1 is illustrated in Figure 2. Notice that the intense wave spectrum is very sharply peaked at 56.2 kHz, with responses in the adjoining channels due principally to filter overlaps in the spectrum analyzer. The bandwidth of the waves is typically less than about 10 percent of the center frequency. The event illustrated in Plate 1 also has a very narrow bandwidth. Some examples of the intense waves appear in high resolution spectrograms made from Hawkeye and IMP 6 wideband analog data. None of

the high resolution spectrograms show any evidence for intense wave events near  $f_{\text{UHR}}$  having bandwidths greater than about 10 percent. Occasionally, other narrow spectral features are present at higher frequencies in conjunction with the band near  $f_{\text{UHR}}$ , and these will be discussed in the section on the identification of the wave mode.

The intensity of the electrostatic turbulence varies greatly as a function of time. The dots in Figure 1 show the sporadic nature of the waves. Variations of more than an order of magnitude in electric field strength are commonly detected on time scales of several minutes to a few seconds. The spectrum in Figure 2 illustrates the variation of intensity over short time intervals.

While the average electric field spectral density in this example is about  $7 \times 10^{-11} \text{ V}^2 \text{ m}^{-2} \text{ Hz}^{-1}$ , the peak is about  $3 \times 10^{-9} \text{ V}^2 \text{ m}^{-2} \text{ Hz}^{-1}$ . This represents a variation of a factor of about 7 in electric field strength in 5.11 seconds.

The intense waves near  $f_{\text{UHR}}$  usually include a weak magnetic component. Following the terminology of Shaw and Gurnett [1975], we have consistently referred to the waves as being electrostatic, but as can be seen in Figure 3, a small but measurable magnetic field component is present. The electric-to-magnetic field energy density ratio for this example is about 1600, while the ratio is usually equal to or greater than about 1000 for the other events detected with IMP 6. In some cases, no magnetic component is detectable. Because the electric-to-magnetic field energy density ratio

is very large compared to that for electromagnetic waves in free space, we refer to these waves as electrostatic. It is important to mention that magnetic field data for the frequency range of interest are available only in the IMP 6 data. We have assumed that features visible in the Hawkeye data which are similar to IMP 6 events in their electric field characteristics also have similar magnetic field properties.

### B. Regions of Occurrence

The initial isolation and characterization of the intense electrostatic waves discussed in this thesis were achieved through a semi-automatic search of plasma wave data acquired with the IMP 6 and Hawkeye 1 satellites. Electrostatic bands near  $f_{UHR}$  are narrow-band and fluctuate rapidly in intensity on time scales of seconds or less. A computer algorithm is used to select narrowband ( $\Delta f/f \leq 10$  percent) events by seeking responses in a single channel which are stronger by a factor of at least 3 than the responses in adjacent channels. The algorithm also selects events which exhibit rapid fluctuations in intensity by requiring a peak-to-average electric field strength ratio greater than about 3. Finally, only those events with maximum electric field strengths greater than about  $1 \text{ mV m}^{-1}$  are selected. Waves of lower intensity have been studied in detail elsewhere [Shaw and Gurnett, 1975].

Intense electrostatic waves at low frequencies, e.g., near  $3f_g^-/2$  have been studied extensively [Kennel et al., 1970; Fredricks and Scarf, 1973; Scarf et al., 1973]. In this thesis we seek to extend the study of electrostatic waves in the magnetosphere to intense waves at frequencies usually much greater than  $f_g^-$ , i.e.,  $f_p^-$  or  $f_{UHR}$ . While the electron plasma frequency may drop to as low as 500 Hz in portions of the magnetotail,  $f_p^-$  is usually greater than about 5 kHz for most regions of the magnetosphere. Hence, the search was conducted at IMP 6 analyzer center frequencies of 5.62, 10.0, 16.5, 31.1, 56.2 and 100 kHz. Two analyzer center frequencies of the Hawkeye plasma instrument were located at slightly different values of 13.3 and 17.8 kHz (versus the 10.0- and 16.5-kHz channels of IMP 6).

Once the list of possible events with narrow spectral structure and large, sporadic amplitudes was generated, the process of gaining specific information on individual events proceeded by hand. In addition to the intense electrostatic events of interest the list includes events for which (1) the waves are clearly electromagnetic, (2) the wave frequencies are well below  $f_p^-$ , and (3) the waves do not occur within the magnetosphere of the earth, such as electron plasma oscillations in the solar wind. The list is refined by hand to accomplish two goals. First, we eliminate events which are clearly not electrostatic waves near  $f_p^-$  or  $f_{UHR}$  in the magnetosphere and second, we attempt to classify and characterize

the remaining events. The refining process relies heavily on the use of high resolution, frequency-time spectrograms which display the wideband analog data gained with each of the plasma wave instruments.

Through our search of over five and one-half years of IMP 6 and Hawkeye observations we have collected approximately 145 electrostatic events with intensities  $\geq 1 \text{ mV m}^{-1}$ . The positions of these intense events are identified in Figure 4, with the figure organized to show four 6-hour segments of local time centered at magnetic noon, midnight, dusk, and dawn. Positions determined within each six-hour quadrant have been rotated (not projected) into the designated meridional plane (e.g., all local times from 2100 through 0300 are rotated into the midnight meridian). The points plotted in Figure 4 represent events detected in each of the six frequency channels from 5.62 kHz through 100 kHz.

It is apparent from Figure 4 that intense electrostatic waves near  $f_{\text{UHR}}$  occur at all local times and over a wide range of latitudes. An examination of the local time distribution of the events on a finer scale than that of Figure 4 does not reveal a significant preference for any local time. The limits of latitudinal coverage by the two satellites are indicated by dashed lines, with coverage within the limits not uniformly distributed. The apparent cutoffs in the occurrence of events near magnetic latitudes  $\pm 50^\circ$  may represent observational limits and not upper bounds for the



phenomena. Orbital coverage is also greatly reduced near the magnetic equator due to the relatively large inclinations of the orbits. Because of this sampling bias greater numbers of intense events may lie close to the equator than are indicated by Figure 4. Kennel et al. [1970] and Fredricks and Scarf [1973] have reported increased occurrence frequencies for intense  $3f_g^-/2$  and  $(n + 1/2)f_g^-$  bands near the equator.

With a sample of only 145 events it is difficult to perform detailed statistical studies. We believe it is significant, however, that from the more than five and one-half years of observations comprising on the order of 1500 plasmopause crossings, the intense waves were observed during only about 10% of the crossings. This implies either that the intense waves are not present most of the time, or that they are confined to localized regions near the plasmopause surface which cover only about 10% of the area normally traversed by Hawkeye and IMP 6. The frequency of occurrence of events at latitudes within  $\pm 10^\circ$  of the magnetic equator is significantly higher than 10%. On the order of one of every three passes of Hawkeye or IMP 6 through the region within  $10^\circ$  of the magnetic equator for  $3 \leq R \leq 8 R_E$  reveal intense waves near  $f_{UHR}$ .

On a few occasions intense electrostatic wave events have been detected in nearly the same region of the magnetosphere and at the same frequency on two consecutive orbits. Some of these event-pairs display striking quantitative similarities suggesting those are not just random, unrelated occurrences. The observation

of similar events on consecutive orbits may imply that the lifetime of those intense wave events can be as long as two to four days (the orbital periods of Hawkeye 1 and IMP 6, respectively).

Evidently, the conditions necessary for the generation of the intense waves are present for periods of time of several hours to a few days and this lifetime could possibly give clues as to the origin of the waves. A reasonable explanation of event lifetimes on the order of a few days is that the intense electrostatic events are related to magnetic storms. A relationship with storms might also explain the infrequent occurrence of the events. However, a study of hourly  $D_{st}$  values at times when the intense wave activity was detected yielded a poor correlation between the wave events and magnetic storms. Only about half of the events showed any association with storms. The values of  $K_p$  during the intense wave events were also analyzed. The distribution of  $K_p$  during the events is not significantly different from the  $K_p$  distribution for all times, hence, no strong association with magnetic activity appears to exist. The events also show little or no correlation with AE as might be expected if electrons injected from the plasma sheet were directly responsible for the instability. In particular, events detected in the midnight sector (21 to 3 hours magnetic local time) show no significant correlation with large values of AE.

A strong correlation between wave frequencies and the radial distance of intense wave events is observed. This trend is illustrated in Figure 5 by plotting the number of events detected in

each frequency channel as a function of radial distance from the earth. The progressive decrease in wave frequencies of the events with increasing radial distances is unmistakable. We have observed approximately 15 events for which the band of emission was present for an interval of time sufficient for the frequency to drift from one channel to the next. In all of these events, the drift was to lower frequencies as a function of increasing radial distance. Notice that the frequency of the intense band in Plate 1 also decreases with increasing radial distance. This relationship is almost certainly due to a close physical connection between the frequencies of these intense bands of electrostatic waves and characteristic frequencies of the local plasma. In this region of the magnetosphere, both the electron plasma frequency and the electron gyrofrequency show monotone decreases with increasing radial distance. It follows that the upper hybrid resonance frequency decreases at the same time (or over the same region of space). In general, the intense electrostatic wave events are observed at frequencies above and often several times greater than  $f_g^-$ . Therefore, we feel confident that the instability is most closely related to either  $f_p^-$  or  $f_{UHR}$ . In the example shown in Plate 1, the ratio  $f_p^-/f_g^-$  is sufficiently large that the difference between  $f_p^-$  and  $f_{UHR}$  is not resolvable. Evidence is presented in the next section which indicates the intense electrostatic turbulence is directly related to  $f_{UHR}$ . The electron gyrofrequency may remain an important parameter through the  $(n + 1/2)f_g^-$  bands. This idea shall be developed further in the next section.

Other parameters which characterize the intense electrostatic waves detected near  $f_{\text{UHR}}$  include the duration (or spatial extent) and the distance from the plasmopause. These parameters are observed to vary greatly in magnitude from event to event with the events illustrated in Figures 1 and 3 and Plate 1 demonstrating some of these variations. For example, notice in Figure 3 that the intense waves clearly lie outside the plasmopause, with the center of the event located nearly  $0.5 R_E$  beyond the plasmopause. In contrast, the event shown in Figure 1 lies just at the plasmopause. Typically, the events range from being just at the plasmopause to a few  $R_E$  outside. The average distance is about  $1.3 R_E$  from the plasmopause. Since a majority of events are not located at the plasmopause, but at significant distances beyond, we conclude that the instability is not directly related to the plasmopause, itself. It is unlikely, then, that strong density gradients are an important factor in the instability. The typical event lasts about 5 to 15 minutes which translates into an average radial extent of about  $0.35 R_E$ . There is wide variability in the radial extent of the events, ranging from less than  $0.1 R_E$  to more than  $1 R_E$ .

### C. Identification of the Wave Mode

By analyzing the polarization of the intense waves and studying other wave modes present in the vicinity of the intense events we can gain information necessary to identify the wave mode of the intense waves. For example, consider the plasma wave observations

gained with Hawkeye 1 on January 31, 1976, during an outbound traversal of the magnetosphere near 10 hours magnetic local time. A portion of the observations are presented in Figure 6 and again in Figure 7 to demonstrate the presence of intense waves with peak electric field strengths  $> 10 \text{ mV m}^{-1}$  in the 31.1-kHz channel between 1840 and 1853 UT. Figure 6 is divided into three regions according to wave polarization. The polarization is determined by analyzing the electric field amplitude as a function of the angle between the electric dipole antenna and the geomagnetic field,  $\vec{B}_0$ . A general description of the method of measuring the polarization using a rotating dipole antenna is discussed in Appendix A. The shaded regions indicate where the polarization of the waves present is such that the electric field of the wave is nearly parallel to  $\vec{B}_0$ . Regions of the figure lacking shading or hatching indicate where the polarization of waves present is such that the electric field is nearly perpendicular to  $\vec{B}_0$ . The hatching indicates that region below  $f_g^-$  consisting of whistler-mode waves which are not of primary interest here. Superimposed on the presentation of Figure 7 is a solid line to specify the electron gyrofrequency and dashed lines for the first four  $(n + 1/2)f_g^-$  harmonics. The magnetic field intensities required to calculate  $f_g^-$  were obtained by means of the onboard magnetometer, and were provided by J. A. Van Allen [personal communication, 1978]. Since the spacing of the eight frequency channels is approximately logarithmic, the ordinate of this figure may be defined as a frequency scale with the baseline of each

channel marking the position of the center frequency of that channel.

As shown in Figure 6 the polarization of the intense electrostatic turbulence at 31.1 kHz is such that the wave electric field is virtually perpendicular to the geomagnetic field,  $\vec{B}_0$ . Figure 8 shows the variation of the electric field as a function of antenna orientation angle,  $\delta$ . During the intense event, the spin axis,  $\vec{\omega}$ , of the spacecraft is nearly perpendicular to  $\vec{B}_0$  and provides an excellent opportunity to measure the angle between  $\vec{B}_0$  and the wave electric field,  $\theta$ . The analysis, detailed in Appendix A, indicates  $\theta \geq 80^\circ$ . The perpendicular polarization of these waves provides the best evidence that the waves are most closely related to  $f_{UHR}$  and not  $f_p^-$ . There are no modes at  $f_p^-$  which have perpendicular polarizations, whereas the modes at  $f_{UHR}$  are all polarized perpendicular to  $\vec{B}_0$  [Shaw and Gurnett, 1978]. Other events have been analyzed for polarization with each one showing a perpendicular rather than parallel polarization.

A characteristic feature of the intense electrostatic waves is that the intensification generally occurs at  $f_{UHR}$  when  $f_{UHR} \approx (n + 1/2)f_g^-$ . This is clearly seen in Plate 1. Notice that there are weak banded emissions below the intense band at  $f_{UHR}$ . These bands lie at about  $3/2$ ,  $5/2$ ,  $7/2$ , and  $9f_g^-/2$ . (Near 1930 UT the  $11f_g^-/2$  band can also be seen.) The intensification at 2110 appears to occur when the  $9f_g^-/2$  band coincides with the band at  $f_{UHR}$ . The magnitude of the intensification is orders of magnitude greater

than a simple addition of wave amplitudes of the diffuse electrostatic bands and the usually weak UHR band.

Although the effect is more difficult to see in the Hawkeye data, the event in Figures 6 and 7 also shows that the intense waves occur when  $f_{\text{UHR}} \approx (n + 1/2)f_g^-$ . Figure 7 shows that the intense electrostatic waves in the 31.1-kHz channel lie directly at the  $7f_g^-/2$  harmonic. Diffuse electrostatic waves in the 23.7- and 17.8-kHz channels also align well with the  $7f_g^-/2$  band, but these are very weak. From Figure 7 one can visualize a continuous band at  $7f_g^-/2$  which suddenly intensifies near 1845 UT. Most of the events studied may be interpreted as intensifications of one of the  $(n + 1/2)f_g^-$  bands.

There is sufficient information available in Figures 6 and 7 to identify the frequency of the intensification of the  $7f_g^-/2$  band as  $f_{\text{UHR}}$ . The waves in the shaded region of Figure 6, consisting of low amplitude waves with  $\vec{E} \parallel \vec{B}_0$ , are almost certainly continuum radiation propagating mainly in the (L, 0) mode (in the convention of Stix [1962]). The intense wave event is located very close to the lower frequency cutoff of the continuum radiation which must be  $f_p^-$ . Since the intense waves are at about  $3.5f_g^-$ ,  $f_p^- \approx f_{\text{UHR}}$ , and as discussed above, the perpendicular polarization of the intense wave turbulence unambiguously identifies  $f_{\text{UHR}}$  as the characteristic frequency important in the instability. Therefore, the event shown in Figures 6 and 7 is an intensification of the  $7f_g^-/2$  band at  $f_{\text{UHR}}$ .

There exist many other examples of intense wave events occurring at  $f_{\text{UHR}}$  when  $f_{\text{UHR}} \approx (n + 1/2)f_g^-$ . Figure 7 displays IMP 6 wideband data in a mode which cycles through bandwidths of 0.65 to 10 kHz, 11 to 19 and finally 21 to 29 kHz (not shown) while alternately switching between a magnetic loop antenna and an electric dipole antenna. During this time interval the electron gyrofrequency is about 1.9 kHz (based on IMP 6 measurements of the magnetic field obtained from the National Space Science Data Center, N. F. Ness and D. H. Fairfield, principal investigators) and electrostatic bands near  $3f_g^-/2$  and  $5f_g^-/2$  are clearly seen. Continuum radiation is detected in the magnetic spectrogram with a lower cutoff at 15 kHz. (Due to the AGC characteristics of the receiver, the gain of the receiver is set much higher in the magnetic portion of the cycle allowing the detection of the weak continuum radiation. The presence of the intense band at about 15.2 kHz in the electric portion of the cycle sets the gain to a low value, hence, the continuum radiation can no longer be detected.) The intense electrostatic band at about 15.2 kHz is at a frequency very close to  $15f_g^-/2$ . Notice that the emissions near 15 kHz are separated by a frequency very close to  $f_g^-$ . Also, if the lower frequency of the continuum radiation is  $f_p^-$ , then  $f_{\text{UHR}}$  is very nearly 15.2 kHz. The significance of  $f_{\text{UHR}} \approx (n + 1/2)f_g^-$  for the intense wave events will be addressed in Chapter IV.



The question which remains concerning the event in Figures 6 and 7 is the explanation of the apparent spread in frequency of the intense event. It appears that the emissions occupy a very broad band of frequencies extending at least from 13.3 kHz to 178 kHz. The responses of all but the two channels adjacent to the 31.1-kHz channel are too great to be attributed to a single, narrowband signal at 31.1 kHz. There are three possible explanations for the responses in the other channels: (1) the event is broadband, (2) there is distortion due to receiver saturation, or (3) the event consists of multiple bands. From our survey of the high resolution spectrograms we can eliminate the possibility of the event being broadband since no evidence for broadband events has been seen. Without high resolution spectrograms for this specific example, however, the other two possibilities must remain. Specific examples of multiple-banded events which are most likely due to harmonic distortion can be found in the wideband, analog data.

We should point out that evidence of multiple-banded events has been found in at least one example from observations with the Hawkeye instrument and is displayed in Figure 10. The waves of interest are the two bands near 27 kHz and 49 kHz. To assure that these bands are similar to other intense waves in the study, we have analyzed the polarization. The arrows in Figure 10 indicate those times when the electric antenna is oriented perpendicular to the geomagnetic field. Since the times indicated by the arrows correspond reasonably well to peaks in the intensities of the bands

at 27 and 49 kHz we can deduce that these bands, like the one in Figure 6, are nearly perpendicularly polarized. The fact that the band at 49 kHz is detected at all attests to its significant intensity since the wideband receiver's sensitivity at 49 kHz is down by about 7 db in comparison to the sensitivity at lower frequencies. In addition, the gain of the AGC receiver is greatly reduced due to the intense band at 27 kHz. Since the dynamic range of the display (i.e., the film) is only about 20 db, the band at 49 kHz is within an order of magnitude of being the same amplitude as the band at 27 kHz. We can rule out receiver distortion as an explanation for the multiple bands in this event because they are not harmonically spaced. (The effect of receiver saturation and distortion is to generate false harmonics of the real signals.) Also, it is doubtful that both of the bands in Figure 10 are  $(n + 1/2)f_g^-$  harmonics. The measured magnetic field yields an electron gyrofrequency of about 16 kHz as indicated to the right of Figure 10. The lower band at 27 kHz certainly lies between  $f_g^-$  and  $2f_g^-$ , but the second band lies too close to the third harmonic of  $f_g^-$  to be considered an odd half-harmonic. An alternate hypothesis is that the band at 27 kHz is not only a so-called 3/2 band, but also lies at  $f_{UHR}$ . Knowing  $f_{UHR}$  and  $f_g^-$  allows a calculation of  $f_p^-$ . Hence, according to this hypothesis  $f_p^-$  is about 22 kHz. It is interesting to note that the band at 49 kHz is approximately 22 kHz above the band at 27 kHz. Further, close scrutiny of Figure 10

yields some evidence of wave activity near 22 kHz. Hence, it is possible that a mixture of waves at  $f_p^-$  and  $f_{UHR}$  produces the band at 49 kHz, although this is a highly speculative supposition.

### III. PLASMA SIGNATURES ASSOCIATED WITH INTENSE ELECTROSTATIC WAVES

#### A. Survey of Plasma Measurements Gained During Intense Electrostatic Wave Events

As a first step in accumulating information about plasmas associated with intense electrostatic waves near  $f_{UHR}$  we shall survey plasma measurements taken simultaneously with the detection of the waves. For 47 events detected with the Hawkeye plasma wave instrument energy-time spectrograms have been produced from data from the LEPDEEA. The energy-time spectrograms allow large quantities of information concerning intensities, pitch angle distributions, energies, etc., to be studied in a simple, compact form. The spectrograms were analyzed to detect plasma signatures which might be uniquely related to the intense waves of interest. Before proceeding, however, we must caution that while the energy carried by the waves is large, the ratio of the wave energy density to the thermal energy of the plasma is very small, typically less than  $10^{-4}$ . Hence, the free energy source in the plasma distribution function need not be large. It is also crucial to realize that the measured distribution function is a time-stationary state which is in pseudo-equilibrium with the intense waves. That is,

the measured distribution function may not only be that function driving the waves, but, also, is almost certainly being modified by the waves through diffusion.

The plasma survey is limited to electrons with energies greater than several hundred eV. Because the waves are at high frequencies, the importance of ions in the wave-particle interaction must be negligible. Also, measurements of electron intensities below energies of several hundred eV with the Hawkeye LEPEDA at  $4 \leq L \leq 8$  may be aliased by spacecraft charging [Gurnett and Frank, 1976]. While this eliminates the study of cold electrons, it may be that hot electrons will prove to be instrumental in the wave-particle interaction as indicated by the correlation of 1.2 keV electron fluxes with electrostatic waves above  $f_g^-$  [Anderson, 1976]. Also, Lyons [1974] demonstrated that the energy of electrons diffused by electrostatic waves above  $f_g^-$  increased as the energy in the waves increases, hence, the wave studied here could put 1 to 10 keV electrons on strong diffusion.

Measurable intensities of electrons at energies  $E \geq 900$  eV are detected with all but one of the intense electrostatic wave events for which simultaneous observations are available and many of these show moderate to large intensities,  $\sim 10^3$  to  $10^4$  ( $\text{cm}^2 - \text{sec} - \text{sr} - \text{eV})^{-1}$ , typically. Generally, the intense wave regions are much more tightly confined (temporally or spatially) than the regions of a few-keV electrons thought to be associated with the waves.

There are striking examples showing excellent correlation between the occurrence of an intense wave event and a peak in intensity of  $\sim 1$  to 20 keV electrons. An example of such a case is shown with the aid of Plate 2 and Figure 11. The center panel of Plate 2 shows the intensity of electrons as a function of energy and time. The scale at the left of the panel gives the common logarithm of the energy and ranges from about 50 eV to 40 keV. The color bar at the right is calibrated in units of the logarithm of the instrument responses, counts  $(\text{sec})^{-1}$ . The sinusoidal pattern of dots just above the center panel indicates the pitch angle,  $\alpha$ , being sampled as a function of time. The coverage of pitch angles or the envelope of the sine wave is a function of time and depends on the orientation of the spacecraft's spin axis with respect to the geomagnetic field. In this case the pitch angle sampling is fairly poor:  $45^\circ \leq \alpha \leq 135^\circ$ .

The wave event in Figure 11 is most intense in the 17.8-kHz channel (nearly  $10 \text{ mV m}^{-1}$ ) between about 2258 and 2305 UT and lower amplitude wave turbulence occurs somewhat earlier in the 13.3-kHz channel. The event is centered at about  $54^\circ$  magnetic latitude. The plasma spectrogram in Plate 2 shows a gradual rise in electron intensities near 1 keV beginning at about 2250 UT and they become quite intense near 2258 UT. There is a fairly sharp decrease in intensity at about 2305 UT. The narrow intensity peaks at large amplitudes are analyzer responses to scattered solar Lyman- $\alpha$  radiation.

This example, then, shows reasonably good temporal correlation between the intense waves and intensities of  $\sim 1$  to 10 keV electrons. About 26% of the cases studied exhibit this good spatial (temporal) correlation.

The example shown in Plate 2 and Figure 11 of good spatial correlation between intense electrostatic waves and electron intensities is an exceptional case in that 74% of the events do not show as good a correlation between the onset and cessation times of the wave and particle events. A more typical event consists of a fairly localized region of intense waves which occurs within an extended region of plasma-sheet-like plasma. The spectrograms do not generally reveal noticeable changes in the signature of the electron intensities during the intense wave event. Of the events at magnetic latitudes greater than  $20^\circ$  virtually all of those events showing poor correlations between intense wave events and obvious plasma signatures lie at magnetic local times between about 4 hours and 20 hours. Events showing good correlations at latitudes above  $20^\circ$  lie between about 20 hours and 4 hours magnetic local time. Notice that the event with a good temporal correlation in Figure 11 and Plate 2 is an apparent exception to this local time trend. Local time does not appear to affect the wave-plasma correlation for events near the magnetic equator. The evidence is fairly convincing that the intensity of  $\sim 1$  to 20 keV electrons cannot be the only parameter important in the instability resulting in intense electrostatic waves

near  $f_{UHR}$ . That is, the instability responsible for the intense waves is most likely related to a feature of the electron distribution function and not simply electron intensity.

For approximately 30% of the events studied the orientation of the spacecraft spin axis is such that a fairly complete range of pitch angles is sampled by the Hawkeye LEPDEA. All of these cases which include a wide range of pitch angle sampling show evidence of electron anisotropy. Each of the fourteen events exhibiting anisotropy has maximum electron intensities near  $\alpha = 90^\circ$  with minima at  $0^\circ$  and  $180^\circ$ . An example of anisotropic electron distributions associated with intense electrostatic waves is shown in Plate 3. Plate 3 displays the LEPDEA energy-time spectrogram coinciding with an intense wave event during orbit 205 which is illustrated in Figure 12.

The intense waves in the orbit 205 event peak in the 100-kHz channel of the plasma wave receiver at about 2207 UT on August 15, 1975. Notice that between 2200 and 2210 UT in the electron spectrogram of Plate 3 there is a periodic signature near 1 keV which extends in energy as high as about 20 keV. Using the sinusoidal pattern above the panel, we can explain the periodicity in the signature as a pitch angle anisotropy. Notice that when the electron intensity near 1 keV is a maximum, the instrument is sampling near  $\alpha = 90^\circ$ . This event is located almost directly on the magnetic equator. The orientation required to allow sampling of the widest range of pitch angles occurs only very close to the magnetic equator.



Hence, we have evidence for anisotropic distributions of electrons only for events close to the equator.

In summary of the plasma survey we have shown that while  $\sim 1$  to 20 keV electrons apparently are a factor in the instability responsible for the intense electrostatic waves near  $f_{UHR}$ , the intensity of electrons is not, in itself, the controlling factor. At least for the events near the magnetic equator, it appears that an anisotropy in the electron distribution could be a more important feature. It is necessary, however, to look more closely at the distribution function to analyze the details of the electrons which are responsible for the instability.

#### B. Electron Distribution Functions Measured During Intense Electrostatic Wave Events

In this section we analyze in detail a portion of the electron distribution function for several events which were included in the general survey described above. In order to obtain as complete distribution functions as possible, we are constrained to events lying close to the magnetic equator where the maximum range of pitch angles is sampled and having adequate analyzer response at pitch angles as small as  $30^\circ$ .

We shall now examine two events which demonstrate possible sources of free energy in the electron distribution function in the form of a temperature anisotropy and a loss-cone distribution. In Figure 13 we show the electron velocity distribution

function,  $f(v_{\perp}, v_{\parallel})$  measured during an intense wave event at 0430 UT on April 5, 1977, which is shown in Figure 14. The distribution function covers the energy range of about 1 to 38 keV. Plotted are contours of constant  $f(v_{\perp}, v_{\parallel})$ . The dashed line is the 100 counts (sec) $^{-1}$  line and indicates that measurements at smaller  $v_{\perp}$  (or smaller  $\alpha$ ) may be suspect due to poor statistics. Two features of the distribution function shown in Figure 13 may be of importance with respect to the wave event detected simultaneously. First, there is evidently a temperature anisotropy with the perpendicular-to-parallel temperature ratio,  $T_{\perp}/T_{\parallel}$ , approximately 2 in the energy range shown. Second, a loss cone is evident at small pitch angles ( $\alpha \leq 20^{\circ}$ ). The loss cone appears as an indentation near the  $v_{\parallel}$  axis and an evaluation of  $\partial f(v_{\perp}, v_{\parallel})/\partial v_{\perp}$  for  $v_{\parallel} \geq 3 \times 10^9$  cm (sec) $^{-1}$  would result in a positive slope.

Both of these features may be unstable to electrostatic waves. A temperature anisotropy has been shown to be unstable to waves between  $nf_g^{-}$  and  $(n+1)f_g^{-}$  if the thermal anisotropy ( $A = (T_{\perp}/T_{\parallel}) - 1$ ) exceeds  $n$  [Ashour-Abdalla and Cowley, 1974]. In the cases examined, however, the anisotropy does not appear to be large enough to drive instabilities in the higher harmonics unless the anisotropy condition of Ashour-Abdalla and Cowley might be relaxed by the addition of cold electrons [Ashour-Abdalla, personal communication, 1978]. The loss-cone distribution function has been used by Ashour-Abdalla and Kennel [1978b] as a free energy source to study multi-harmonic cyclotron waves.

A second example, similar to the orbit 487 example discussed above is illustrated in Figure 15. The distribution function shown here is measured in conjunction with the intense wave event shown in Figure 16 at about 2155 UT on June 12, 1975. Again,  $T_{\perp}/T_{\parallel}$  is approximately 2 and there is a suggestion of a loss cone at small pitch angles. The distribution function measured was actually taken after the peak in the wave event. Larger counting rates are present at about 2200 and after. Measurement simultaneity has been sacrificed for improved counting statistics in this case. Hence, it is possible a more pronounced loss cone could be observed earlier during the peak of the wave event.

The loss-cone distributions presented in Figures 13 and especially 15 are quite weak and it would be prudent to question the validity of the effect. Because the LEPDEA field of view is finite, measurements at very small pitch angles also include a response to particles with larger pitch angles. The effect is to fill in or de-emphasize any loss cone which is in the actual distribution function. Figure 17 demonstrates the magnitude of the de-emphasis. The solid contours of  $f(v_{\perp}, v_{\parallel})$  in Figure 17 are a model hot distribution function based on the subtracted bi-Maxwellian given by Ashour-Abdalla and Kennel [1978a]. The dashed contours in the figure represent the response of a finite-width detector, such as the Hawkeye LEPDEA, to the model distribution function. The point of this exercise is to demonstrate that weak loss-cone distributions as measured by the Hawkeye LEPDEA in orbits 487 and

176 are conservative measurements of the depth of the real loss cone. The model contours in Figure 17 also serve as a comparison between theory and observation. The model is representative of the models used in the multi-cyclotron harmonic emission theory while Figures 13 and 15 represent the first measurements of distribution functions in the magnetosphere which may be related to these waves. Notice that there are certainly good qualitative similarities between the model and actual observations, especially pertaining to the form of the loss cone.

Two additional examples are shown which are similar to the above two examples, but suggest there are variations in the character of the distribution of electrons during the intense wave events and possibly a third form of free energy. Figure 18 is the electron distribution function for the intense wave event in the 100-kHz channel at 2345 UT on November 17, 1975, shown in Figure 19. The distribution of Figure 18 again shows a loss cone at small pitch angles and a definite anisotropy. In this event, however, the increased density of hot electrons with large pitch angles is confined to pitch angles quite close to  $90^\circ$ .

A similar distribution is shown in Figure 20, corresponding to the wave event of orbit 205 shown above in Figure 12. The second dashed line in Figure 20 at smaller  $v_\perp$  is the 50 count (sec)<sup>-1</sup> contour and indicates that electron intensities measured nearly parallel to  $B_0$  are very small and should be disregarded. Hence, little can be said about the possibility of a loss cone in this

example. The feature of interest in this example, however, is near  $\alpha = 90^\circ$  and  $6 \times 10^9 \leq v_\perp \leq 10^{10} \text{ cm (sec)}^{-1}$ . Again, the distribution shows greater intensities very near  $\alpha = 90^\circ$  but it is intriguing to speculate on the possibilities presented by the  $f(v_\perp, v_\parallel) = 10^{-32}$  contour. The energy resolution of the Hawkeye LEPEDEA is quite coarse due to weight and power limitations. While there is no direct evidence, it is possible that there may be a local maximum at  $v_\parallel = 0$  and  $v_\perp \approx 8 \times 10^9 \text{ cm (sec)}^{-1}$ . Hence, a third possibility for a free energy source is suggested by the orbit 205 event which is a bump-on-tail in the perpendicular distribution function.

While this study of the plasma associated with intense electrostatic waves near  $f_{\text{UHR}}$  just outside the plasmopause does not treat the cold electrons, a definite tie between electrons with energies in the range  $\sim 1 - 20 \text{ keV}$  and the waves can be seen. The relevant plasma signature is most likely a detail of the distribution function. Because of the intensity of the waves, it is obvious that an important signature which might be isolated would be the source of free energy in the plasma interacting with the waves. This study exposes three possibilities for such a free energy source: (1) a loss-cone distribution, (2) a temperature anisotropy, and (3) a bump-on-tail in the perpendicular velocity distribution at  $v_\parallel = 0$ , although there is no solid evidence for

this third possibility in the data shown. The temperature anisotropies measured are not great and may not be sufficient to drive the instability to higher  $(n + 1/2)f_g^-$  harmonics.

#### IV. A COMPARISON OF INTENSE ELECTROSTATIC WAVES OBSERVED NEAR $f_{\text{UHR}}$ WITH LINEAR INSTABILITY THEORY

##### A. Review of the Theory of Electrostatic Waves Above the Electron Gyrofrequency

The observations presented heretofore strongly suggest that the theory of electrostatic, multi-cyclotron instabilities may provide a straightforward explanation of the intense wave mode explored in this study. We begin here by reviewing briefly the development of the linear theory of the  $(n + 1/2)f_{\text{g}}^-$  instabilities. Then we shall draw a scenario relating the theory to the intense, upper hybrid resonance waves and show that there is substantial, qualitative agreement between the theory and observations.

The development of the theory of electrostatic cyclotron instabilities may be described as a series of efforts to solve the Harris [1959] dispersion relation at frequencies above the electron gyrofrequency. The dispersion relation is satisfied for longitudinal plasma waves in a uniform magnetic field:

$$D\left(\omega^*, k, \frac{k_{\perp}}{k_{\parallel}}\right) = 1 + \frac{\omega_p^2}{k^2} \sum_{n=-\infty}^{\infty} \int \frac{G_n(v_{\parallel}) dv_{\parallel}}{\omega^* - k_{\parallel} v_{\parallel} - n\Omega} = 0 \quad (1)$$

where

$$G_n(v_{||}) = 2\pi \int_0^{\infty} \left( \frac{n\Omega}{v_{\perp}} \frac{\partial F}{\partial v_{\perp}} + k_{||} \frac{\partial F}{\partial v_{||}} \right) J_n^2 \left( \frac{k_{\perp} v_{\perp}}{\Omega} \right) v_{\perp} dv_{\perp}$$

$\omega^*$  complex frequency;

$\vec{k}$  wave vector;

$k_{||}$  component of  $\vec{k}$  parallel to the static magnetic field;

$k_{\perp}$  component of  $\vec{k}$  perpendicular to the static magnetic field;

$\Omega$  electron gyrofrequency ( $\Omega = 2\pi f_g^-$ );

$\omega_p$  electron plasma frequency ( $\omega_p = 2\pi f_p^-$ );

$v_{\perp}, v_{||}$  perpendicular and parallel electron velocities, respectively;

$J_n$  Bessel function of the first kind;

$F$  normalized electron distribution ( $f(v_{\perp}, v_{||}) = nF(v_{\perp}, v_{||})$ , where  $n$  is the particle number density).

By using a ring distribution of the form

$$F = \frac{1}{2\pi} \delta(v_{\perp} - u) \delta(v_{||}) \quad (2)$$



Fredricks [1971] solved the dispersion relation and showed that instability above  $f_g^-$  was possible for a range of  $k_\perp/k_\parallel$ . But the distribution function is unrealistically severe for plasmas in the magnetosphere, hence Young et al. [1973] improved the situation by demonstrating that the addition of a cold electron component with density  $n_c$  and temperature  $T_c$  to a hot loss-cone distribution could produce instability between  $f_g^-$  and  $2f_g^-$ . The source of the cold electron population is generally assumed to be the ionosphere. A distribution function consisting of a cold population and a hot, loss-cone population with density  $n_h$  and temperature  $T_h$  became the general form used by all subsequent investigators.

The first detailed numerical solutions obtained to investigate the effect of  $n_c$ ,  $n_h$ ,  $T_c$ ,  $T_h$  and the slope of the loss cone were by Karpman et al. [1973, 1975]. Karpman et al. identified the 3/2 instability as the cold upper hybrid mode and found that the upper unstable frequency limit was  $f_{UHC}$  ( $f_{UHC}^2 = (f_g^-)^2 + (f_{pc}^-)^2$  calculated using the cold electron density,  $n_c$ ). They also found that there were many normal modes above  $f_g^-$  and that instability was encouraged by strengthening the positive slope of the loss cone and by using a finite  $T_c$ .

The theory of electrostatic cyclotron instabilities was advanced by the development of an algorithm to give minimum and maximum unstable frequencies based on marginal stability analysis [Ashour-Abdalla et al., 1975]. Ashour-Abdalla et al. employed

the algorithm to analyze bandwidths of the instabilities using a subtracted, bi-Maxwellian distribution with  $T_c = 0$  while varying  $n_c/n_h$  and  $f_{UHC}/f_g^-$ .

It was recognized by Ashour-Abdalla and Kennel [1975] that the convective nature of the electron cyclotron waves was important to the correct identification of the most rapidly growing modes. Hence, they calculated the spatial growth rate,  $K_1$  ( $K_1 = \gamma/v_g$ ) where  $\gamma$  is the temporal growth rate, i.e., the imaginary part of the wave frequency and  $v_g$  is the group velocity. Ashour-Abdalla and Kennel used calculations of  $K_1$  to show that finite cold temperatures ( $T_c \neq 0$ ) are required to explain observations of 3/2 bands in the magnetosphere. With the addition of cold electrons at non-zero temperatures  $v_{g\perp}$  can approach zero, hence the waves become nonconvective. As  $v_g$  approaches zero the spatial growth rate can become very large, even with small temporal growth rates.

When it became clear that the cyclotron instabilities could become nonconvective, the analysis of the wave modes as a function of parameters in the model distribution function as well as the wave frequency and  $k_\perp/k_\parallel$  became significantly more complex. In order to positively identify relevant trends of the instabilities with variations of the plasma model Ashour-Abdalla and Kennel [1978a] employed complete searches in wave-number space. In addition, they assumed that the modes most easily observed experimentally would be those with the largest spatial growth rates.

By performing complete searches in wave-number space and finding regions of nonconvective instability Ashour-Abdalla and Kennel [1978a] conducted a thorough study of the parameters important in the electron cyclotron harmonic instabilities, particularly for  $f_g^- < f < 2f_g^-$ . They found that  $n_c$  controlled which of the harmonic bands could be excited. In general, the highest frequency  $(n + 1/2)f_g^-$  band to be unstable is that band which includes  $f_{UHC}$ . In addition, if the ratio  $n_c/n_h$  becomes sufficiently large, the lower frequency bands will stabilize. Ashour-Abdalla and Kennel also found that as  $T_c/T_h$  grows larger than a few times  $10^{-2}$  the instability becomes convective. The loss-cone fill-in parameter,  $\Delta$ , was also varied with the result that nonconvective instability could still be achieved with a partially filled loss cone ( $\Delta > 0$ ) but the bandwidth of strong growth would be narrower than for the empty loss cone. A significant result was that more than one band could become nonconvectively unstable simultaneously.

The most directly applicable advance in the theory to the study of intense electrostatic waves near  $f_{UHR}$  was the prediction of a nonconvective instability in the  $(n + 1/2)f_g^-$  band containing  $f_{UHC}$  [Ashour-Abdalla and Kennel, 1978b]. For values of  $n_c/n_h$  greater than about 1.5 and less than about 4, a single band at a frequency less than about  $f_{UHC}$  but within the same  $(n + 1/2)f_g^-$  band could become nonconvectively unstable, at least for  $n$  equal 1, 2, or 3.

Hubbard and Birmingham [1978a] classified electrostatic cyclotron harmonic bands observed in the magnetosphere and proceeded to demonstrate that the various classes of waves could be produced by varying parameters of the model distribution function. The model used by Hubbard and Birmingham is nearly the same as that used by Ashour-Abdalla and Kennel [1978a,b] but makes use of a Lorentzian of order  $p$  in the hot, parallel distribution. Specifically, they more or less reproduce the results of Ashour-Abdalla and Kennel [1978a] for the  $3f_g^-/2$  emission, requiring  $n_c/n_h \leq 1$ ,  $T_c/T_h \leq 0.2$  and  $f_{\max} < f_{\text{UHC}} \leq 3$  where  $f_{\max}$  is the maximum wave frequency. Parameters required for multiple  $(n + 1/2)f_g^-$  bands are  $n_c/n_h \leq 1$  and  $f_{\max} \leq f_{\text{UHC}}$ . For diffuse electrostatic bands they predict  $n_c/n_h \gg 1$ ,  $T_c/T_h \sim .01$ , and, again,  $f_{\max} \leq f_{\text{UHC}}$ . The classification studied by Hubbard and Birmingham which is most pertinent to the waves treated in this paper are classified as " $f \sim f_p$  waves". For this classification the results indicate  $n_c/n_h$  may be much larger than unity and  $T_c/T_h$  is less than about 0.02. The " $f \sim f_p$  waves", however, are typified in Hubbard and Birmingham paper by an event near  $10.9 R_E$ . This is clearly outside the region where intense waves near  $f_{\text{UHR}}$  are usually detected. In addition, by polarization measurements we have specifically ruled out any identification of the waves studied here with the electron plasma frequency. We assume that any waves treated by Hubbard and Birmingham using the electron cyclotron instability theory are close to  $f_p^-$  only because  $f_g^- \ll f_p^-$  and, therefore,  $f_p^- \sim f_{\text{UHR}}$ .

B. Comparison of the Theory of Electrostatic  
Multi-Harmonic Emissions With  
Observations of Intense Waves Near  $f_{UHR}$

In this section we shall apply the theory of electrostatic, multi-harmonic emissions to the study of intense waves near  $f_{UHR}$ . A reasonable scenario explaining the upper hybrid waves can be drawn from Ashour-Abdalla and Kennel [1978b] and Hubbard and Birmingham [1978a]. Both of these papers predict stronger wave growth near  $f_{UHC}$  than at other frequencies (assuming in the case of Hubbard and Birmingham that  $f_{UHC} \approx f_p^-$ ). Both papers indicate that a necessary requirement for wave growth primarily near  $f_{UHC}$  is  $n_c/n_h \gtrsim 1$  (and possibly  $n_c/n_h \gg 1$  in the case of Hubbard and Birmingham). If, indeed,  $n_c/n_h \gtrsim 1$  then  $f_{UHC}$  approaches  $f_{UHR}$  and the identification of the observed waves with  $f_{UHR}$  (based on the total number density) is reasonable. Through a search of wave-number space Ashour-Abdalla and Kennel found that the band near  $f_{UHC}$  can be nonconvectively unstable, hence, it is reasonable to expect large wave growth.

Below is a qualitative comparison of the theory of the electrostatic cyclotron instabilities and observations of intense waves which shows good agreement between the theory and observations. Ultimately, however, one would like to do direct, numerical comparisons between growth rates calculated using the measured distribution function and simultaneously measured waves. This direct, numerical comparison, however, can only be accomplished when theory

and observations are at a sufficiently advanced stage. For example, all the theoretical studies until this time have used basically the same cold electron core plus a hot loss-cone distribution as a model. The partial distribution functions shown in Figures 13, 15, 18, and 20 represent the first measurements of the real distribution function associated with the intense upper hybrid waves. Further, the Hawkeye distribution functions yield virtually no information about the cold electrons which are equally important in the instability. Only now are more-complete plasma measurements becoming available with GEOS and ISEE [Borg et al., 1978; Frank et al., 1979]. For example, the ISEE 1 distribution function shown in Figure 22 extends to about 200 eV, however, this may still not yield any conclusive information about the "cold" electrons important in the cyclotron theory. Measurements with a different mode of the ISEE instrument extending the energy range covered to near 1 eV should provide significant answers to questions about the cold component.

Now that the observations are beginning to provide detailed wave and plasma measurements, the theory will have to be revised to utilize analytic or numerical distributions which more accurately reflect the true conditions of the magnetosphere. Even so, quantitative saturation amplitudes will remain incalculable because the waves we study here are sufficiently intense that they cannot be treated thoroughly with the linear theories in existence presently. Currently, there exists a solid quasi-linear theory of diffusion of hot electrons

due to intense electrostatic waves above  $f_g^-$  [Lyons, 1974], but an additional saturation mechanism which must be addressed is the heating of the cold electrons [Ashour-Abdalla *et al.*, 1979]. The qualitative agreement between theory and observation to be shown here, then, will not provide a complete and unambiguous explanation of the intense electrostatic waves near  $f_{UHR}$ , but will demonstrate that a sound basis for the instability can be found in the theory of electrostatic multi-harmonic waves.

Perhaps the clearest indication in the theory that intense wave growth is to be expected near  $f_{UHR}$  comes from a study of the regions of nonconvective instability as a function of the upper hybrid resonance frequency and  $n_c/n_h$ . Figure 21 shows the results of such a study for  $f_g^- < f_{UHC} < 5 f_g^-$ . The abscissa is  $f_{UHC}$  normalized to the gyrofrequency, and  $n_c/n_h$  is scaled on the ordinate. For  $T_c/T_h = 5 \times 10^{-2}$  regions of nonconvective instability are plotted for the  $(n + 1/2)f_g^-$  harmonics with  $n = 1, 2, 3$ , and 4. The plasma model used is the subtracted bi-Maxwellian of Ashour-Abdalla and Kennel [1978a]. Notice that there is a wide range of  $n_c/n_h$  greater than about 1.5 where only the harmonic in the same band as  $X_{UHC}$  is nonconvectively unstable. At the same time, the other bands are convective. For example, if  $f_{UHC}$  is about  $3.5f_g^-$  and  $n_c/n_h$  is about 2, Figure 21 indicates that the third harmonic band will be nonconvectively unstable while the lower two bands will show weaker, convective growth. Little growth is

expected much above  $f_{\text{UHC}}$ , hence, the fourth harmonic would not show strong growth, either, since  $f_{\text{UHC}} \approx 3.5f_g^-$ . Notice that Figure 21 provides a simple determination of wave amplitude in that growth within a nonconvective region is expected to be large and growth elsewhere is expected to be weak or non-existent. As shown by Ashour-Abdalla and Kennel [1978b] the nonconvective regions appear to coincide roughly with contours of constant spatial growth rate with regions of larger growth within the contours. Figure 21 also shows that for  $n_c/n_h$  less than about 1, two or more of the first four harmonics may be nonconvectively unstable simultaneously if  $f \leq f_{\text{UHC}}$ .  $T_c/T_h$  has been chosen fairly large in Figure 21 to limit the regions of nonconvective instability and hence the first band does not appear to become unstable until  $X_{\text{UHC}}$  exceeds 2.5. Refer to Ashour-Abdalla and Kennel [1978a] for a more thorough study of the first harmonic band.

Given that  $n_c/n_h \geq 1.5$ , then, a single, intense band near  $f_{\text{UHC}}$  should be seen in the wave observations with only weak growth at lower frequencies. This effect has been demonstrated in Chapter II. Plate 1 and Figures 6 and 7 show that when  $f_{\text{UHR}}$  lies near an  $(n + 1/2)f_g^-$  band, intense wave growth is observed. Recently obtained measurements from the ISEE 1 plasma wave receiver show this effect much more clearly. For example, Plate 4 is a display of ISEE 1 sweep-frequency-receiver data for an outbound pass through the magnetosphere. The relatively weak, diffuse wave turbulence



above  $\approx 20$  kHz between 1900 and 2230 UT corresponds to trapped, nonthermal continuum radiation which cannot propagate at frequencies below the local  $f_p^-$  [Gurnett and Shaw, 1973; Gurnett, 1975]. The weak banded emissions near 2000 UT below the continuum radiation are diffuse electrostatic bands [Shaw and Gurnett, 1975] which lie between harmonics of  $f_g^-$ . To the accuracy that this display can be read,  $f_{UHR}$  lies close to the lower boundary of the continuum radiation since  $f_g^- \ll f_p^-$  over most of the time interval when the diffuse electrostatic emissions are present. Notice that at about 17 kHz there is an intensification when each of the first 5 diffuse bands intersects the lower edge of the continuum radiation where  $f \sim f_{UHR}$ . The intensification shown here is not as great as reported in the Hawkeye/IMP 6 survey of Chapter II, but the effect is obvious.

Another particularly striking example of intensification occurs in the  $3f_g^-/2$  band. In Plate 5 the upper hybrid resonance band follows the density discontinuity at the plasmopause at about 1110 UT and merges into a diffuse electrostatic band at about  $3f_g^-/2$ . The rectangular region of apparently increased wave amplitudes at about 1140 UT is the result of receiver saturation due to an extremely large signal at about 18 kHz. It is at the intensification at 18 kHz that the  $3f_g^-/2$  band appears to merge with the upper hybrid band. Notice, also, that the intensification occurs very close to the lower edge of the continuum radiation, as in Plate 4. Measurements made by the ISEE 1 Quadrispherical LEPDEA

during the intense wave event shown in Plate 5 have been analyzed to obtain  $f(v, \alpha)$  where  $\alpha$  is the pitch angle. Figure 22 shows the average  $f(v)$  for  $70^\circ < \alpha \leq 90^\circ$ . There are two features in this distribution function which may be related to the intense waves. Near  $2 \times 10^9 \text{ cm (sec)}^{-1}$  a small peak or plateau is seen. This feature persists over the eight-minute interval during which these measurements were made and also extends over a pitch angle range of  $20^\circ \leq \alpha \leq 160^\circ$ . The other feature, near  $6 \times 10^9 \text{ cm (sec)}^{-1}$  or about 10 keV is clearly a feature with a positive slope with respect to  $v_\perp$ . Again, this feature persists in time and over the range  $20^\circ \leq \alpha \leq 160^\circ$  although there is some variation in the height and energy of the "bump" over the range in pitch angles. Pitch angles sufficiently small to detect a loss cone, if present, were not sampled during this time period, but certainly the feature at 10 keV and possibly even the one near 1 keV are potential sources of free energy to drive the intense waves. The feature at  $6 \times 10^9 \text{ cm (sec)}^{-1}$  in Figure 22 is reminiscent of the bump-on-tail suggested in Chapter III by the distribution in Figure 20.

We can use the event displayed in Plate 1 to serve as a basis for a detailed comparison of observations of the intense waves near  $f_{\text{UHR}}$  with the linear instability theory. Plate 1 is an inbound pass through the magnetosphere including intense electrostatic waves at about 2111 UT. The wave amplitude is about  $7 \text{ mV m}^{-1}$  in this case and the receiver becomes saturated. However, the

diffuse electrostatic bands at lower frequencies can be seen before and after the event. Notice that while the event at  $f_{\text{UHR}}$  (approximately 30 kHz) is very intense, the diffuse bands are weak and barely detectable.

The theory, as demonstrated in Figure 21, predicts that for values of  $n_c/n_h$  greater than about 1.5 a single band can become nonconvectively unstable while instabilities in other bands are convective, hence, probably much less intense. This effect can be seen in the lower panel of Figure 23 which illustrates the maximum spatial growth rate as a function of frequency. The abscissa of Figure 23 is frequency normalized to the electron gyrofrequency obtained from measurements of  $|B|$  provided by C. T. Russell [personal communication, 1978]. The plasma model has parameters  $\Delta = 0$  (indicating the loss cone is completely empty),  $\beta = 0.9$ ,  $T_c/T_n = 5 \times 10^{-2}$ , and  $n_c/n_h = 3$ . The parameter  $\beta$  in the Ashour-Abdalla and Kennel [1978a] model is a measure of the width of the loss cone where  $\beta \approx 1$  gives the broadest loss cone, but with a corresponding weak slope. For the growth rate spectrum in Figure 23  $f_{\text{UHC}} = 4.5 f_g^-$ . As expected, the band at  $4 < f/f_g^- < 5$  is nonconvectively unstable. Since the group velocity becomes arbitrarily small at a nonconvective instability the spatial growth rates are unrealistically large. Hence, the growth rates should only be regarded in a qualitative manner.

The upper panel of Figure 23 is a spectrum taken from the event in Plate 1 just prior to the time when the receiver saturates.

Notice that there is very weak wave growth between the lower harmonics of  $f_g^-$  corresponding to the small, convective growth rates in the first three harmonics in Figure 23. As expected, very intense waves are detected between the fourth and fifth harmonics of  $f_g^-$  corresponding to the peak near  $4.7f_g^-$  in Figure 23.

It should be pointed out that the growth rates shown in Figures 21 and 23 are the result of complete searches in wave-number space. The regions of nonconvective instability can be very strong functions of  $k_\perp$  and  $k_\parallel$ . An important output of the theory then, is a prediction of  $k_\perp/k_\parallel$  or  $\theta = \tan^{-1} k_\perp/k_\parallel$ . For the waves near  $f_{UHC}$   $\theta$  is typically  $86^\circ$  to  $88^\circ$ . Measurements such as those done for Figure 6 give  $\theta \gtrsim 80^\circ$ . (See also Figure 8 and Appendix A.)

The bandwidth of the intense waves near  $f_{UHR}$  are approximately 10 percent or less of the center frequency of the waves as described in Chapter II. Theoretical bandwidths are in agreement with this number [Ashour-Abdalla and Kennel, 1978a]. Notice that in Figure 23 the nonconvective band is very sharply peaked in frequency. Further, the theory indicates relatively large bandwidths for the lower, weaker harmonics as seen in the first three bands in Figure 23. The bandwidth of diffuse electrostatic waves is observed to be broader than the intense waves, also [Shaw and Gurnett, 1975].

There exists, then, excellent qualitative agreement between observations of intense waves near  $f_{UHR}$  and the theory of electrostatic cyclotron instabilities. The analysis is not complete, however, until the model distribution function used in the

computations is addressed. The object of such an analysis is to compare the model to those plasma observations in hand and determine, if possible, whether the model is justifiable.

The plasma measurements from Hawkeye 1 presented in Chapter III certainly represent only a small portion of the electron distribution function, but a few features allow significant checks with the theory. Most important, there is evidence in all four distributions shown in Chapter III indicating sources of free energy with which to drive the instability. These are a loss-cone distribution, a temperature anisotropy, and some suggestion of a bump-on-tail in  $f(v_{\perp})$ . The bump-on-tail possibility is supported by the distribution function shown in Figure 22. While the theory has been based on a loss-cone distribution, the other sources of free energy may still be viable for the electrostatic cyclotron instability. However, theoretical consideration of the temperature anisotropy and bump-on-tail distribution must be given before the final judgment can be made.

The loss cone as a source of free energy must be considered to be well justified on the basis of the Hawkeye plasma measurements. Both the orbit 487 and orbit 250 distributions clearly show a loss cone effect. Both show qualities very similar to the model plotted in Figure 17. In fact, the model distribution function plotted in Figure 17 is based directly on the hot distribution of Ashour-Abdalla and Kennel [1978a]:

$$n_h F_h = n_h \frac{\exp(-v_{||}^2/A_{||}^2)}{\pi^{1/2} A_{||}} \left\{ \frac{\Delta}{\pi A_{\perp}^2} \exp\left(\frac{-v_{\perp}^2}{A_{\perp}^2}\right) + \right. \\ \left. \frac{(1-\Delta)}{(1-\beta)} \frac{1}{\pi A_{\perp}^2} \left[ \exp\left(\frac{-v_{\perp}^2}{A_{\perp}^2}\right) - \exp\left(\frac{-v_{\perp}^2}{\beta A_{\perp}^2}\right) \right] \right\} \quad (3)$$

where

- $F_h$  normalized hot electron distribution function;
- $A_{\perp}^2$   $A_{\perp}^2 = 2T_{\perp}^h/m$  ( $T_{\perp}^h$  is the hot electron temperature perpendicular to  $\vec{B}$  and  $m$  is the electron mass);
- $A_{||}^2$   $A_{||}^2 = 2T_{||}^h/m$ ;
- $\Delta$  loss cone fill-in parameter ( $0 \leq \Delta \leq 1$ );
- $\beta$  determines the width of the loss cone ( $0 < \beta < 1$ ).

The model contours in Figure 17 use  $T_{||}^h = 3$  keV,  $T_{\perp}^h = 10$  keV,  $\Delta = 0$ ,  $\beta = 0.9$  and  $n_h = 0.125 \text{ cm}^{-3}$ . Notice that the contours of the model show the same qualitative features as the observed contours of the Hawkeye distributions, except for a bump-on-tail. We must conclude that while modified forms of Equation 3 may give more accurate fits to the observations of the loss cone, the use of Equation 3 in the theory until this time certainly is a reasonable choice.

The other important parameter upon which the theory of the intense upper hybrid waves relies heavily is the ratio  $n_c/n_h$ . The range of values for this ratio which is reasonable for nonconvective instability near  $f_{UHR}$  only is roughly  $1.5 \leq n_c/n_h \leq 10$  for the first four harmonics, as seen in Figure 21. (Hubbard and Birmingham place no upper limit on  $n_c/n_h$  for their ' $f \sim f_p$ ' class of waves.) Obviously, the Hawkeye plasma measurements shown give no information at all on cold electrons. In fact, the definition of "cold" and "hot" electrons must be made carefully in the context of the theory. It is apparent that the theory is based on "cold", ionospheric electrons and "hot" plasma sheet electrons. Ashour-Abdalla and Kennel [1978a] demonstrate that the characteristics of the "cold" population are critical in determining the nonconvective nature of the instability. It is likely that, in practice, the meaning of "cold" will be determined primarily by the energy of resonant electrons. Those electrons colder than the resonant electrons are the "cold" particles of importance here.

With the aforementioned caution in mind, we will present a value of  $n_c/n_h$  for the orbit 487 event based on crude assumptions. The result, for the reasons given above, must be taken with a degree of skepticism. We assume the event in orbit 487 shown in Figure 14 lies near  $f_{UHC} \approx 17.8$  kHz. (We use the somewhat circular argument that the theory predicts maximum wave growth near  $f_{UHC}$ .) The gyrofrequency is about 5.3 kHz and, hence,  $f_{pc}^-$  (the cold

plasma frequency) is about 17 kHz. The value of  $n_c$ , then, is about  $3.6 \text{ cm}^{-3}$ . Using the value of  $n_h$  of  $0.13 \text{ cm}^{-3}$  (based on a crude fit of the distribution in Figure 13 to a Maxwellian)  $n_c/n_h$  is approximately 29. Hence, a very rough determination of  $n_c/n_h$  gives a ratio considerably higher than expected by Figure 21. (For this example  $f_{\text{UHC}}$  is in the third of  $7f_g^-/2$  band.) Obviously, the portion of  $f(v_\perp, v_\parallel)$  which has been used is very limited and we cannot expect reasonable accuracy. The example, though, may indicate that a typical value of  $n_c/n_h$  in the region of the magnetosphere where the intense upper hybrid waves are detected is greater than unity.

The plasma observations presented do not allow a complete justification of the model used in the theory of electrostatic cyclotron emissions, but strong evidence is given which supports the use of a hot loss-cone distribution such as in Equation 3. Very little can be said about other parameters of the model, including  $n_c/n_h$ . A value crudely determined above appears to qualitatively be consistent with the theoretical model, but the nature of the assumptions used in the calculation imply that little weight should be given to this agreement.

More complete distribution functions are becoming available from the ISEE and GEOS satellites which should improve the understanding of the real distribution function immensely. Even so, it will be necessary to carefully consider the meaning of "cold" electrons in the interpretation of these results. In response to the



new observations, the theory will have to adapt to more realistic distribution functions.

## V. DISCUSSION

### A. Intense Electrostatic Waves as a Source of Nonthermal Continuum Radiation

The electrostatic waves described in this thesis are among the most intense plasma waves detected in the magnetosphere of the earth. It is important to consider the possible impact upon the magnetosphere of waves of this magnitude. Hence, we have sought to determine whether or not these waves are perhaps related to the generation of a portion of the earth's radio spectrum. It is reasonable to examine these regions of strong electrostatic waves in connection with the generation of the nonthermal continuum radiation. Gurnett [1975] reported the generation region to be a broad region outside the plasmapause at radial distances between 4.0 and 8.0  $R_E$  and between about 0400 and 1400 hours local time. While this study reveals the intense electrostatic events at all local times, the radial distance range just outside the plasmapause is very similar to that found for the intense electrostatic waves. A significant relation between these intense electrostatic waves and the generation of continuum radiation is found in Gurnett and Frank [1976] in which it is argued that continuum radiation appears to be correlated with intensities of 1 to 20 keV electrons in the

region  $4 \leq L \leq 8$ , similar to the electrons apparently involved in the instability generating the waves near  $f_{UHR}$ .

There are several other reasons to expect these electrostatic waves may be connected with the nonthermal continuum. Gurnett shows a typical spectrum of the continuum radiation (see Figure 4 of Gurnett [1975]) which has a lower frequency cutoff of about 3 kHz defined by the local electron plasma frequency in the magnetospheric cavity in which the lower frequency portion of the radiation is trapped. The upper frequency limit of the feature in Gurnett's spectrum is about 200 kHz. This range in frequency is very similar to the frequencies of the intense electrostatic waves near  $f_{UHR}$  (cf. Figure 5). In fact, a few events were seen in the 178-kHz channels of Hawkeye and IMP 6 but those channels were not included in the search because of the difficulty in distinguishing between the electrostatic waves and auroral kilometric radiation.

Perhaps the most striking evidence suggesting these intense waves are a source for the continuum radiation is shown in Figure 24. An example of an intense wave event is shown in the bottom panel at about 0712 UT centered at about  $4.3 R_E$  from the earth. In the interval from about 0720 to 1145 UT continuum radiation is seen to decrease smoothly in amplitude, presumably as a function of some distance. The center panel is a plot of the power flux of continuum radiation as a function of the distance of the satellite from the earth. We assume that the power flux will decrease as the inverse

square of the distance between the receiver and a simple, compact source. The dashed line represents a function with a geocentric radial distance dependence of  $R^{-2}$ . There is clearly no reason to believe the source for the continuum radiation is centered at the earth based on the center panel. The top panel is another plot of the power flux of the continuum radiation, but as a function of  $(R-R')$  where  $R$  is the position of the satellite and  $R'$  is the position of the intense wave region. We have assumed that the earth, the intense waves and the satellite are collinear for this simple demonstration. The dashed line in the top panel of Figure 24 is a function which is proportional to  $(R-R')^{-2}$ . There is very good agreement between the assumed geometry and the data in this top panel. We have made no attempt to do a least squares fit or to adjust  $R'$  for a better fit. We seek only to demonstrate that the continuum radiation clearly appears to be radiating from a source near  $4.3 R_E$  and that the source is fairly compact.

There are several examples similar to that shown in Figure 24 which strongly suggest the intense waves are a local source of non-thermal continuum radiation (see Gurnett's [1975] Figure 13). Another example of this effect is seen in the IMP 6 orbit 76 event shown in Figure 1. An excellent example, but of different form, is seen in Plate 5. Notice that there is a band of intensified continuum radiation which is at the same frequency as the intense wave event at 1140 UT, but at significantly greater radial distances.

We do not propose to explain the connection between the intense electrostatic band and the intense continuum radiation, but include the example as another piece of evidence suggesting a relation exists. We must say, however, that most events do not display a direct relationship to continuum radiation. The event shown in Figure 11 shows little, if any, continuum radiation which could be related to the intense waves. It is not clear why some events appear to be generating continuum radiation and others do not. Two possible explanations are that either the wave-wave interactions converting electrostatic waves into the electromagnetic mode is sometimes very inefficient or non-existent or there is a propagation effect which dictates regions or directions in which the waves will not propagate. An example of the latter case might be a wave-wave interaction which yields waves strongly beamed in particular directions as defined by wave-vector selection rules for that interaction.

It is not the purpose of this thesis to prove that the intense electrostatic waves reported here are solely responsible for the generation of the nonthermal continuum radiation. We have shown, however, that several features of the electrostatic waves make them a possible source of continuum radiation. The event shown in Figure 24 strongly suggests that intense electrostatic waves are at least secondary sources of nonthermal continuum radiation, even if there are other mechanisms producing the bulk of the electromagnetic radiation.

B. The Implication of Intense Electrostatic Waves  
for the Distributions of Magnetospheric Plasmas

The presence of  $\sim 10 \text{ mV m}^{-1}$  electrostatic waves within the magnetosphere almost certainly implies that electron diffusion should take place as a result of the waves. This is consistent with the work of Lyons [1974] which treats diffusion by electrostatic waves above  $f_g^-$ . The quasi-linear theory of Lyons shows that 1 to 10  $\text{mV m}^{-1}$  electrostatic waves can put 1 to 10 keV electrons on strong diffusion.

The diffusion of hot electrons is only a part of the complete nonlinear problem posed by considering the intense waves near  $f_{\text{UHR}}$ . Since the duration of many of the events is a large fraction of an hour, it is necessary to view the turbulence as a quasi-equilibrium or time-stationary state. That is, the source of free energy, for example, the hot loss cone, must be replenished continually with perhaps the injection of plasma-sheet-like electrons. Simultaneously, it is reasonable to expect that the diffusion of hot electrons may act as a stabilization process, relaxing the non-monotonic distribution function. Alternately, or simultaneously, the cold component may be in a quasi-stationary balance of competing influences. While an influx of cold, ionospheric plasma is taking place, the cold electrons may be both heated and pitch-angle scattered by the electrostatic waves [Ashour-Abdalla *et al.*, 1979]. Hence, we may be measuring waves which have been nonlinearly saturated.

The only nonlinear saturation theory at present is due to Young [1975]. The simultaneously measured distribution functions shown in this work must not only contain the features which are unstable to the electrostatic waves, but will also reflect the result of the nonlinear saturation mechanism.

Unfortunately, the nonlinear nature of the intense electrostatic waves may require the simultaneous solution of the generation mechanism and saturation mechanism (including the diffusion of electrons due to the waves). Hence, an analysis of the impact of the intense waves upon distributions of magnetospheric plasmas will not be straightforward.

## VI. SUMMARY AND CONCLUSIONS

We have described a class of very intense electrostatic waves located at or just outside the plasmapause near the upper hybrid resonance frequency. The waves at amplitudes from  $\sim 1$  to  $20 \text{ mV m}^{-1}$  are only observable in about 10% of the plasmapause crossings made by the Hawkeye 1 and IMP 6 satellites, however, they are among the most intense plasma waves seen in the magnetosphere. The observable characteristics of the waves are:

1. The waves are often very intense,  $> 10 \text{ mV m}^{-1}$ .
2. The waves are narrowband and fluctuate rapidly in intensity.
3. The waves are found at all local times in a magnetic latitude range from the equator to at least  $\pm 50^\circ$ .
4. The waves occur at or just outside the plasmapause and the higher frequency events are found generally at smaller radial distances, i.e., close to the plasmapause.
5. The waves usually lie between harmonics of  $f_g^-$ .
6. The waves also lie near  $f_{\text{UHR}}$ .
7. The waves are polarized such that the wave electric field is perpendicular to the geomagnetic field.
8. There is a small magnetic field component to the waves in many cases, but the electric-to-magnetic field energy density ratio is always very large.



In addition, evidence is given which strongly suggests the wave events are at least secondary sources of nonthermal continuum radiation.

Plasma measurements taken simultaneously with the detection of the intense waves show only a fair correlation with intensities of electrons in the energy range from about 1 to 20 keV. However, all events detected at the magnetic equator when an ample range of pitch angles is sampled show evidence of pitch angle anisotropies in favor of  $\alpha = 90^\circ$ . Measurements of the velocity distribution function for events detected at the magnetic equator reveal two sources of free energy: a loss-cone distribution and a temperature anisotropy with  $T_\perp/T_\parallel > 1$ . There is a suggestion of a third possible source of free energy in the form of a bump-on-tail in  $v_\perp$ .

A possible explanation of the intense electrostatic waves near  $f_{\text{UHR}}$  exists in the theory of multi-cyclotron emissions. Very good qualitative agreement between predictions of the theory and observations of the waves is demonstrated. The theory of the  $(n + 1/2)f_g^-$  emissions indicates that large spatial growth rates can occur in the band including the cold upper hybrid resonance frequency for a range of  $n_c/n_h$  greater than about one. The theory is based on a model distribution function which has many features qualitatively similar to those measured by the Hawkeye and ISEE LEPEDeAs. In particular, the theory is based on a loss-cone free-energy source which is observed simultaneously with several of the intense wave events.

## REFERENCES

- Anderson, R. R., Wave-particle interactions in the evening magnetosphere during geomagnetically disturbed periods, Ph. D. dissertation, Dept. of Physics and Astronomy, University of Iowa, Iowa City, Iowa, 1976.
- Ashour-Abdalla, M., G. Chanteur, and R. Pellat, A contribution to the theory of the electrostatic half-harmonic electron gyrofrequency waves in the magnetosphere, J. Geophys. Res., 80, 2775, 1975.
- Ashour-Abdalla, M., and S. W. H. Cowley, Wave-particle interactions near the geostationary orbit, in Magnetospheric Physics, edited by B. M. McCormac, D. Reidel, Dordrecht, Netherlands, 1974.
- Ashour-Abdalla, M., and C. F. Kennel, VLF electrostatic waves in the magnetosphere, in Physics of the Hot Plasma in the Magnetosphere, edited by B. Hultqvist and L. Stenflo, pp. 201-227, Plenum, New York, 1975.
- Ashour-Abdalla, M., and C. F. Kennel, Nonconvective and convective electron cyclotron harmonic instabilities, J. Geophys. Res., 83, 1531, 1978a.
- Ashour-Abdalla, M., and C. F. Kennel, Multi-harmonic electron cyclotron instabilities, Geophys. Res. Lett., 5, 711, 1978b.
- Ashour-Abdalla, M., C. F. Kennel, and D. D. Sentman, Magnetospheric multi-harmonic instabilities, in Astrophysics and Space Science Book Series, ed. by P. J. Palmadesso, D. Reidel, Dordrecht, Netherlands, 1979.
- Borg, H., L. Å. Holmgren, B. Hultqvist, F. Cambou, H. Reme, A. Bahnsen, and G. Kremser, The keV plasma experiment on GEOS-1 and some early results, 23 pp., Kiruna Geophysical Institute Preprint No. 78:303, 1978.
- Christiansen, P., P. Gough, G. Martelli, J.-J. Block, N. Cornilleau, J. Etcheto, R. Gendrin, D. Jones, C. Béghin, and P. Décréau, GEOS I: Identification of natural magnetospheric emissions, Nature, 272, 682, 1978.

- DeForest, S. E., and C. E. McIlwain, Plasma clouds in the magnetosphere, J. Geophys. Res., 76, 3587, 1971.
- Frank, L. A., Initial observations of low-energy electrons in the earth's magnetosphere with OGO-3, J. Geophys. Res., 72, 185, 1967.
- Frank, L. A., K. L. Ackerson, R. J. DeCoster, and B. G. Burek, Three-dimensional plasma measurements within the earth's magnetosphere, (to be published in Space Science Rev.), 1979.
- Frank, L. A., D. M. Yeager, H. D. Owens, K. L. Ackerson, and M. R. English, Quadrispherical LEPEDeAs for ISEE's-1 and -2 plasma measurements, Geoscience Electronics, GE-16, 221, 1978.
- Fredricks, R. W., Plasma instability at  $(n + 1/2)f_c$  and its relationship to some satellite observations, J. Geophys. Res., 76, 5344, 1971.
- Fredricks, R. W., and F. L. Scarf, Recent studies of magnetospheric electric field emissions above the electron gyrofrequency, J. Geophys. Res., 78, 310, 1973.
- Gregory, P. C., Satellite observations of magnetospheric radio noise 1. Emissions between the plasma and upper hybrid resonance frequencies, Planet. Space Sci., 19, 813, 1971.
- Gurnett, D. A., The earth as a radio source: The nonthermal continuum, J. Geophys. Res., 80, 2751, 1975.
- Gurnett, D. A., R. R. Anderson, F. L. Scarf, R. W. Fredricks, and E. J. Smith, Initial results from the ISEE-1 and -2 plasma wave investigation, (to be published in Space Science Rev.), 1979.
- Gurnett, D. A., and L. A. Frank, Continuum radiation associated with low-energy electrons in the outer radiation zone, J. Geophys. Res., 81, 3875, 1976.
- Gurnett, D. A., and L. A. Frank, A region of intense plasma wave turbulence on auroral field lines, J. Geophys. Res., 82, 1031, 1977.
- Gurnett, D. A., F. L. Scarf, R. W. Fredricks, and E. J. Smith, The ISEE-1 and ISEE-2 plasma wave investigation, Geoscience Electronics, GE-16, 225, 1978.

- Gurnett, D. A., and R. R. Shaw, Electromagnetic radiation trapped in the magnetosphere above the plasma frequency, J. Geophys. Res., 78, 8136, 1973.
- Harris, E. G., Unstable plasma oscillations in a magnetic field, Phys. Rev. Lett., 2, 34, 1959.
- Hubbard, R. F., and T. J. Birmingham, Electrostatic emissions between electron gyroharmonics in the outer magnetosphere, J. Geophys. Res., 83, 4837, 1978a.
- Hubbard, R. F., and T. J. Birmingham, Magnetospheric electrostatic emissions and cold plasma densities, (submitted to J. Geophys. Res.), 1978b.
- Karpman, V. I., Ju. K. Alekhin, N. D. Borisov, and N. A. Rjabova, Electrostatic waves with frequencies exceeding the gyro-frequency in the magnetosphere, Astrophys. and Space Sci., 22, 267, 1973.
- Karpman, V. I., Ju. K. Alekhin, N. D. Borisov, and N. A. Rjabova, Electrostatic electron cyclotron waves in plasma with a loss cone distribution, Plasma Phys., 17, 361, 1975.
- Kennel, C. F., F. L. Scarf, R. W. Fredricks, J. H. McGehee, and F. V. Coroniti, VLF electric field observations in the magnetosphere, J. Geophys. Res., 75, 6136, 1970.
- Kurth, W. S., M. M. Baumback, and D. A. Gurnett, Direction-finding measurements of auroral kilometric radiation, J. Geophys. Res., 80, 2764, 1975.
- Lyons, L. R., Electron diffusion driven by magnetospheric electrostatic waves, J. Geophys. Res., 79, 575, 1974.
- Mosier, S. R., M. L. Kaiser, and L. W. Brown, Observations of noise bands associated with the upper hybrid resonance by the IMP 6 radio astronomy experiment, J. Geophys. Res., 78, 1673, 1973.
- Scarf, F. L., R. W. Fredricks, C. F. Kennel, and F. V. Coroniti, Satellite studies of magnetospheric substorms on August 15, 1968, J. Geophys. Res., 78, 3119, 1973.
- Schild, M. A., and L. A. Frank, Electron observations between the inner edge of the plasma sheet and the plasmasphere, J. Geophys. Res., 75, 5401, 1970.

- Shaw, R. R., and D. A. Gurnett, Electrostatic noise bands associated with the electron gyrofrequency and plasma frequency in the outer magnetosphere, J. Geophys. Res., 80, 4259, 1975.
- Shaw, R. R., and D. A. Gurnett, The low-frequency cutoffs of non-thermal continuum radiation: Comments on 'source of terrestrial non-thermal radiation' by D. Jones, University of Iowa Research Report 78-14, 30 p., 1978.
- Stix, T. H., The Theory of Plasma Waves, McGraw-Hill, New York, 1962.
- Taylor, W. W. L., and S. D. Shawhan, A test for incoherent Cerenkov radiation for VLF hiss and other magnetospheric emissions, J. Geophys. Res., 79, 105, 1974.
- Young, T. S. T., Destabilization and wave-induced evolution of the magnetospheric plasma clouds, J. Geophys. Res., 80, 3995, 1975.
- Young, T. S. T., J. D. Callen, and J. E. McCune, High-frequency electrostatic waves in the magnetosphere, J. Geophys. Res., 78, 1082, 1973.

## APPENDIX A: POLARIZATION DETERMINATION

The method of polarization determination described here is a general analysis of the response of a rotating dipole to an arbitrarily oriented, instantaneous electric field of magnitude  $|\vec{E}|$ . Since wave-vectors,  $\vec{k}$ , are not measured, but only components of  $\vec{E}_0$ , we must define this "polarization" determination more crudely than the generally accepted standard. To arrive at a true polarization, assumptions must be made about the wave mode. For example, an electrostatic wave with  $\vec{E}_0 \perp \vec{B}_0$  where  $\vec{B}_0$  is the geomagnetic or stationary magnetic field will give the same result in this analysis as a circularly or randomly polarized electromagnetic wave propagating in the extraordinary mode. With this precautionary statement, we shall begin by transforming the electric field into the coordinate system of the spacecraft and its dipole antenna. Then, we will specialize to the point of assuming that measurements are only available along the axis defined by the antenna (i.e., there is only one antenna on board). An assumption will then be made which eliminates azimuthal dependence from the problem. Finally, the results will be interpreted in terms of an electrostatic wave assumption.

The sketch at the top of Figure 8 defines the coordinate systems used in this analysis. The static magnetic field forms the basis of the coordinate system in which we wish to know  $\vec{E}_0$ . The  $\hat{z}$  axis is parallel to  $\vec{B}_0$  and  $\hat{x}$  and  $\hat{y}$  are arbitrarily chosen, but with  $\hat{x} \times \hat{y} = \hat{z}$ .  $\vec{E}_0$  lies at a polar angle,  $\theta$ , with respect to  $\hat{z}$

(or  $\vec{B}_0$ ) and at an azimuthal angle,  $\varphi$ , measured in the positive sense from the  $+\hat{x}$  direction. ( $\varphi$  is not shown in Figure 8 in order to minimize confusion in that figure.)

Our primary goal is to transform, by a pair of Euler rotations,  $\vec{E}_0$  into a coordinate system defined by the angular momentum vector,  $\vec{\omega}$ , of the spacecraft ( $\hat{z}'$ ) and the dipole antenna axis ( $\hat{x}'$ ):

$$\vec{E}'_0 = \lambda_{\approx 2} \lambda_{\approx 1} \vec{E}_0 \quad (4)$$

where  $\lambda_{\approx 1}$  and  $\lambda_{\approx 2}$  are Euler transformation matrices.

The first rotation is about the  $\hat{x}$  axis in a negative sense by an angle  $\beta$ :

$$\lambda_{\approx 1} = \begin{pmatrix} 1 & 0 & 0 \\ 0 & \cos\beta & -\sin\beta \\ 0 & \sin\beta & \cos\beta \end{pmatrix} .$$

The second rotation is about the  $\hat{z}'$  or  $\vec{\omega}$  axis by an angle  $\delta$  in the positive sense:

$$\lambda_{\approx 2} = \begin{pmatrix} \cos\delta & \sin\delta & 0 \\ -\sin\delta & \cos\delta & 0 \\ 0 & 0 & 1 \end{pmatrix} .$$



The total transformation matrix,  $\lambda$ , then, is:

$$\lambda = \lambda_2 \lambda_1 = \begin{pmatrix} \lambda_{11} & \lambda_{12} & \lambda_{13} \\ \lambda_{21} & \lambda_{22} & \lambda_{23} \\ \lambda_{31} & \lambda_{32} & \lambda_{33} \end{pmatrix}$$

with

$$\lambda_{11} = \cos\delta$$

$$\lambda_{12} = \sin\delta\cos\beta$$

$$\lambda_{13} = -\sin\delta\sin\beta$$

$$\lambda_{21} = -\sin\delta$$

$$\lambda_{22} = \cos\delta\cos\beta$$

$$\lambda_{23} = -\cos\delta\sin\beta$$

$$\lambda_{31} = 0$$

$$\lambda_{32} = \sin\beta$$

$$\lambda_{33} = \cos\beta$$

The instantaneous electric field in the magnetic coordinate system is:

$$\vec{E}_O = \begin{pmatrix} E_O \sin\theta \cos\varphi \\ E_O \sin\theta \sin\varphi \\ E_O \cos\theta \end{pmatrix} .$$

By Equation 4, then, the elements of  $\vec{E}'_O$  are:

$$E'_{Ox} = E_O \sin\theta \cos\varphi \cos\delta + E_O \sin\theta \sin\varphi \sin\delta \cos\beta - E_O \cos\theta \sin\delta \sin\beta \quad (5a)$$

$$E'_{Oy} = -E_O \sin\theta \cos\varphi \sin\delta + E_O \sin\theta \sin\varphi \cos\delta \cos\beta - E_O \cos\theta \cos\delta \sin\beta \quad (5b)$$

$$E'_{Oz} = E_O \sin\theta \sin\varphi \sin\beta + E_O \cos\theta \cos\beta \quad (5c)$$

We now assume the electric antenna is aligned along the spacecraft  $\hat{x}$  axis and  $\delta$  varies with time as the spacecraft spins about  $\vec{\omega}$ . Hence, Equation 5a gives the component of  $\vec{E}_O$  measured as a function of  $\delta$  (or time) and  $\beta$ . This result is correct for an instantaneous electric field  $\vec{E}_O$ . Further, if an assumption of linear polarization applies, Equation 5a is directly applicable.

In most cases, however, a time average of  $\vec{E}_O$  will show little  $\varphi$  dependence, in the absence of factors such as density gradients which could eliminate an azimuthal symmetry. A good example would be an electromagnetic wave with  $\hat{k} \parallel \hat{B}_O$  which is circularly polarized.

A time average of such a wave's electric field would show no azimuthal dependence, assuming  $\vec{B}_0$  is imbedded in an isotropic medium. Of greater interest to this thesis are electrostatic waves ( $\vec{k} \parallel \vec{E}_0$ ) which propagate at an angle,  $\theta$ , with respect to  $\vec{B}_0$ . We have no reason to expect azimuthal asymmetry, hence, the response measured by the dipole receiver averaged over a large number of waves would be expected to be equivalent to the response to a conical locus of electric field vectors as indicated by the dashed cone in Figure 8. The response is obtained by summing the power at each azimuthal angle,  $\phi$ .

The next step, then, is to obtain a quantity proportional to the power of the wave by simply squaring  $\vec{E}_0$ . Hence, squaring  $E'_{ox}$  we obtain:

$$\begin{aligned}
 (E'_{ox})^2 = & E_0^2 \sin^2 \theta \cos^2 \phi \cos^2 \delta + \\
 & E_0^2 \sin^2 \theta \sin^2 \phi \sin^2 \delta \cos^2 \beta + \\
 & E_0^2 \cos^2 \theta \sin^2 \delta \sin^2 \beta + \\
 & 2E_0^2 \sin^2 \theta \cos \phi \sin \phi \cos \delta \sin \delta \cos \beta - \\
 & 2E_0^2 \sin \theta \cos \theta \sin \phi \sin^2 \delta \sin \beta \cos \beta - \\
 & 2E_0^2 \sin \theta \cos \theta \cos \phi \sin \delta \cos \delta \sin \beta
 \end{aligned} \tag{6}$$

Now, we sum contributions at various angles,  $\varphi$ , by integrating from 0 to  $2\pi$ . Notice that the last three terms in Equation 6 are zero when integrated over the limits 0 to  $2\pi$ :

$$\begin{aligned} \frac{1}{2\pi} \int_0^{2\pi} (E'_{ox})^2 d\varphi &= \frac{E_o^2}{2\pi} \cos^2 \theta \sin^2 \delta \sin^2 \beta \int_0^{2\pi} d\varphi + \\ &\quad \frac{E_o^2}{2\pi} \sin^2 \theta \cos^2 \delta \int_0^{2\pi} \cos^2 \varphi d\varphi + \\ &\quad \frac{E_o^2}{2\pi} \sin^2 \theta \cos^2 \beta \sin^2 \delta \int_0^{2\pi} \sin^2 \varphi d\varphi \end{aligned}$$

which yields

$$\begin{aligned} (E'_{ox})^2 &= E_o^2 (\cos^2 \theta \sin^2 \delta \sin^2 \beta + \frac{1}{2} \sin^2 \theta \cos^2 \delta + \\ &\quad \frac{1}{2} \sin^2 \theta \cos^2 \beta \sin^2 \delta) \end{aligned} \quad (7)$$

Equation 7 represents the electric field measured with an electric dipole antenna rotating about an axis which is at an angle  $\beta$  with respect to the geomagnetic field.

An analysis of Equation 7 may be performed to find the local maxima and minima of the function as the spacecraft spins. By taking the first and second derivatives with respect to  $\delta$  it is seen that the maxima and minima lie at 0 or  $\pi/2$ . In particular, when  $\theta \leq \pi/4$

the minima occur when  $\delta = 0$  (and  $\pi$ ) and the maxima occur at  $\delta = \pi/2$  (and  $3\pi/2$ ). Conversely, if  $\theta$  is closer to  $\pi/2$  (i.e.,  $\pi/4 \leq \theta \leq \pi/2$ ) the minimum occurs at  $\delta = \pi/2$  and the maximum is at 0.

Detailed information about the angle,  $\theta$ , can only be deduced from the depth of the spin modulation nulls. For example, setting  $\delta = 0$  and  $\pi/2$  in Equation 7 and dividing the two gives the result:

$$\theta = \tan^{-1} \left( \sqrt{2} \frac{E_{\perp}}{E_{\parallel}} \sin\beta \right) \quad (8)$$

where  $E_{\perp}$  is the component of the field measured at  $\delta = 0$  and  $E_{\parallel}$  is the component measured at  $\delta = \pi/2$ . We can understand this form if we interpret the  $\sin\beta$  factor as a correction based on the orientation of the spin axis, since the factor is one when the spin axis is perpendicular to  $\vec{B}_0$ . We would expect to arrive at the best determination of  $\theta$  if the entire range of components of  $(\vec{E}_0)^2$  from perpendicular to parallel to  $\vec{B}_0$  can be measured. This can only be achieved if  $\beta$  is  $\pi/2$ . The factor of  $\sqrt{2}$  comes from the integration over  $\varphi$ . We have summed over many wave vectors randomly distributed in azimuth, thus giving a magnitude greater than an individual vector.

We can now interpret the measurements shown in the lower panel of Figure 8. Since we do not a priori know  $|E_0|$  we must leave that as a parameter to be determined from the data. Equation 7 may be written:

$$\frac{\left(\frac{E'_{ox}}{E^2}\right)^2}{\langle E^2 \rangle} = C^2(\cos^2 \theta \sin^2 \delta \sin^2 \beta + \frac{1}{2} \sin^2 \theta \cos^2 \delta + \frac{1}{2} \sin^2 \theta \cos^2 \beta \sin^2 \delta) \quad (9)$$

where we have chosen  $\langle E^2 \rangle \equiv C^2 E_0^2$  and defined that  $\langle E^2 \rangle$  represent some time-averaged spectral density. In practice, we have normalized the data in Figure 8 by dividing by the average spectral density for all points sampled within time intervals approximately one minute in length. The usefulness of this averaging procedure is twofold: first, the data are normalized to correspond to the functional form of Equation 8; and second, amplitude fluctuations with time scales of minutes will not affect the analysis.

To obtain  $\theta$  (and  $C^2$ , if that is of interest) a least-squares fit of the data to the function in Equation 9 is performed, substituting the proper value for  $\beta$  during the time interval. In the case of Figure 8,  $\beta$  varied by only a few degrees, hence, the median value was used. The result of the least-squares fit is  $\theta = 81^\circ$ . We caution, however, that there are unsymmetrical errors in this determination. The depth of the null becomes crucial as  $\theta$  approaches  $90^\circ$  since according to Equation 8,  $E_\perp/E_\parallel$  approaches infinity. Hence, small errors in  $E_\parallel$  will have a profound effect on  $\theta$ . At the same time, it is apparent that errors in the other direction will not be as important, since  $E_\perp/E_\parallel$  will assume a smaller value, not as sensitive to  $E_\parallel$ . We, therefore, interpret the analysis of the data in Figure 8 as being consistent with  $\theta \geq 80^\circ$ .

## APPENDIX B: PLATES

Plate 1      A typical example of intense waves near  $f_{UHR}$  can be seen at about 2110 UT. This event occurs at about 12.7 hours magnetic local time and at a magnetic latitude of  $6.9^\circ$ . The band at  $f_{UHR}$  can be traced from within the plasmasphere at high frequencies out through the plasmopause and into the outer magnetosphere near the lower cut-off of the nonthermal continuum radiation. Also seen are weak, diffuse electrostatic bands between harmonics of the gyrofrequency, below the upper hybrid band.



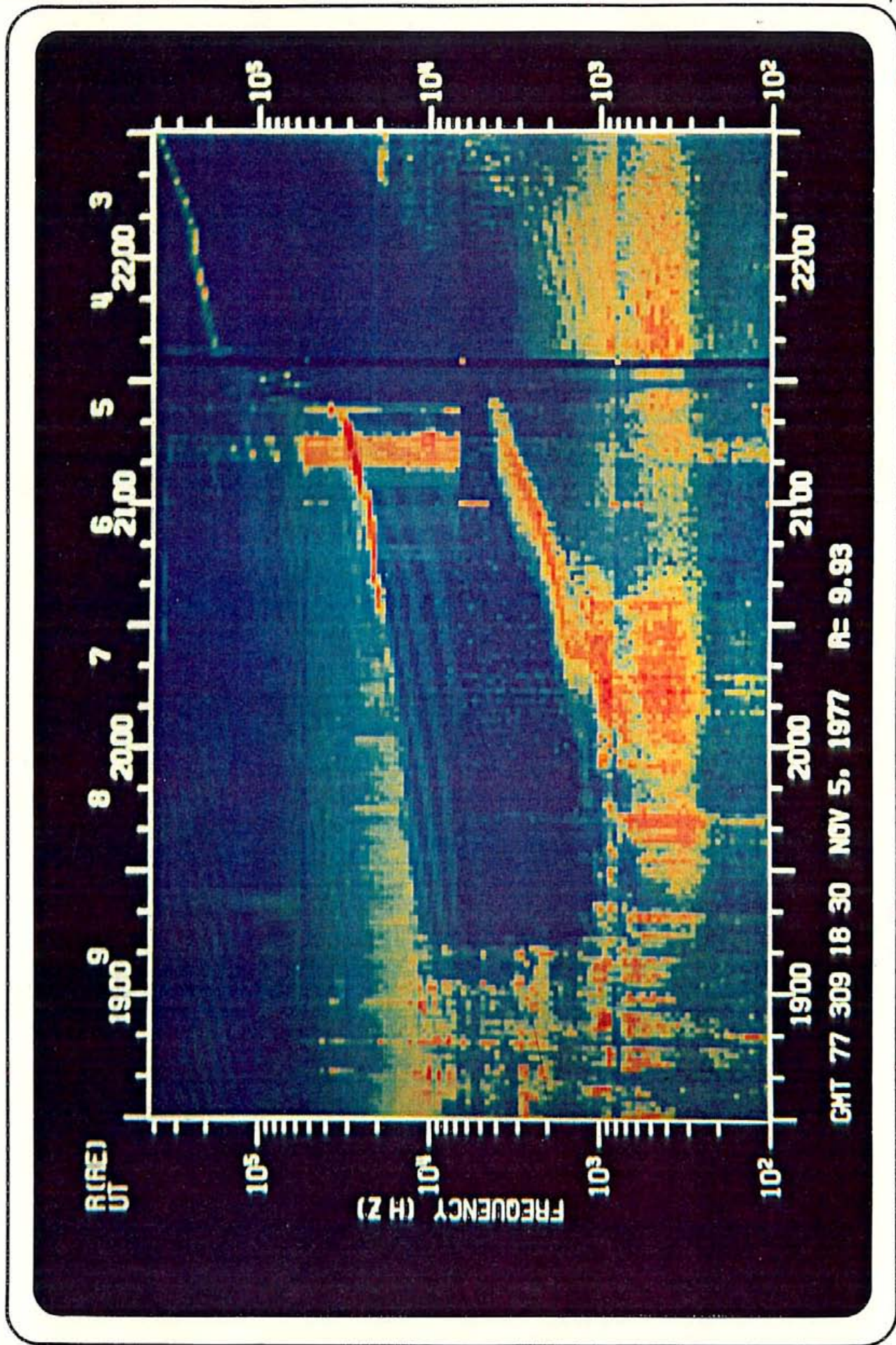


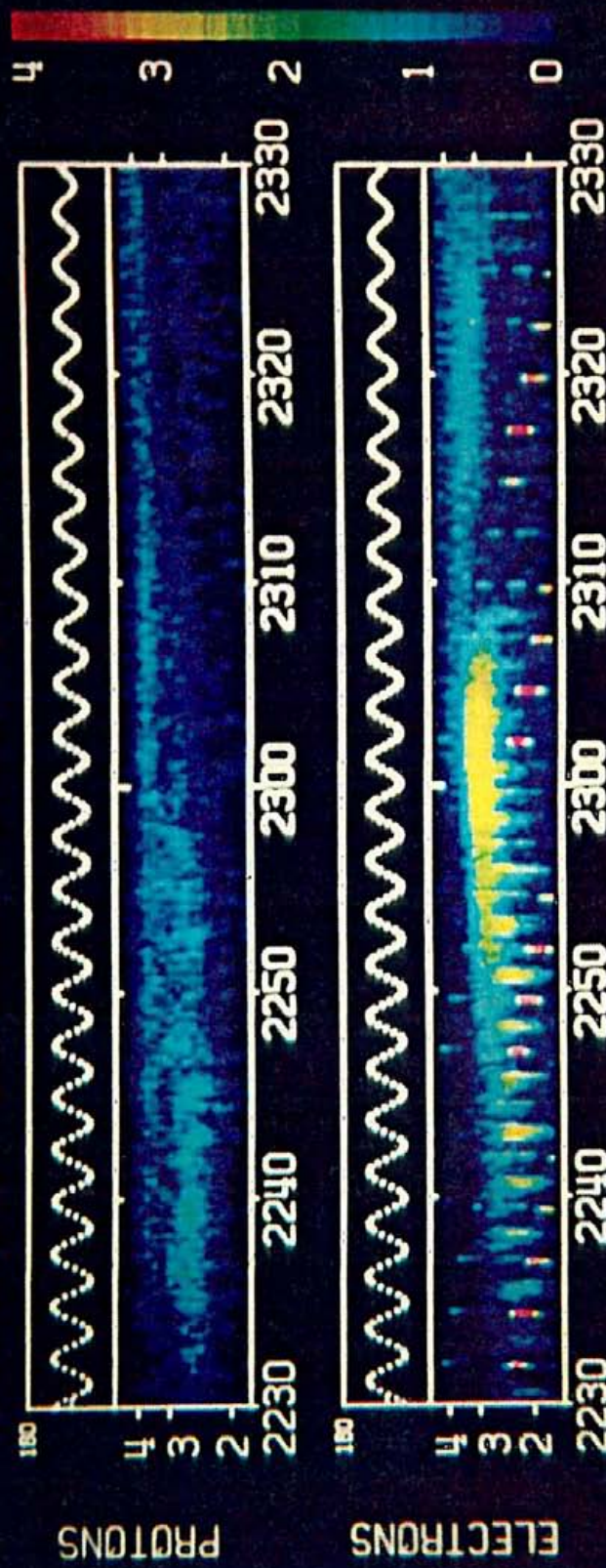
Plate 1

Plate 2

A plasma energy-time spectrogram obtained during the high latitude wave event shown in Figure 11. While incomplete pitch angle coverage does not allow an analysis of pitch angle anisotropy, the time correlation of the electron intensities at about 1 keV with the intense electrostatic waves seen in Figure 11 is very good.



HAWKEYE 1 LEPEDA ORBIT 324 76/114 (23 APR)



GM TUBE	2230	2240	2250	2300	2310	2320	2330
HARMN	5.7	5.4	5.1	4.8	4.4	4.1	
RE	79.0	77.7	76.2	74.5	72.4	70.1	
INV	16.5	16.6	16.6	16.6	16.6	16.7	
MLT							

Plate 3      A plasma energy-time spectrogram obtained during the intense electrostatic wave event shown in Figure 12. Since this event lies at the equator, nearly complete sampling in pitch angle is possible. Note the very anisotropic electron signature at about 1 keV between 2200 and 2210 UT.



# HAWKEYE 1 LEPEDA ORBIT 205 75/227 (15 AUG)

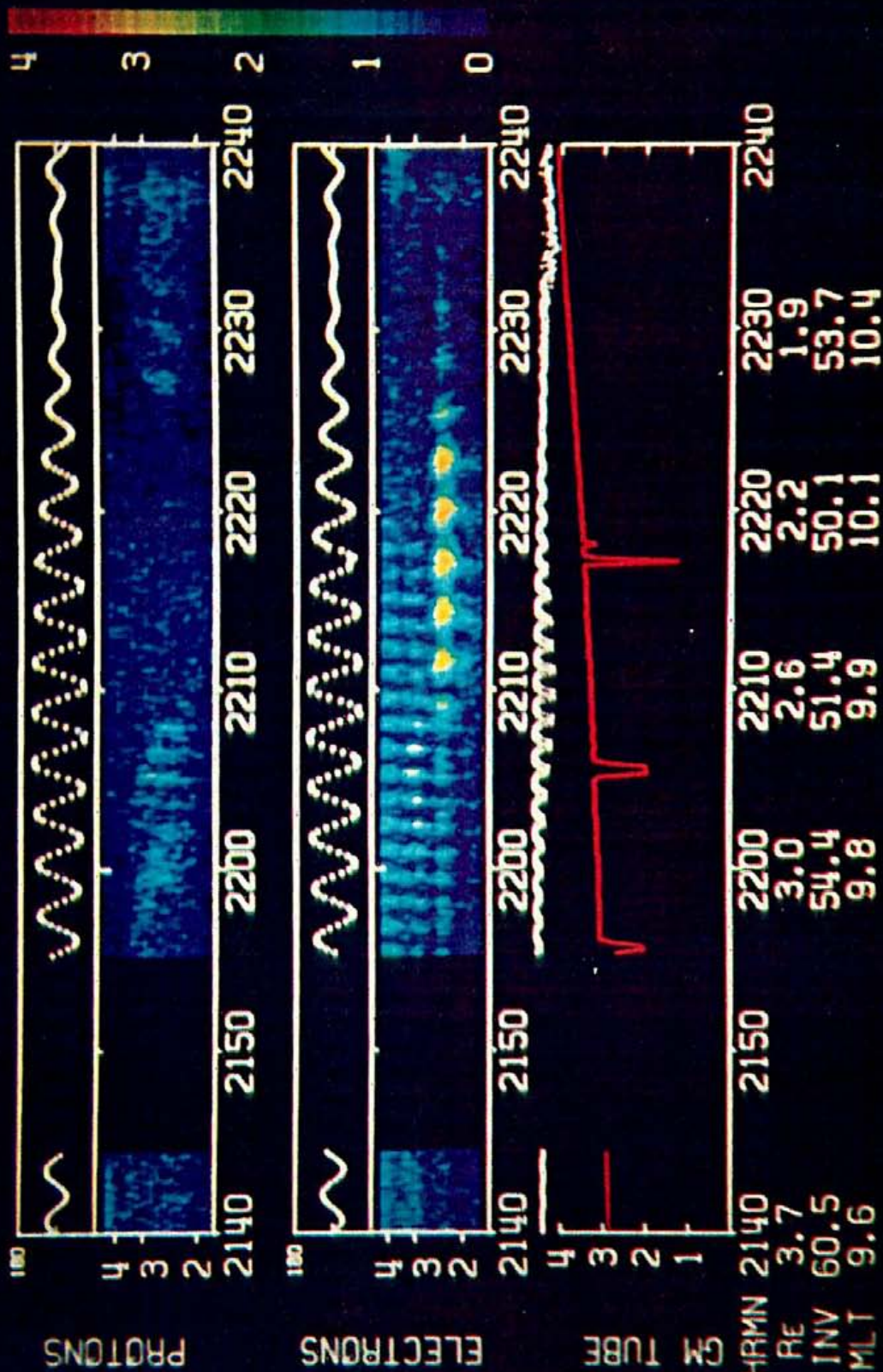


Plate 4      A demonstration of the intensification near  $f_{\text{UHR}}$  at  $(n + 1/2)f_g^-$  bands. In this outbound pass of the ISEE 1 satellite one can see intensifications as each of the first five  $(n + 1/2)f_g^-$  bands approaches  $f_{\text{UHR}}$  near the lower edge of the non-thermal continuum radiation. This pass is at about 6 hours magnetic local time and near  $20^\circ$  magnetic latitude.



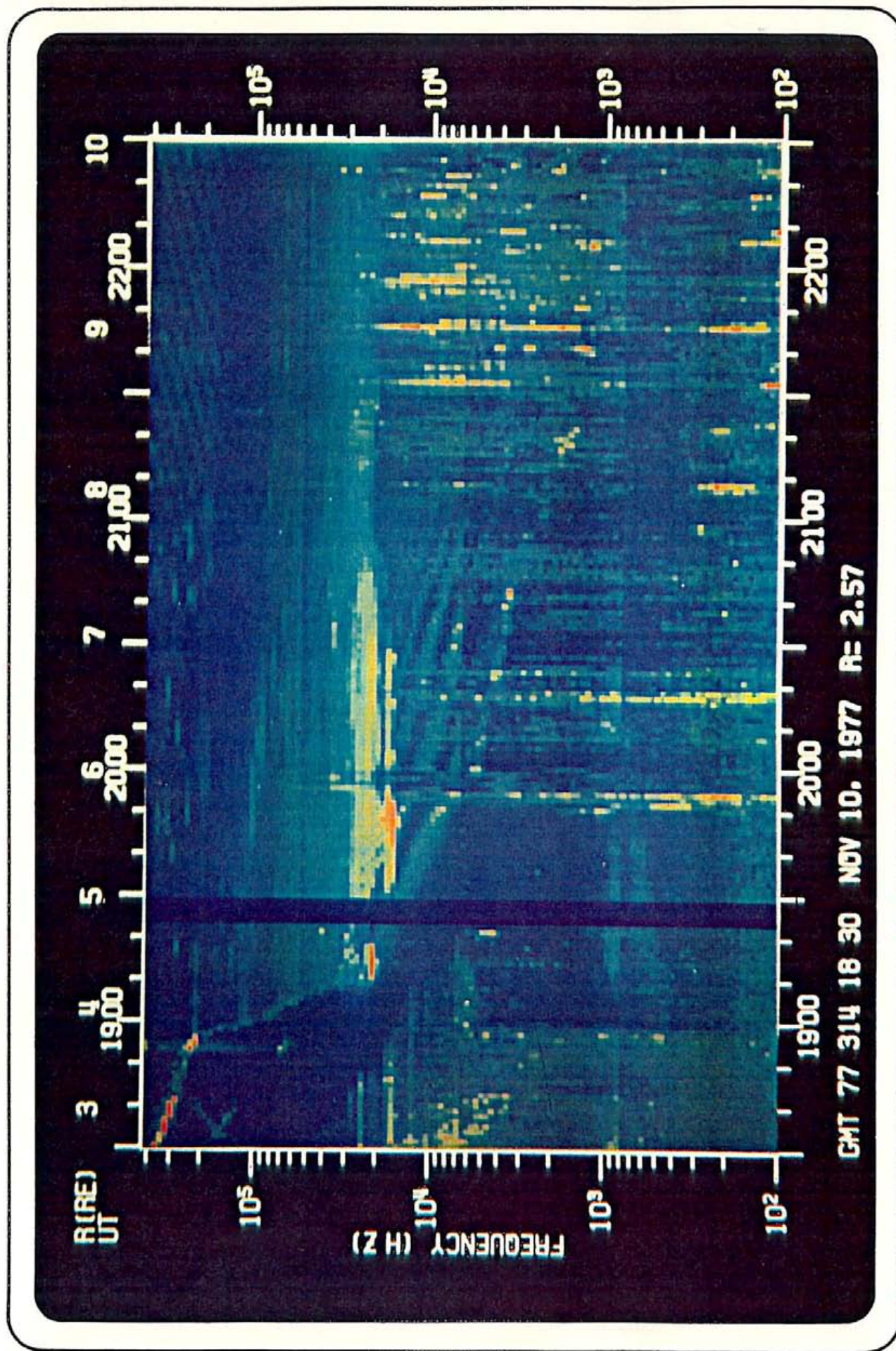


Plate 4

Plate 5      A striking example showing an intensification as the band at  $f_{\text{UHR}}$  merges with the  $3f_g^-/2$  band. Notice, also, the intensification in the non-thermal continuum radiation at about  $7 R_E$  at the same frequency as the intense electrostatic waves, suggesting a possible relation between the two. This intense event occurs at 3.8 hours MLT and at  $38.1^\circ$  magnetic latitude.



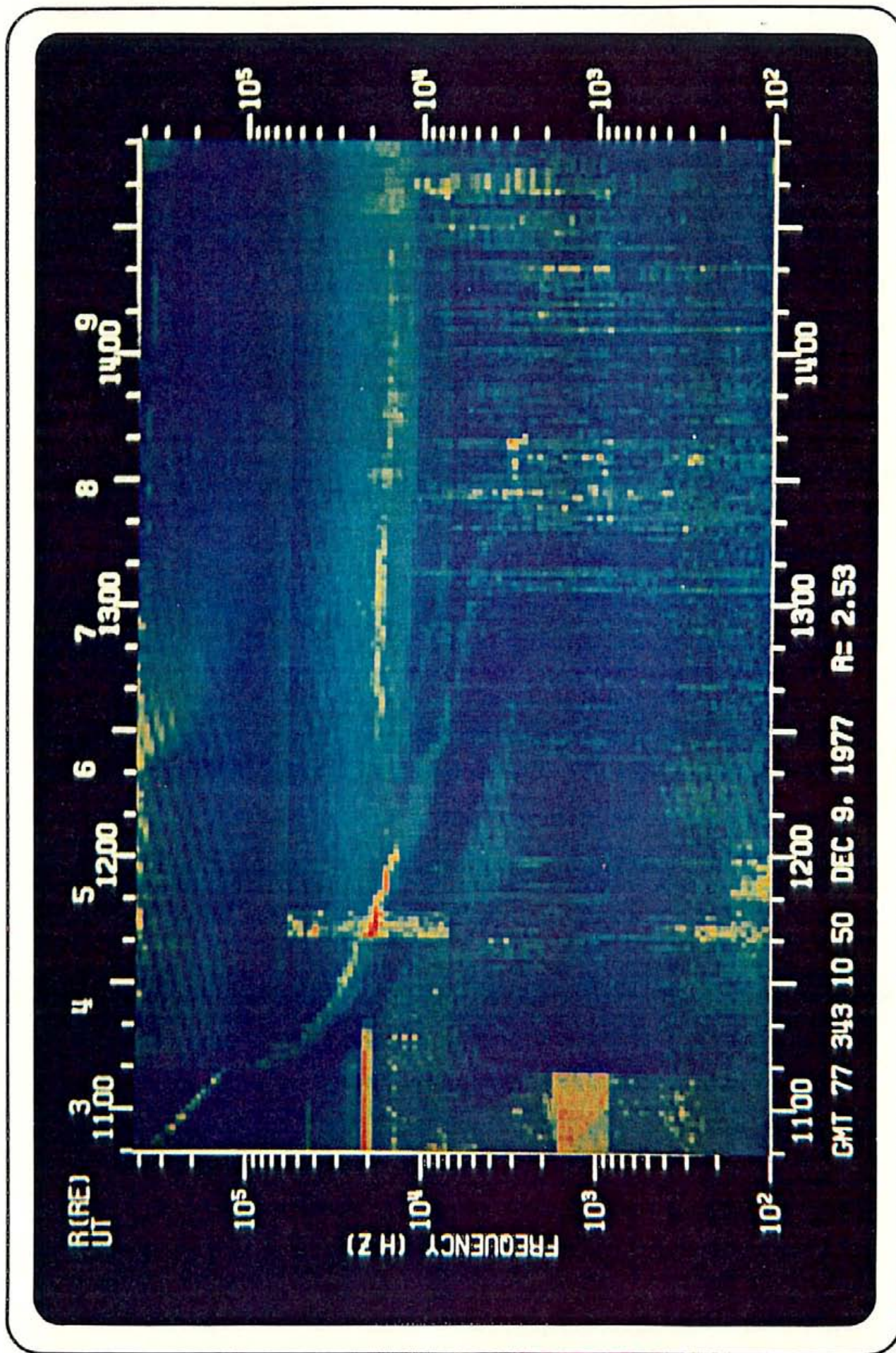


Plate 5

## APPENDIX C: FIGURES

Figure 1      An example of intense electrostatic waves detected just at the plasmopause by the University of Iowa plasma wave instrument onboard the IMP 6 satellite. The solid black areas have a vertical extent proportional to the logarithm of the average electric field strength during 5.11 second averaging intervals. The dots indicate the peak electric field detected during the same interval. The dashed line labeled  $f_{\text{UHR}}$  illustrates the expected trend of the upper hybrid frequency as a function of time if one assigns a frequency scale to the ordinate so that the baseline of each channel defines that channel's frequency on the scale.

D-G77-273-2

IMP 6, ORBIT 76, JAN. 18, 1972

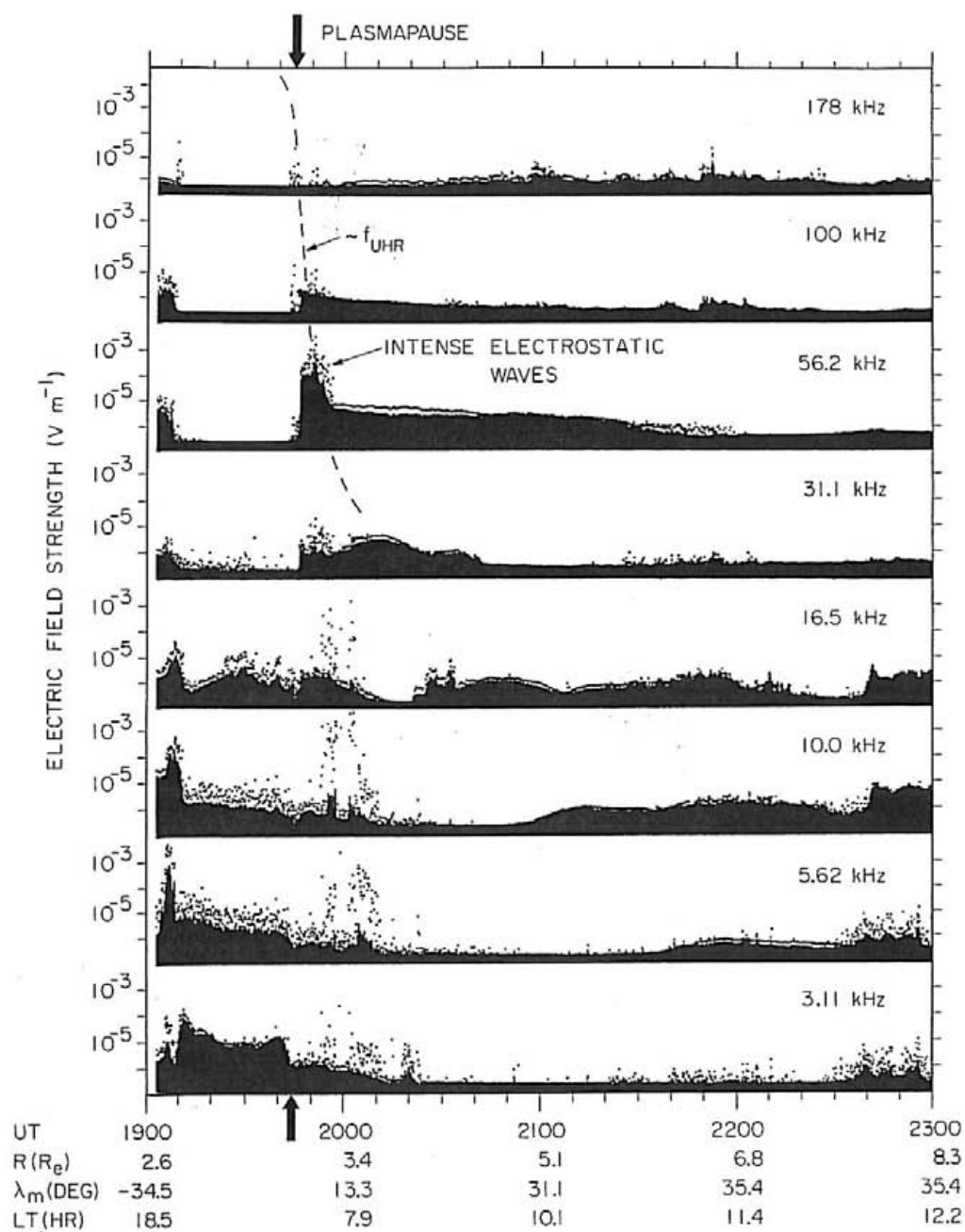


Figure 1

Figure 2      The electric field spectrum of the intense electrostatic wave event shown in Figure 1. Notice the intense waves are sharply peaked at 56.2 kHz and the peak-to-average ratio is about 30, indicating large fluctuations in intensity on a time scale of a few seconds.

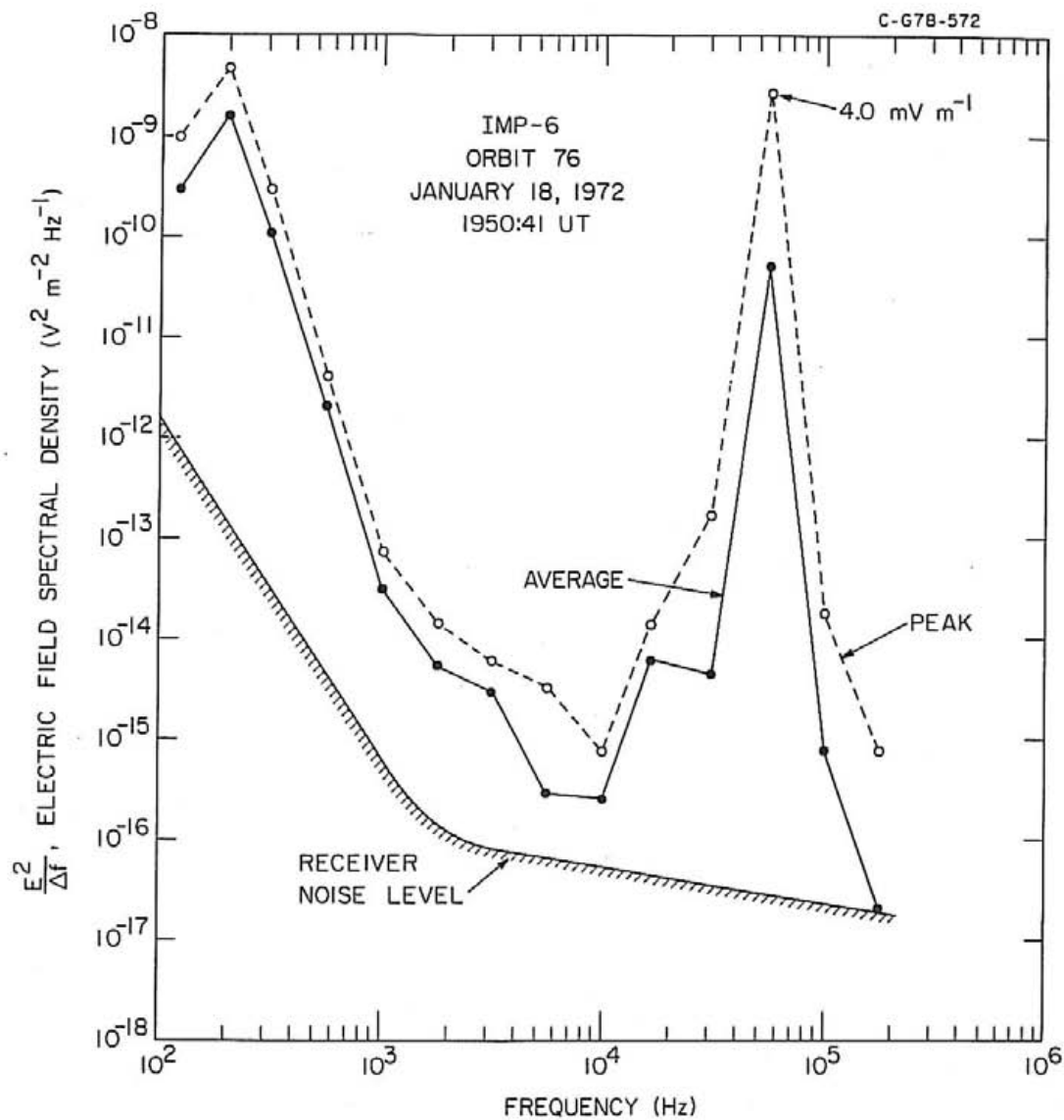


Figure 2

Figure 3      Another example of intense waves as measured by the IMP 6 instrument. This event is approximately  $0.5 R_E$  outside the plasmapause. The magnetic spectrum analyzer data shown in the lower panel indicate the presence of a relatively small magnetic component for this event. The ratio of the electric-to-magnetic field energy densities in this example is about 1600.



D-G77-225-1

IMP 6, ORBIT 202, JUNE 24, 1973

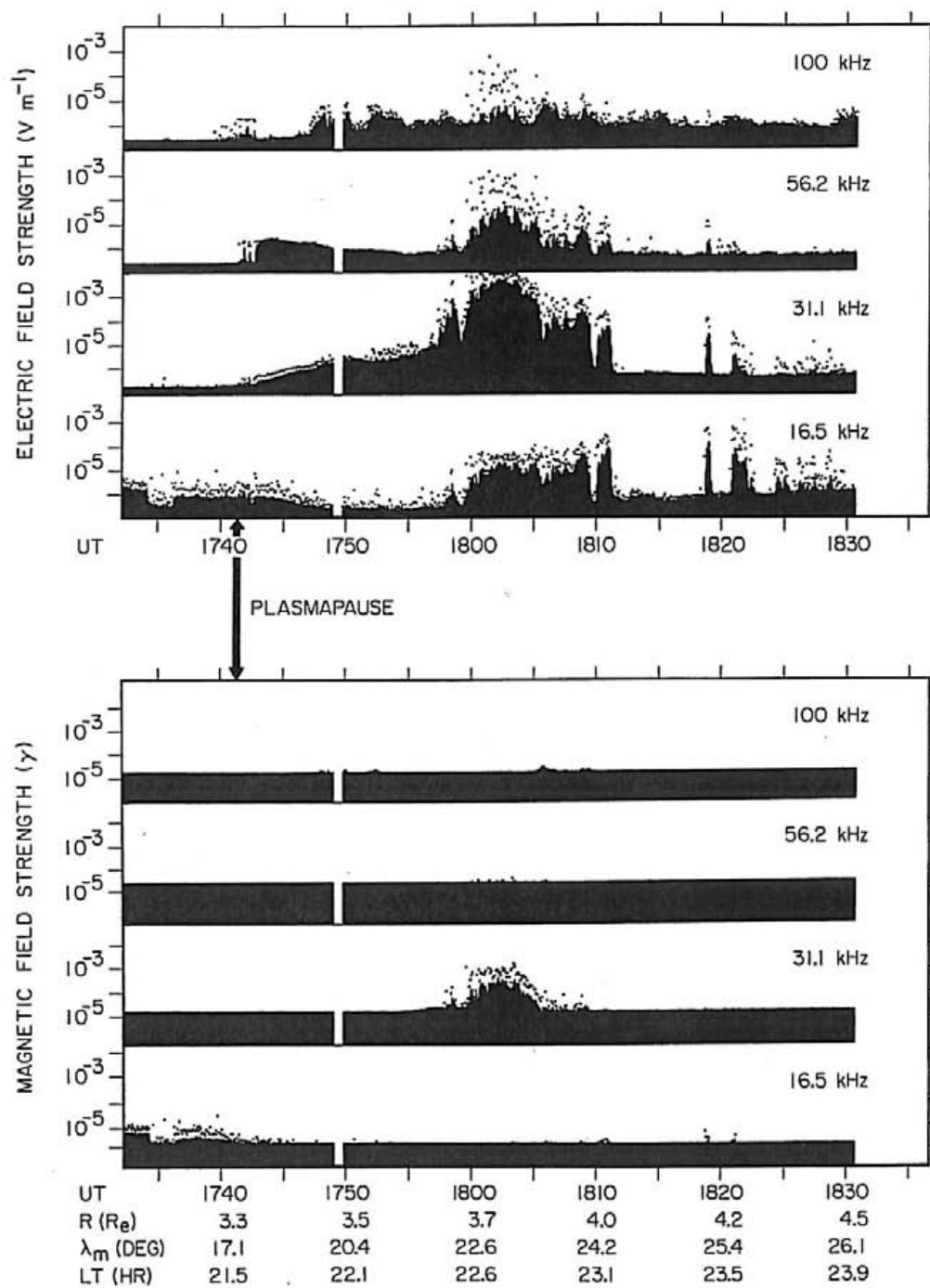


Figure 3



Figure 4 This is a display of all the intense electrostatic wave events ( $|\vec{E}| \geq 1 \text{ mV m}^{-1}$ ) detected during over five and one-half years of observations with the Hawkeye 1 and IMP 6 satellites. Each of four quadrants in magnetic local time are rotated into the noon-midnight and dawn-dusk magnetic meridian planes shown here. Notice the wide range of latitudes at which the intense waves are detected. The events also occur at all local times.

C-678-214

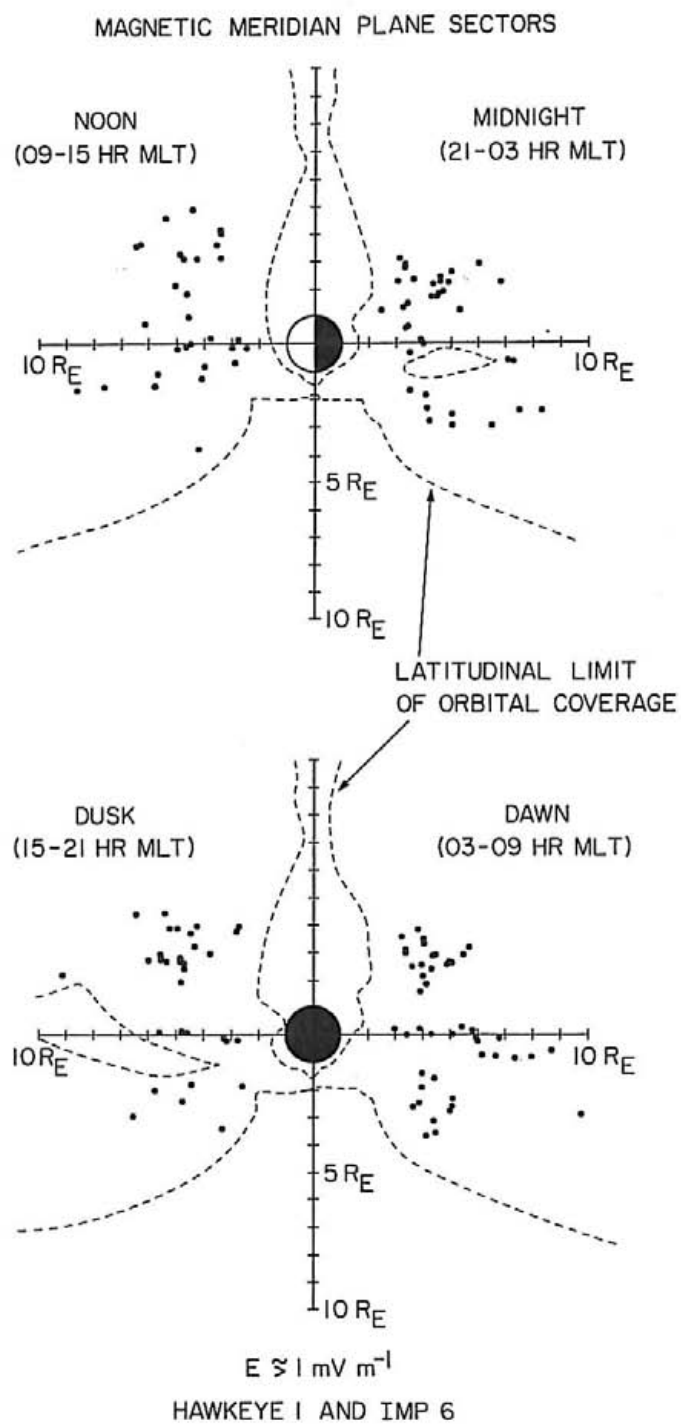


Figure 4

Figure 5 A series of histograms showing the number of intense electrostatic wave events with electric field amplitudes greater than about  $1 \text{ mV m}^{-1}$  as a function of radial distance. Each histogram represents the events detected at each of six different frequencies. The histogram labeled " $\sim 10 \text{ kHz}$ " comprises events from IMP 6's 10-kHz channel and Hawkeye's 13.3-kHz channel and the histogram labeled " $\sim 17 \text{ kHz}$ " combines the events from the 16.5- and 17.8-kHz channels from IMP 6 and Hawkeye 1, respectively. Notice the trend towards lower frequencies at greater distances, implying that the instability is closely related to either  $f_{\text{UHR}}$  or  $f_p^-$ .

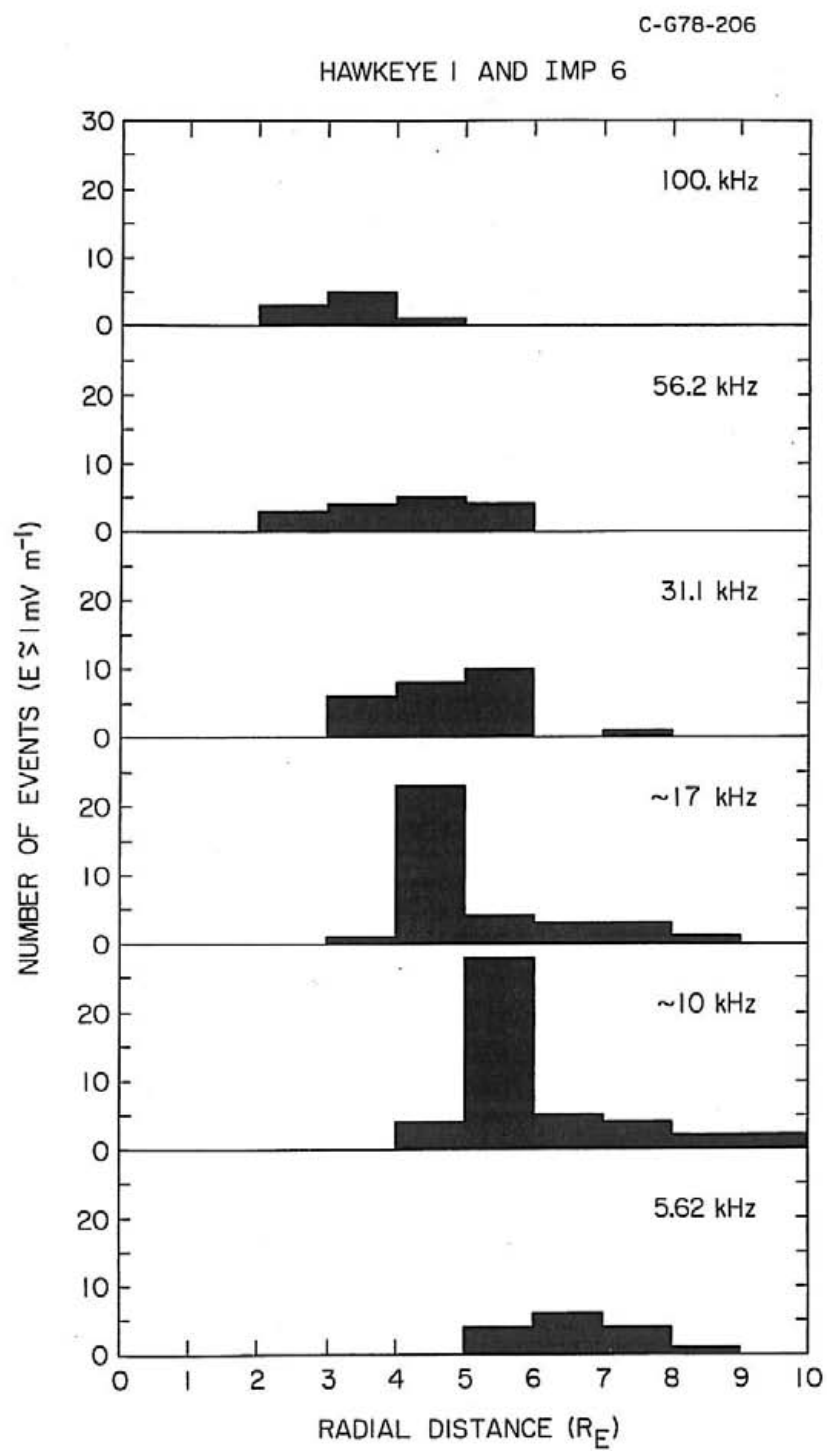


Figure 5

Figure 6

A display of plasma wave measurements of an intense wave event detected by Hawkeye 1 with a summary of polarization measurements superimposed over the data. The spin modulation seen in many of the features has been analyzed to determine the orientation of the wave electric field with respect to the geomagnetic field. The shaded regions are regions of frequency and time where all waves are polarized such that  $\vec{E} \parallel \vec{B}_0$ , consistent with the polarization of nonthermal continuum radiation. The unshaded region indicates frequencies and times, including the intense electrostatic event at 31.1 kHz, when waves with measurable polarization have electric fields oriented perpendicular to  $\vec{B}_0$ . This polarization unambiguously identifies  $f_{\text{UHR}}$  as the characteristic frequency of the intense waves (see text). The hatched region consists of whistler-mode turbulence.

D-G78-241-2

HAWKEYE I, ORBIT 286, JANUARY 31, 1976

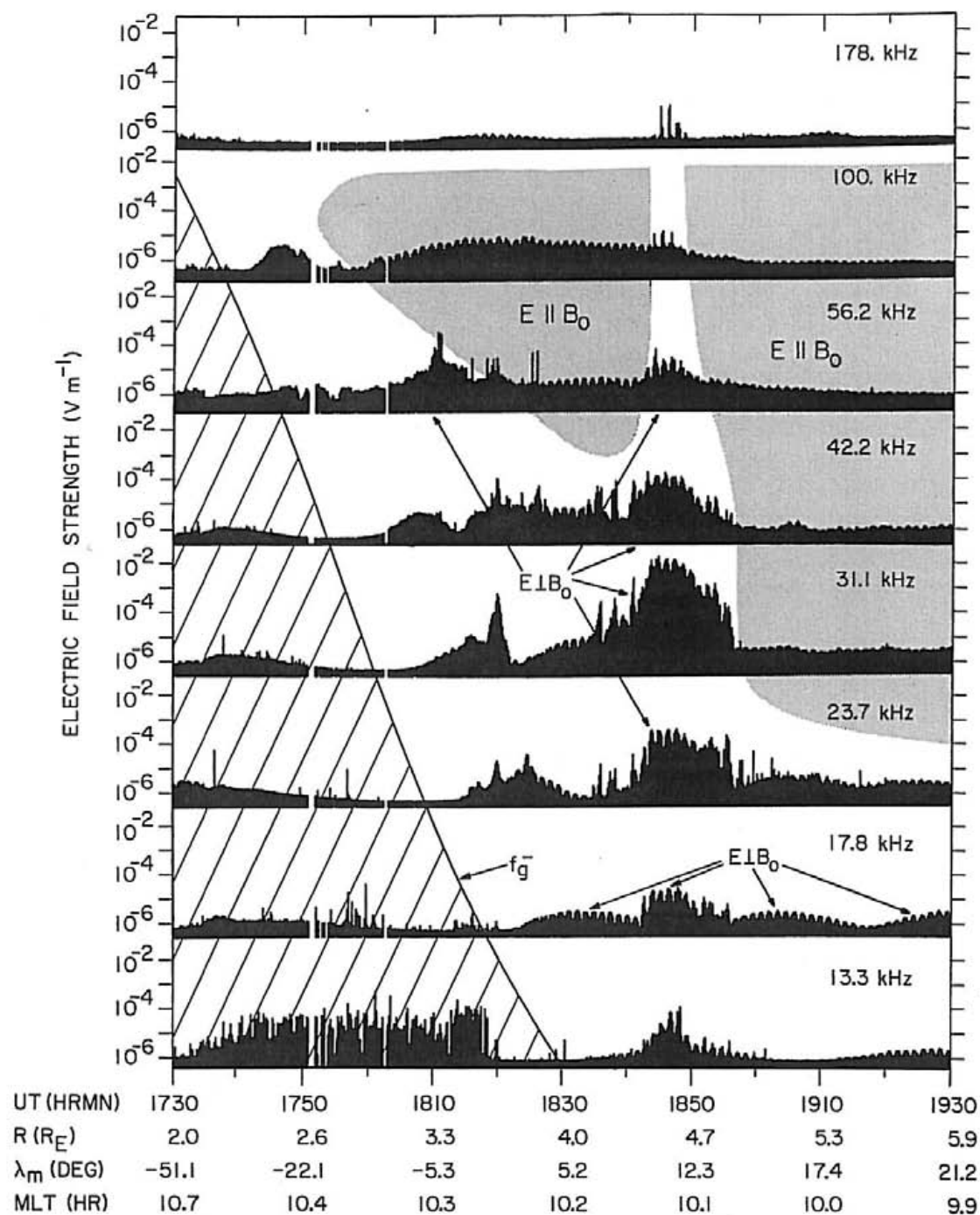


Figure 6

Figure 7 A display of plasma wave measurements of the same event shown in Figure 6, but overlaid with lines at  $f_g^-$  and the lower order  $(n + 1/2)f_g^-$  bands using the ordinate as a frequency scale. The values of  $f_g^-$  are calculated from the measured magnetic field provided by the magnetometer onboard Hawkeye 1. Notice that a large number of the features present in this complex region lie at or near the  $(n + 1/2)f_g^-$  harmonics. In particular, the intense event at 31.1 kHz lies directly at the  $7f_g^-/2$  harmonic.

D-678-293

HAWKEYE I, ORBIT 286, JANUARY 31, 1976

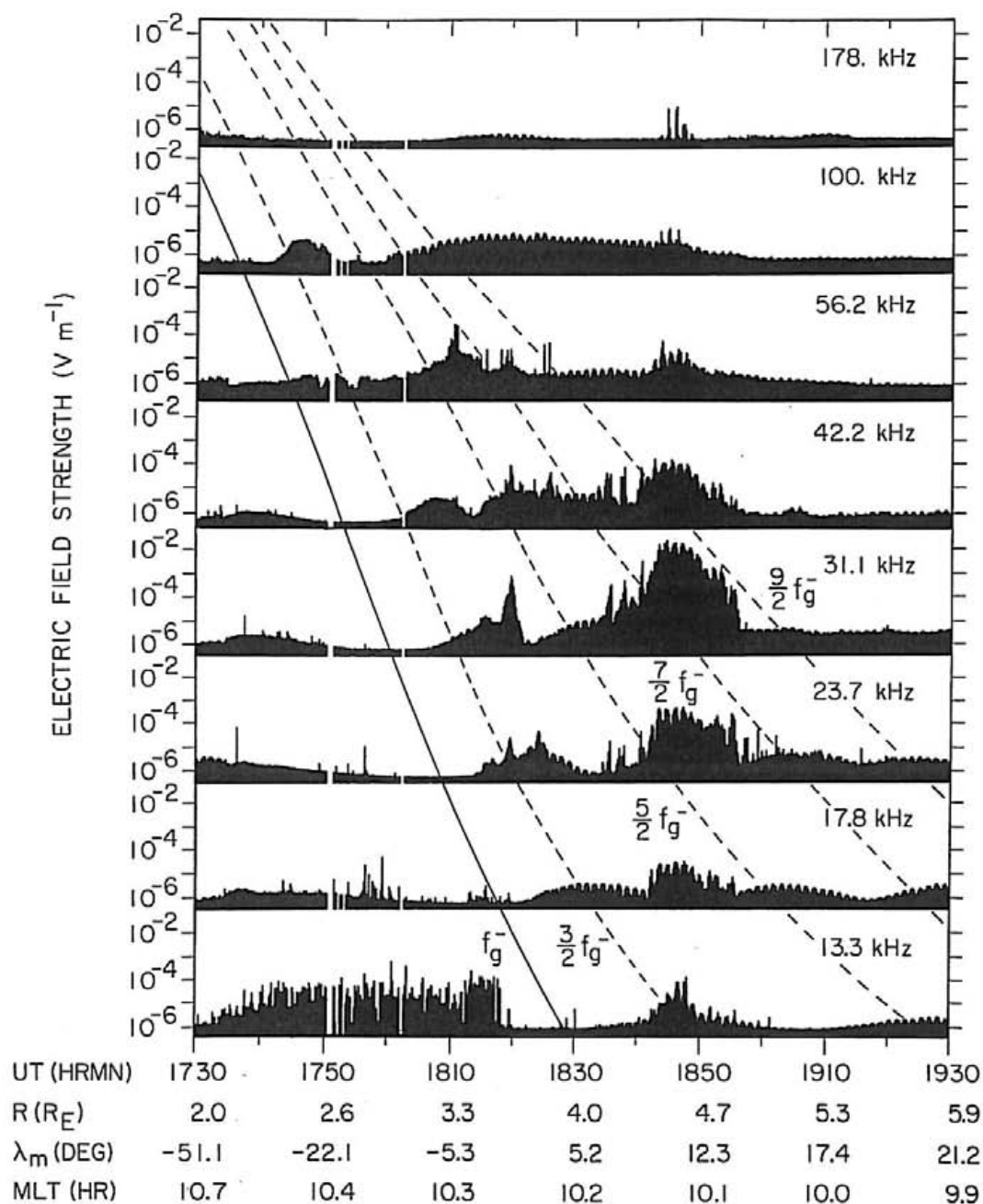


Figure 7



Figure 8      A demonstration of the variation of measured electric field strength as a function of  $\delta$ , the angle of the electric dipole antenna. The sketch in the upper portion of the figure demonstrates the relative orientation of the geomagnetic field,  $\vec{B}_0$ , the spacecraft spin axis,  $\vec{w}$ , and the electric field to be measured,  $\vec{E}_0$ . A general description of the polarization determination is found in Appendix A.

C-G78-III16

POLARIZATION DETERMINATION  
 HAWKEYE I ORBIT 286  
 JANUARY 31, 1976  
 1843:39 - 1849:36 UT

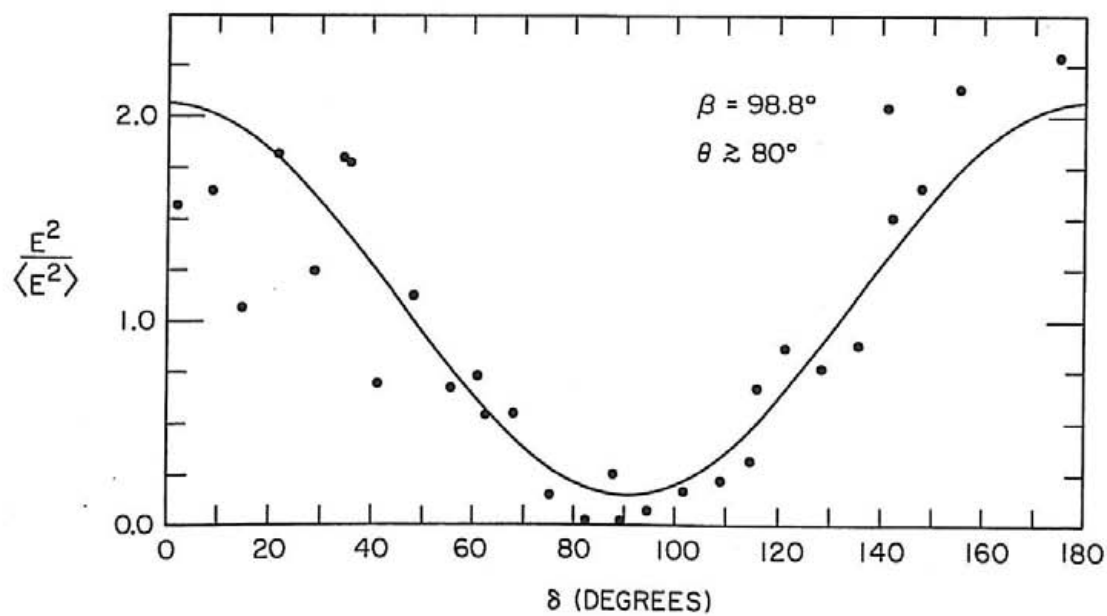
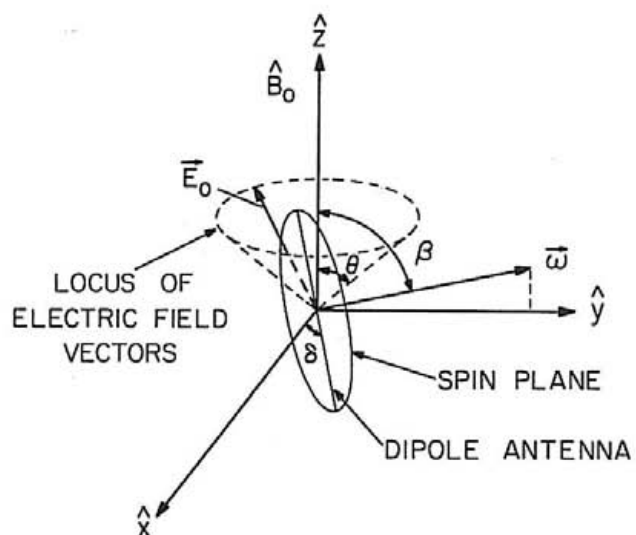


Figure 8

Figure 9      A high-resolution frequency-time spectrogram of intense electrostatic waves which occur not only at an  $(n + 1/2)f_g^-$  harmonic, but also near  $f_{UHR}$ . The gyrofrequency for this event is about 1.9 kHz and  $f_{UHR}$  (using the lower frequency cutoff of the continuum radiation for  $f_p^-$ ) is about 15.2 kHz.

A-G78-775-1

IMP 6 ORBIT 29  
JULY 11, 1971

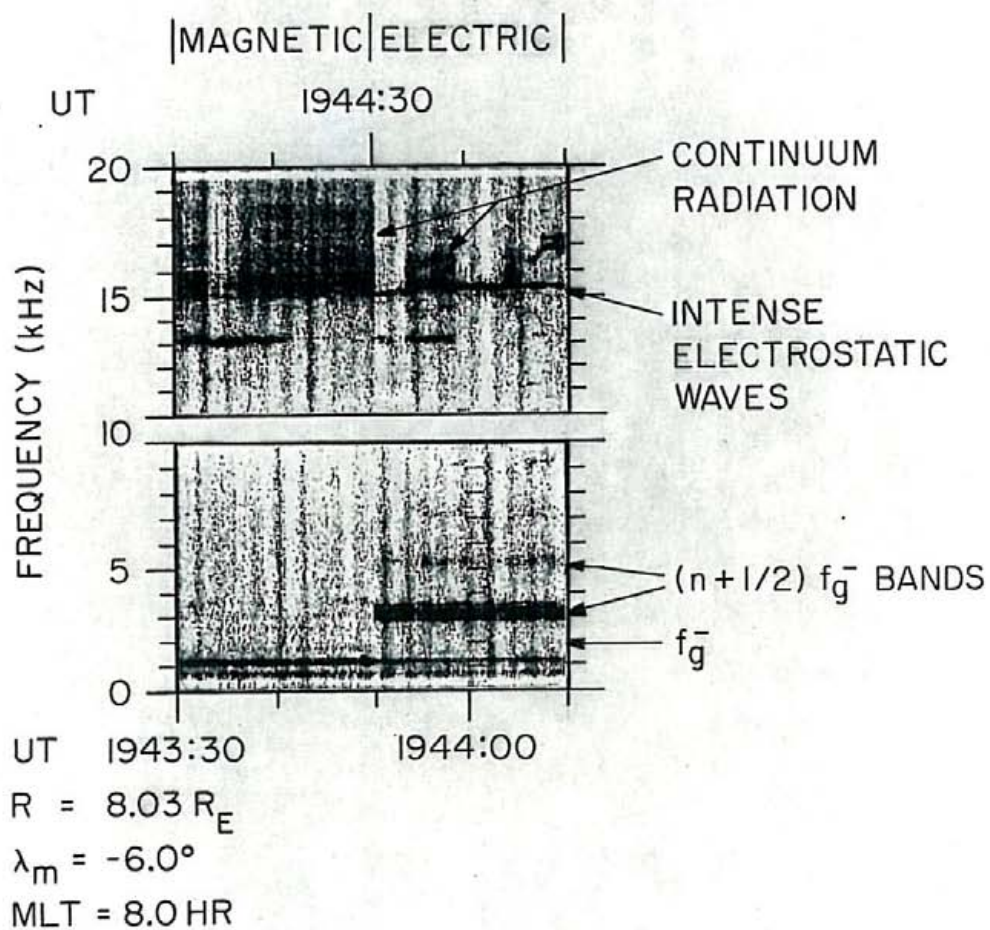


FIGURE 9

Figure 10 A high-resolution frequency-time spectrogram of intense electrostatic waves detected by the Hawkeye plasma wave receiver. Notice the banded structure of the event at frequencies greater than  $f_g^-$ . The waves are most intense when the electric dipole antenna is oriented perpendicular to the measured geomagnetic field. Hence, the wave electric field is nearly perpendicular to  $\vec{B}_0$ .

A-G78-112-2

HAWKEYE I, ORBIT 176, JUNE 12, 1975

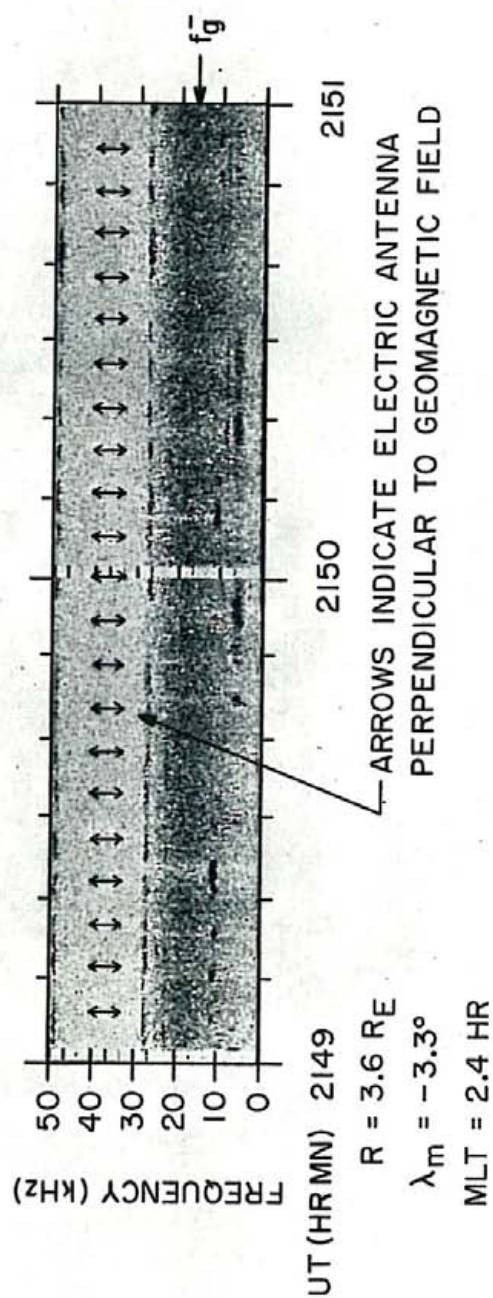


FIGURE 10

Figure 11      A high latitude intense electrostatic wave event to be compared to the plasma measurements shown in Plate 2. The time correlation between the presence of the intense waves in the 17.8-kHz channel and electron intensities near 1 keV is very good.

D-G78-292

HAWKEYE I, ORBIT 324, APRIL 23, 1976

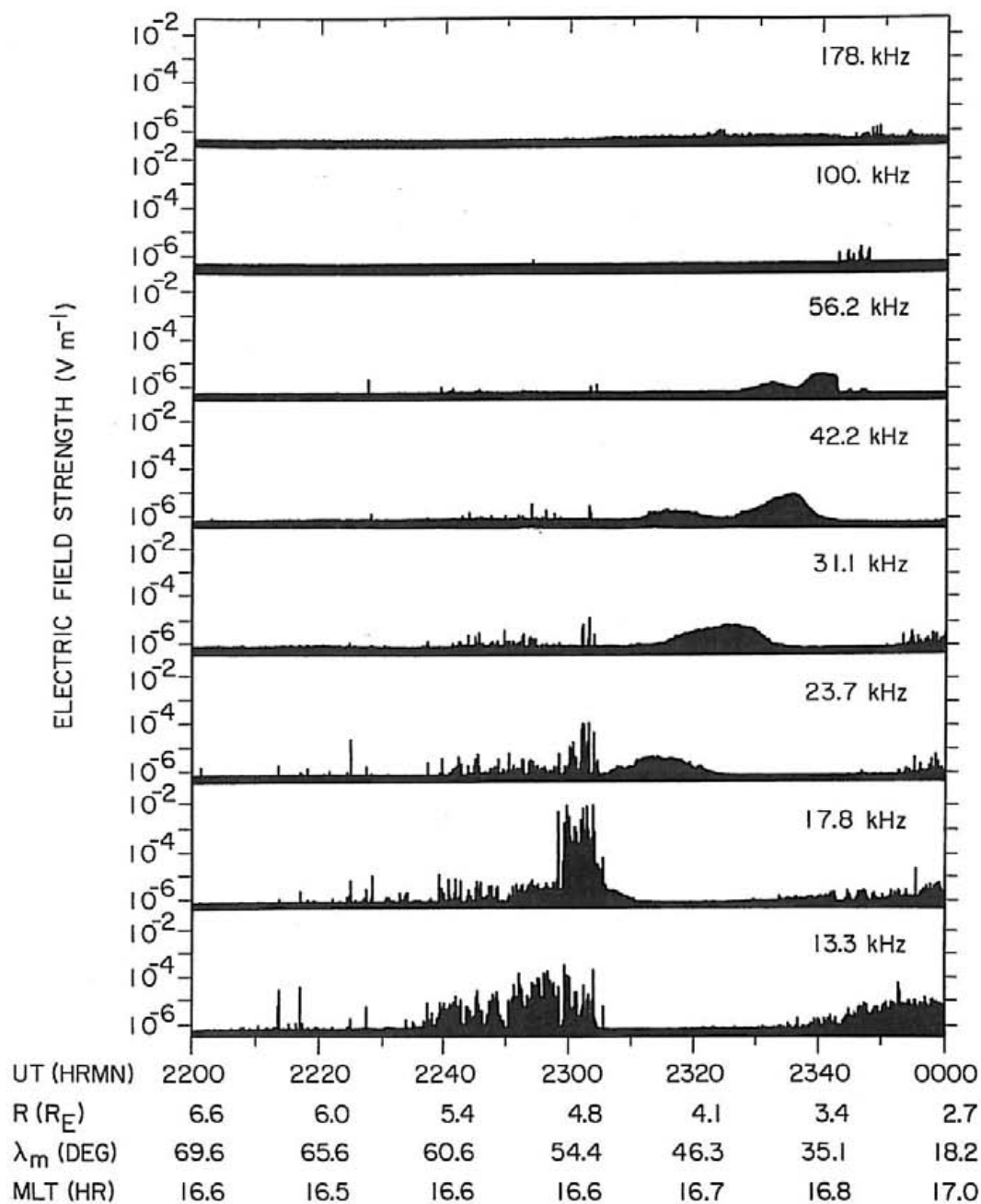


Figure 11



Figure 12      An intense electrostatic wave event at 100 kHz located near the magnetic equator. The energy-time spectrogram obtained from plasma measurements during this event is shown in Plate 3.

D-G78-831

HAWKEYE I, ORBIT 205, AUGUST 15, 1975

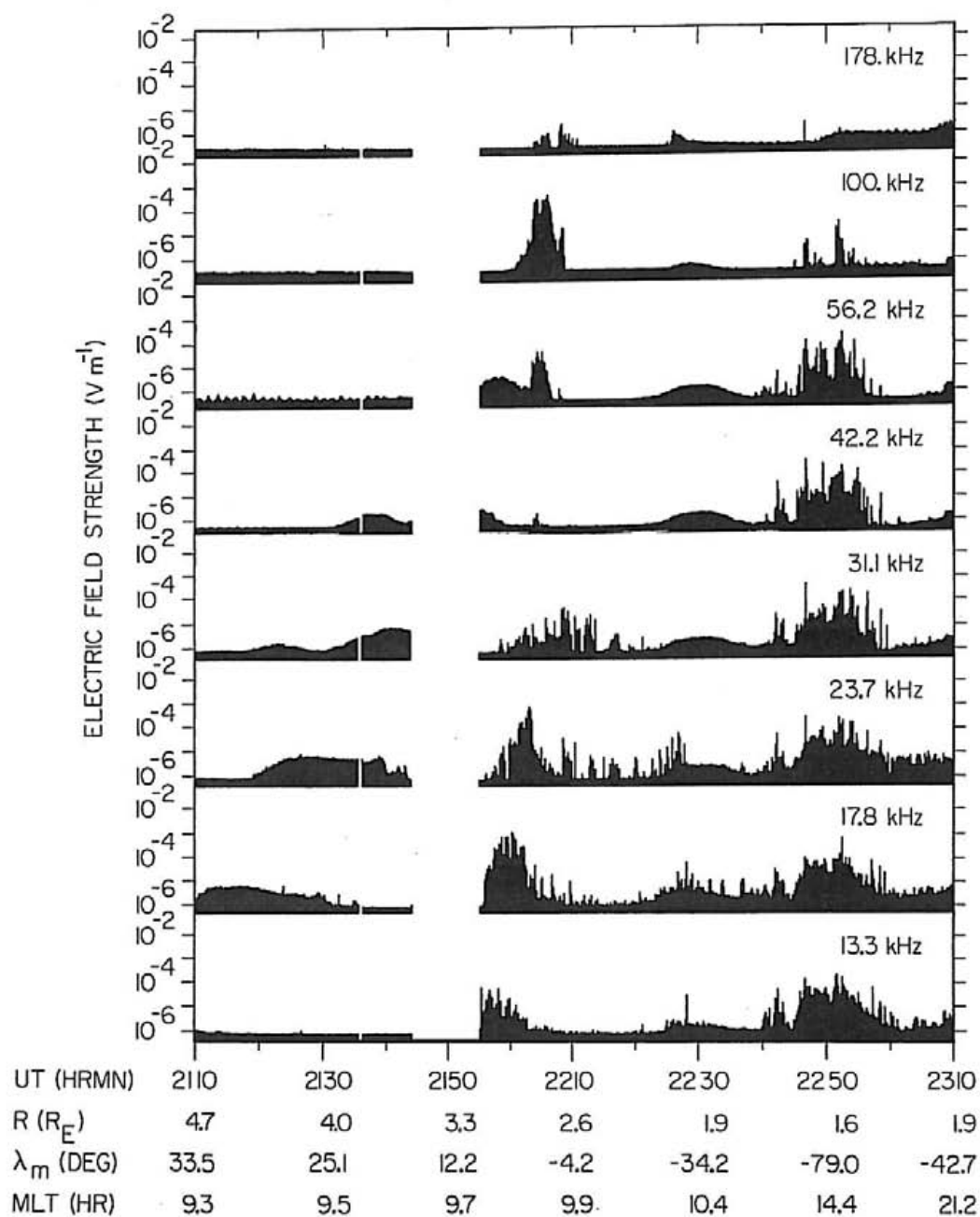


Figure 12

Figure 13      The electron velocity distribution measured during the intense wave event illustrated in Figure 14. Notice the loss cone at small pitch angles, and the temperature anisotropy. The area to the left of the dashed line through contours of constant  $f(v_{\perp}, v_{\parallel})$  is a region of small  $v_{\perp}$  for which the plasma analyzer responses are  $< 100 \text{ counts (sec)}^{-1}$ .

C-678-936-1

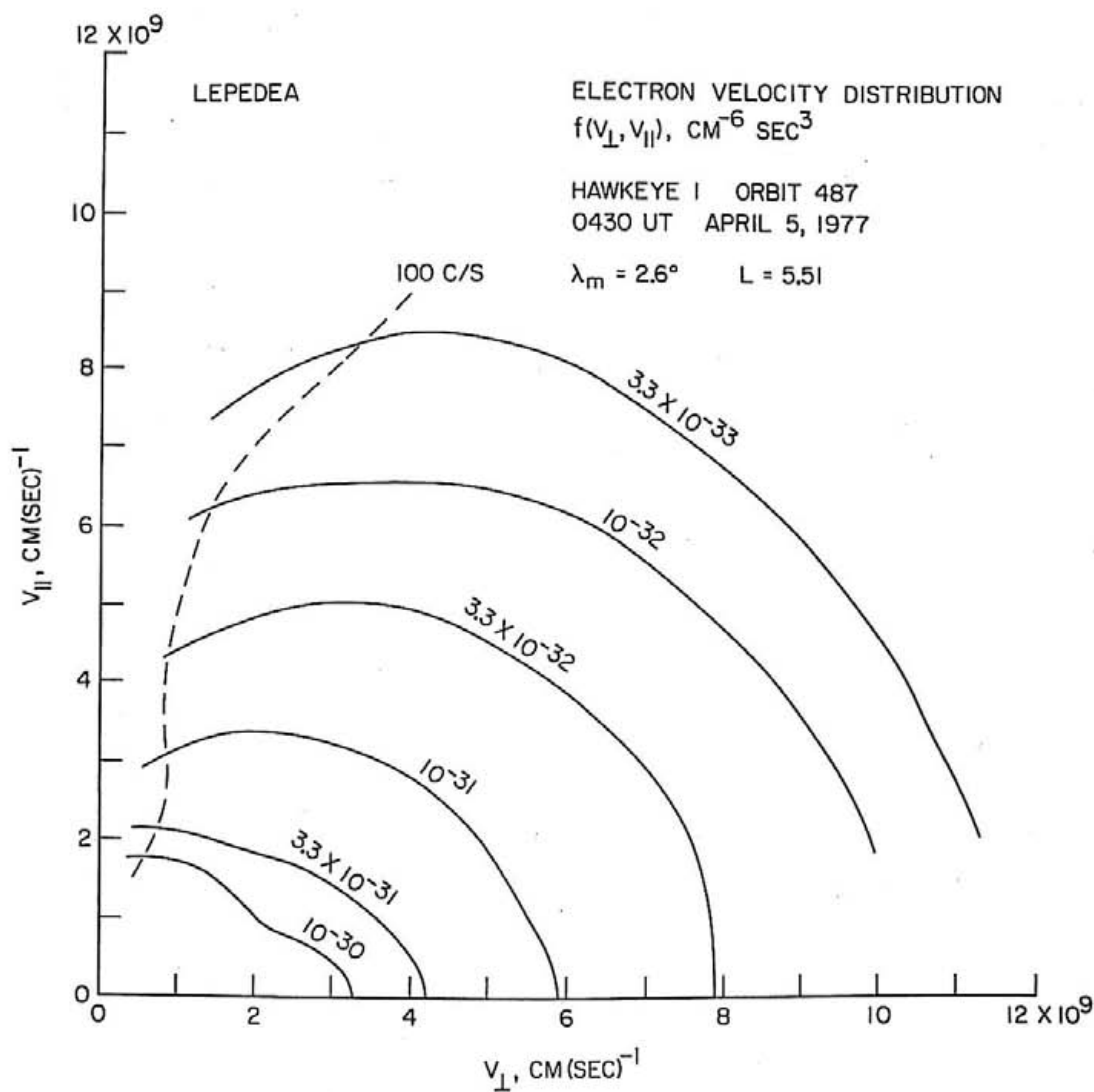


Figure 13

Figure 14      An electrostatic wave event for which an electron velocity distribution has been measured and shown in Figure 13. The intense signal of interest occurs in the 17.8-kHz channel between about 0415 and 0435 UT.

D-G78-871

HAWKEYE I, ORBIT 487, APRIL 5, 1977

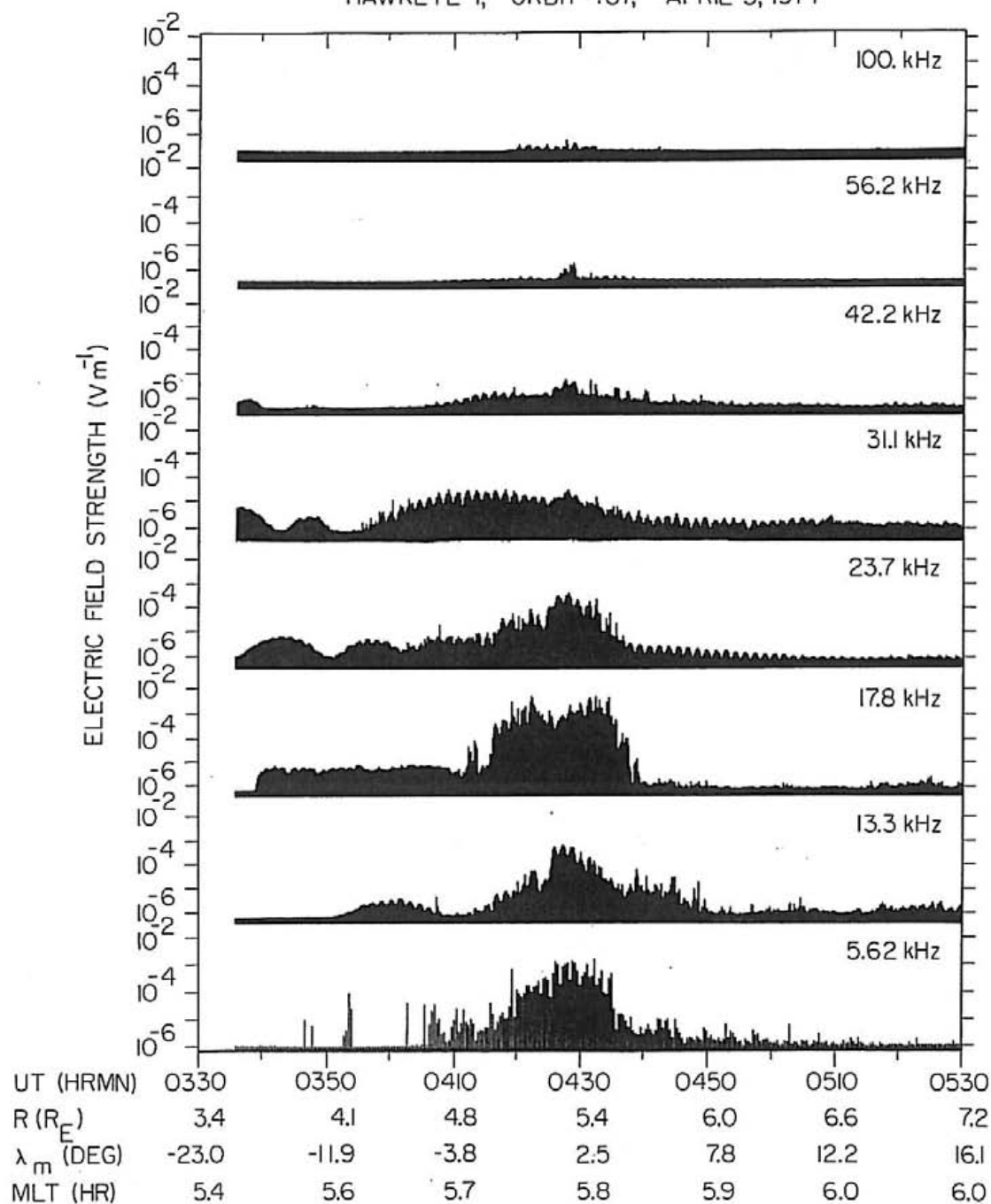


Figure 14

Figure 15      An electron velocity distribution for the event shown in Figure 16 which shows a very weak loss cone and also is anisotropic. The dashed line is the 100 count (sec)<sup>-1</sup> contour.

C-678-935-1

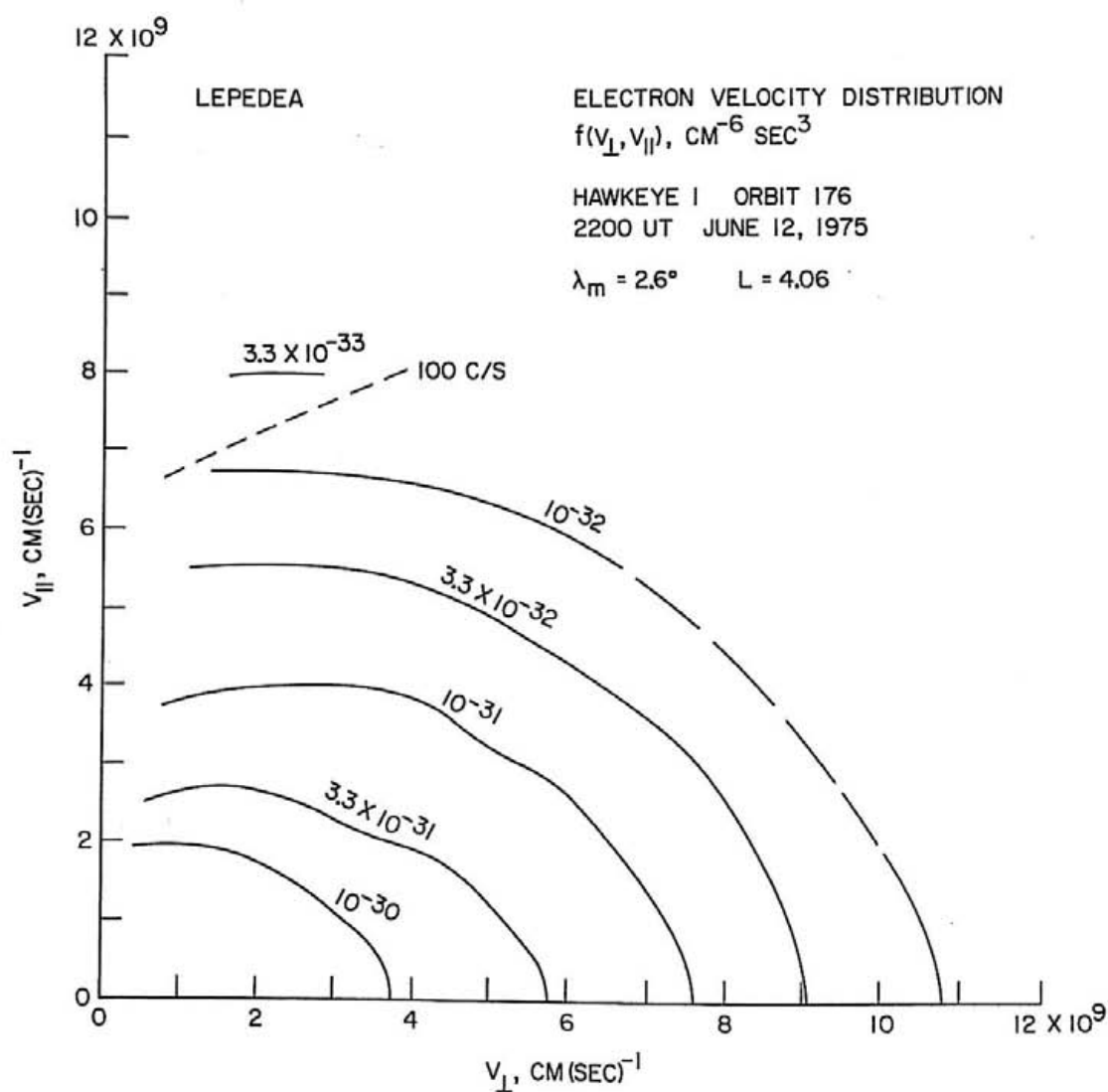


Figure 15



Figure 16      An electrostatic wave event for which an electron velocity distribution has been measured and shown in Figure 15. A high resolution frequency-time spectrogram obtained during this event is shown in Figure 10.

D-G78-239

HAWKEYE 1, ORBIT 176, JUNE 12, 1975

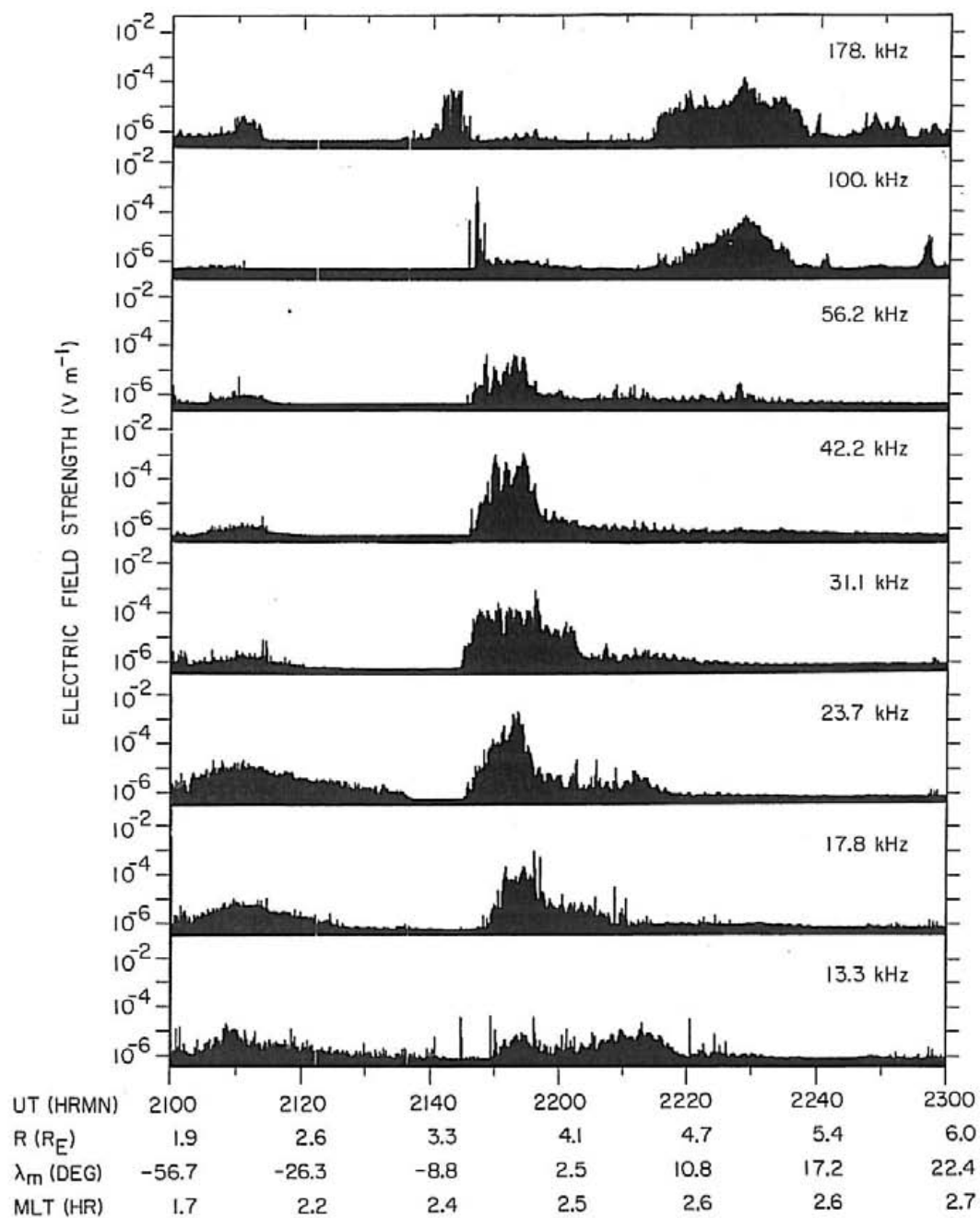


Figure 16

Figure 17      A model loss-cone distribution (solid lines) and the measured response of a detector with finite width (dashed lines). Notice the qualitative similarities between the dashed contours and the contours at small pitch angles shown in Figures 13 and 15.

C-G78-998-1

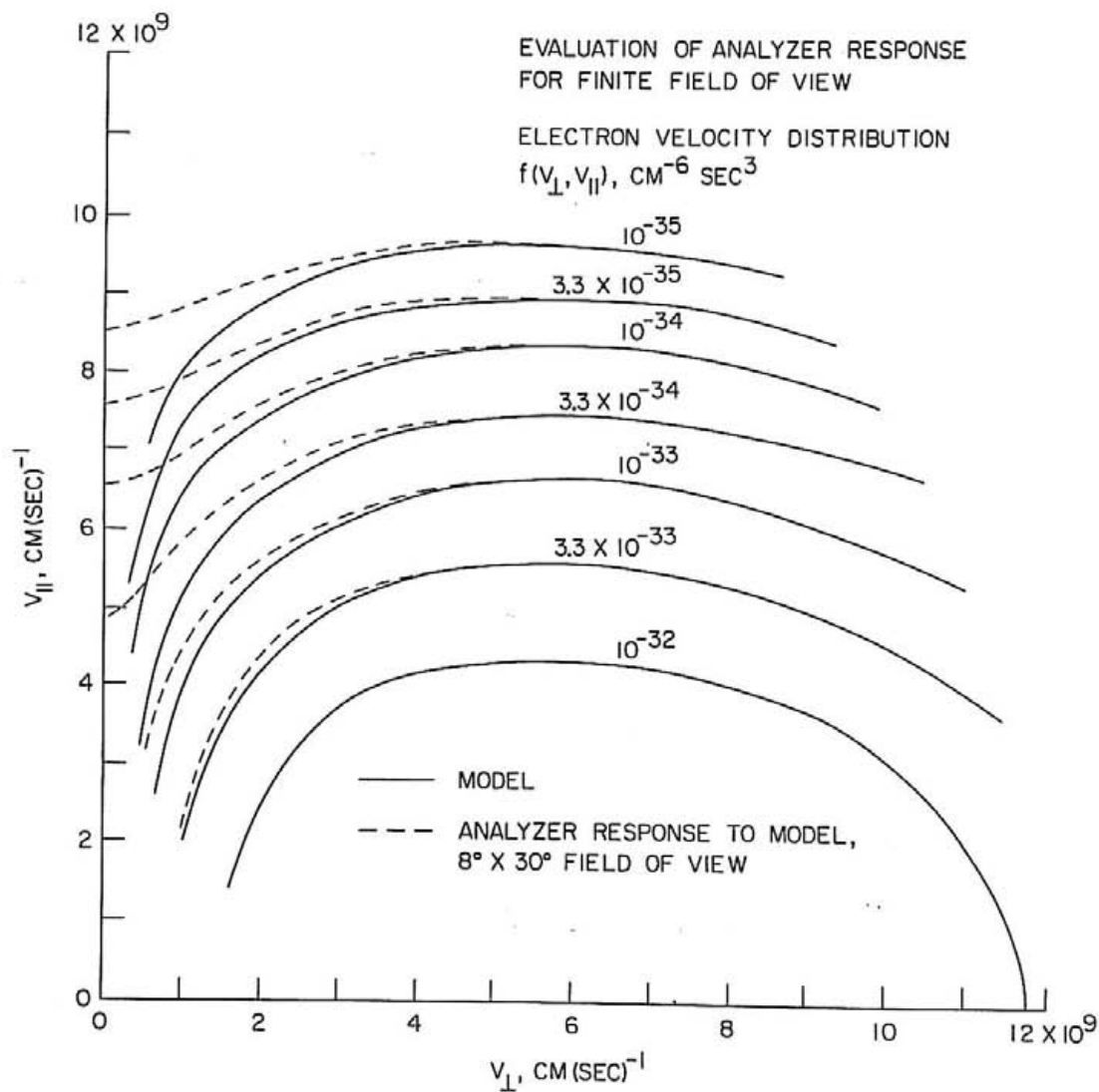


Figure 17

Figure 18      An electron distribution function exhibiting a weak loss-cone distribution and a temperature anisotropy. The wave event corresponding to this distribution function is shown in Figure 19. The dashed line is the 100 counts (sec)<sup>-1</sup> contour.

C-G78-934-1

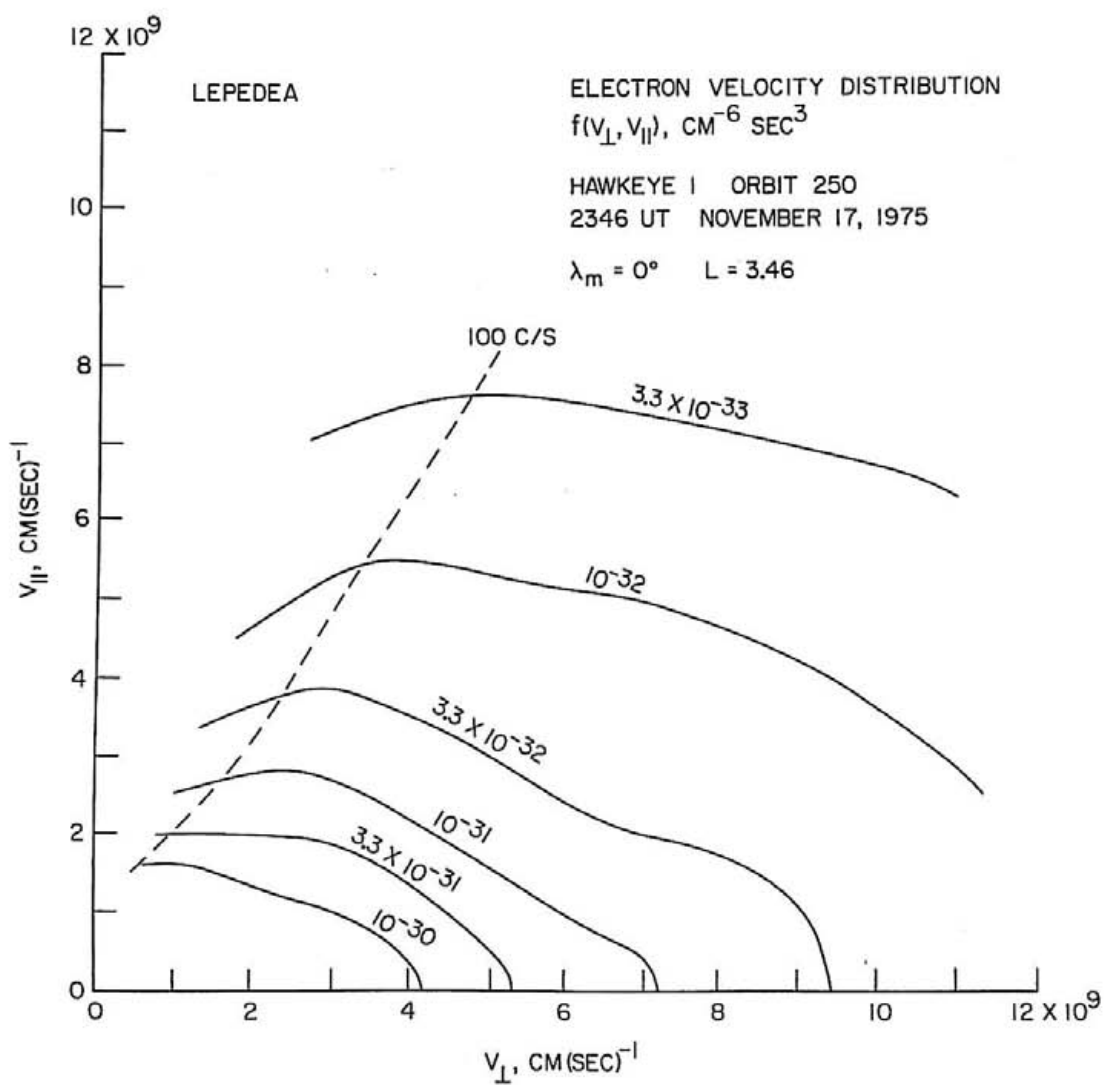


Figure 18

Figure 19      The intense electrostatic wave event for which an electron velocity distribution has been measured and shown in Figure 18. This event, near 2345 UT in the 100-kHz channel, exhibits extreme fluctuations in amplitude on a time scale of minutes.

D-678-838

HAWKEYE 1, ORBIT 250, NOVEMBER 17, 1975

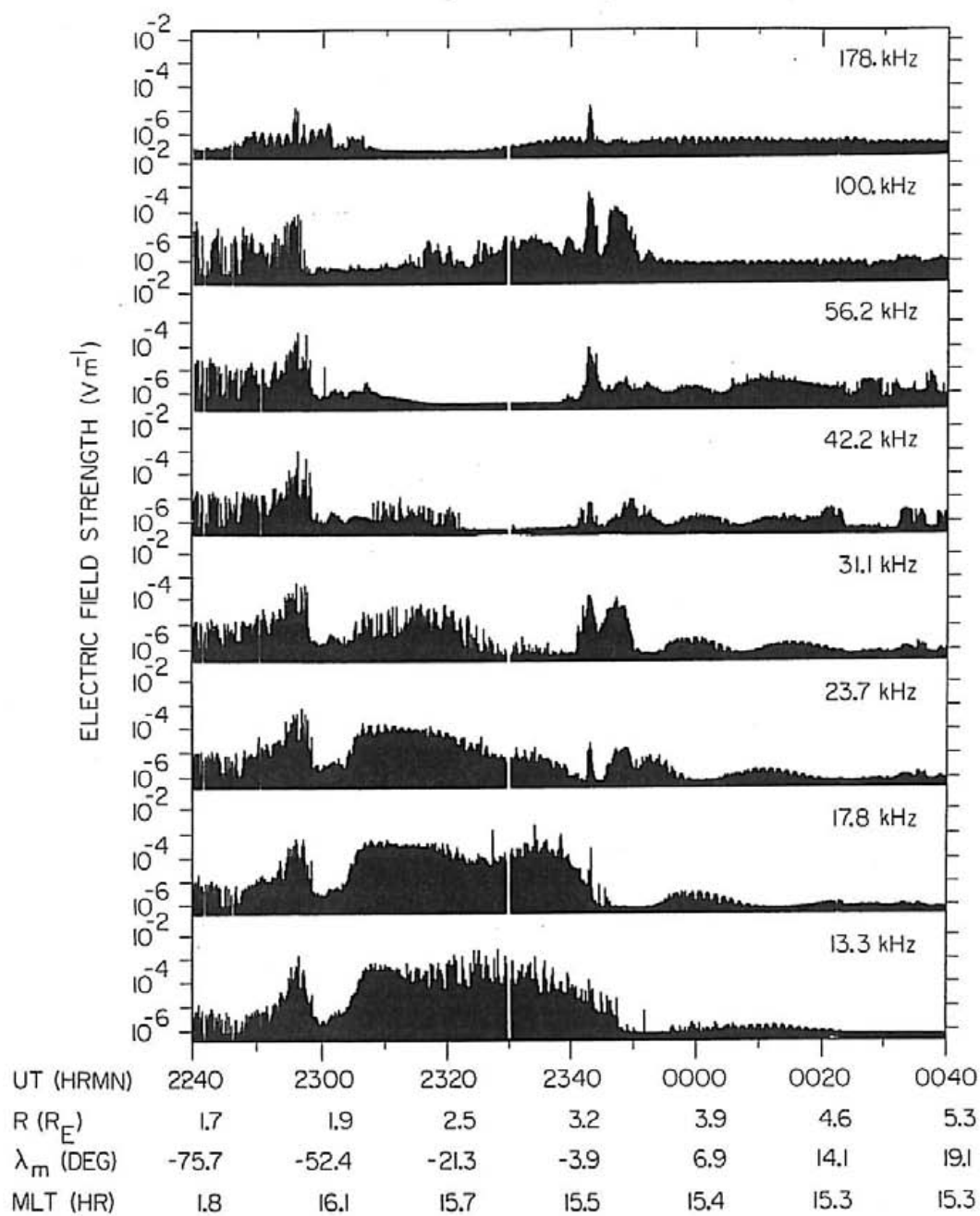


Figure 19



Figure 20      The electron distribution function for the wave event shown in Figure 12. The dashed lines are contours of 100 and 50 counts (sec)<sup>-1</sup>. This distribution function is, perhaps, suggestive of a bump-on-tail distribution at  $v_{||} = 0$ . The function also shows a temperature anisotropy.

C-678-933-2

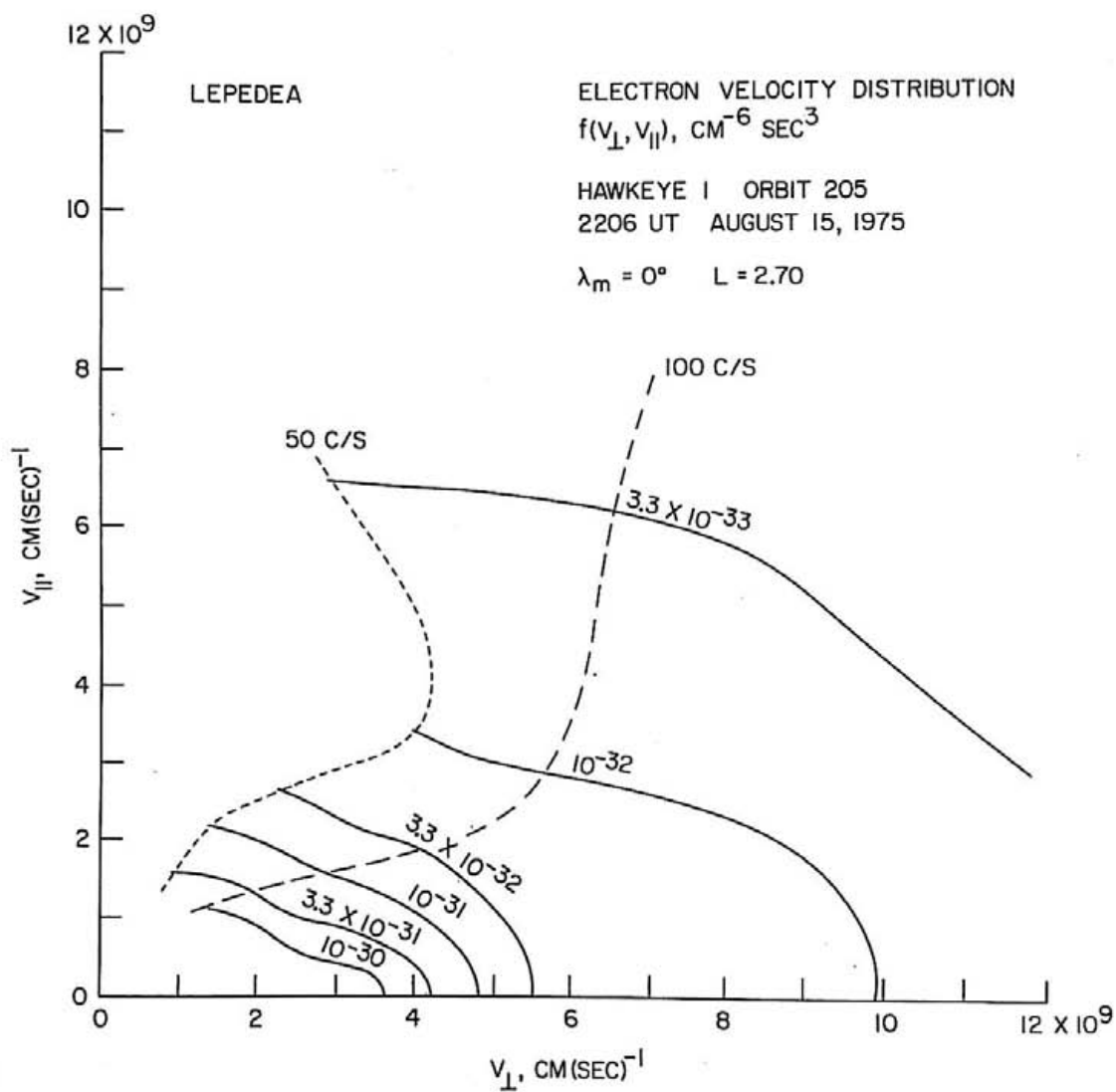


Figure 20

Figure 21      Regions of nonconvective instability for the first four harmonic bands above  $f_g^-$ . Notice that for large ( $\geq 1.5$ )  $n_c/n_h$  and sufficiently large  $f_{UHC}$  a single band (the band including  $f_{UHC}$ ) can become nonconvectively unstable.

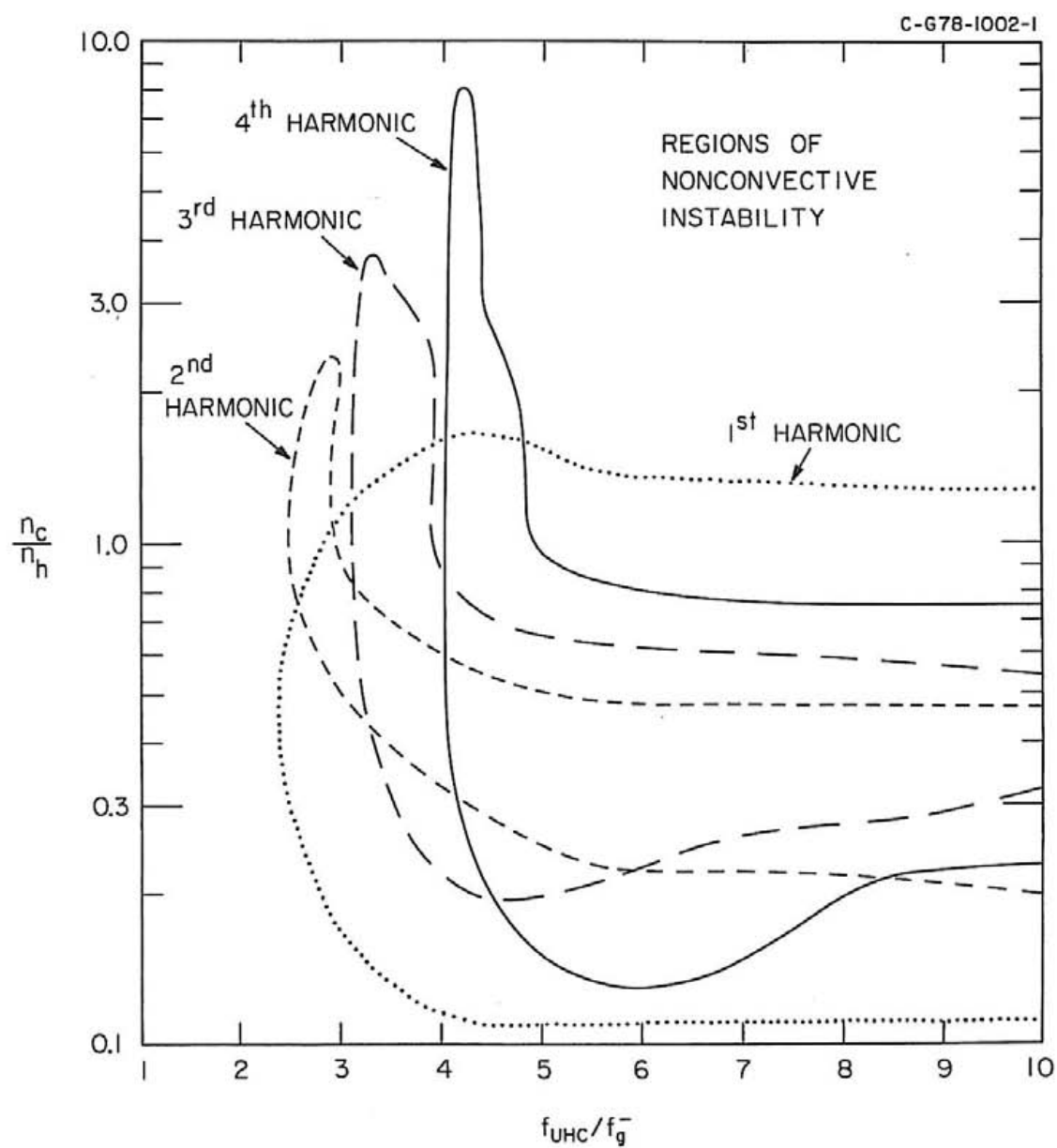


Figure 21

Figure 22      The electron velocity distribution averaged over pitch angles  $70^\circ < \alpha \leq 90^\circ$  during the intense electrostatic wave event illustrated in Plate 5. Notice that there are two features which might be suggestive of a free energy source for the waves in Plate 5. The features persist from  $\alpha \approx 20^\circ$  through  $\alpha \approx 160^\circ$ .

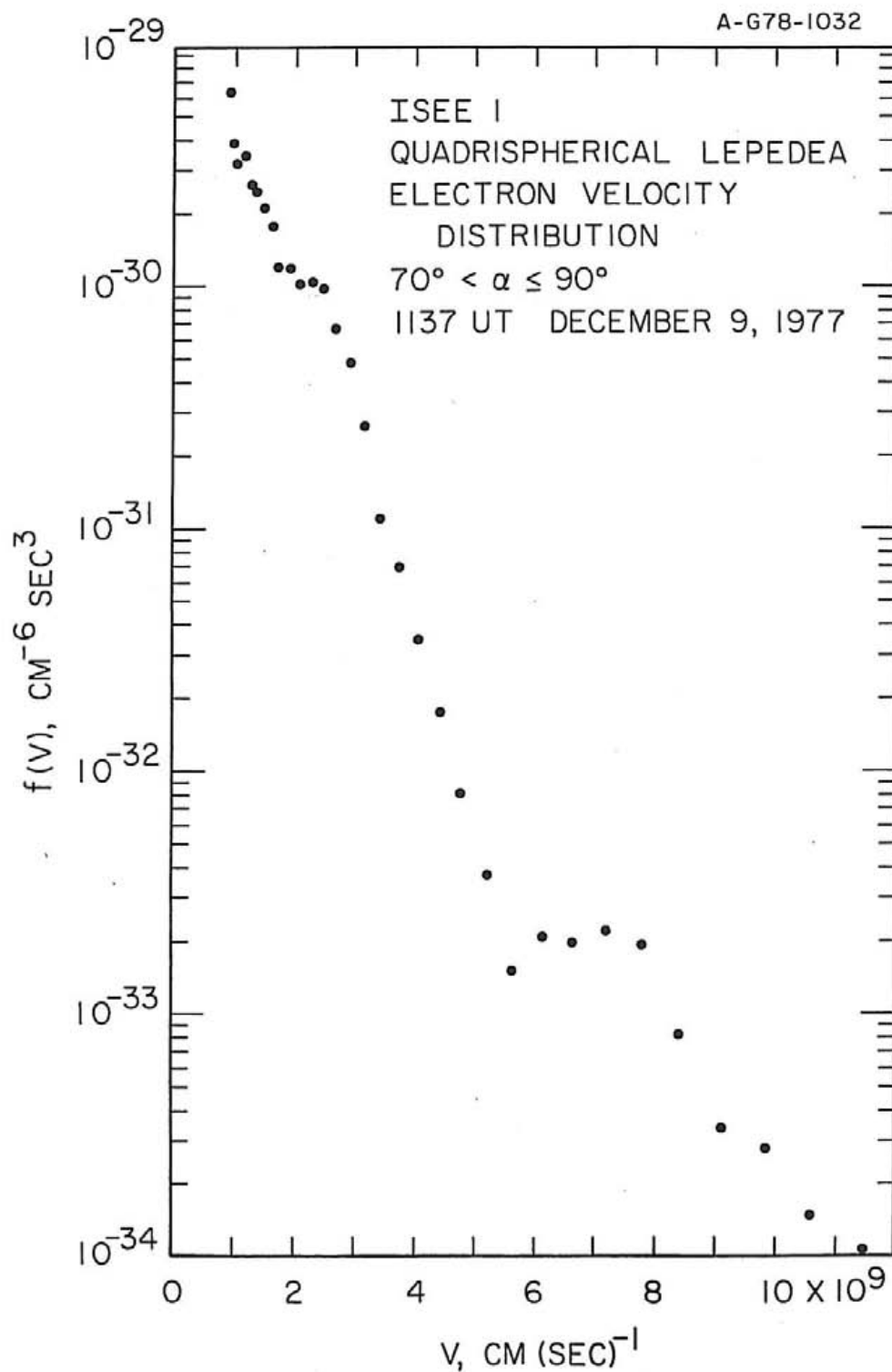


Figure 22

Figure 23      A demonstration of the qualitative agreement between linear instability theory and observations of intense electrostatic waves near  $f_{UHR}$ . The upper panel is the measured wave spectrum during the intense wave event shown in Plate 1. Notice the weak growth in the lower three bands and the intense peak in the fourth band. The lower panel shows calculations of the maximum spatial growth rate as a function of frequency when  $f_{UHC}$  is in the fourth band. Notice there is relatively weak convective growth in the lower 3 bands, but the fourth band is nonconvectively unstable. The growth rates shown near the peak of the fourth band are only representative since for a nonconvective instability  $v_g$  goes to zero and  $K_i$  goes to infinity.

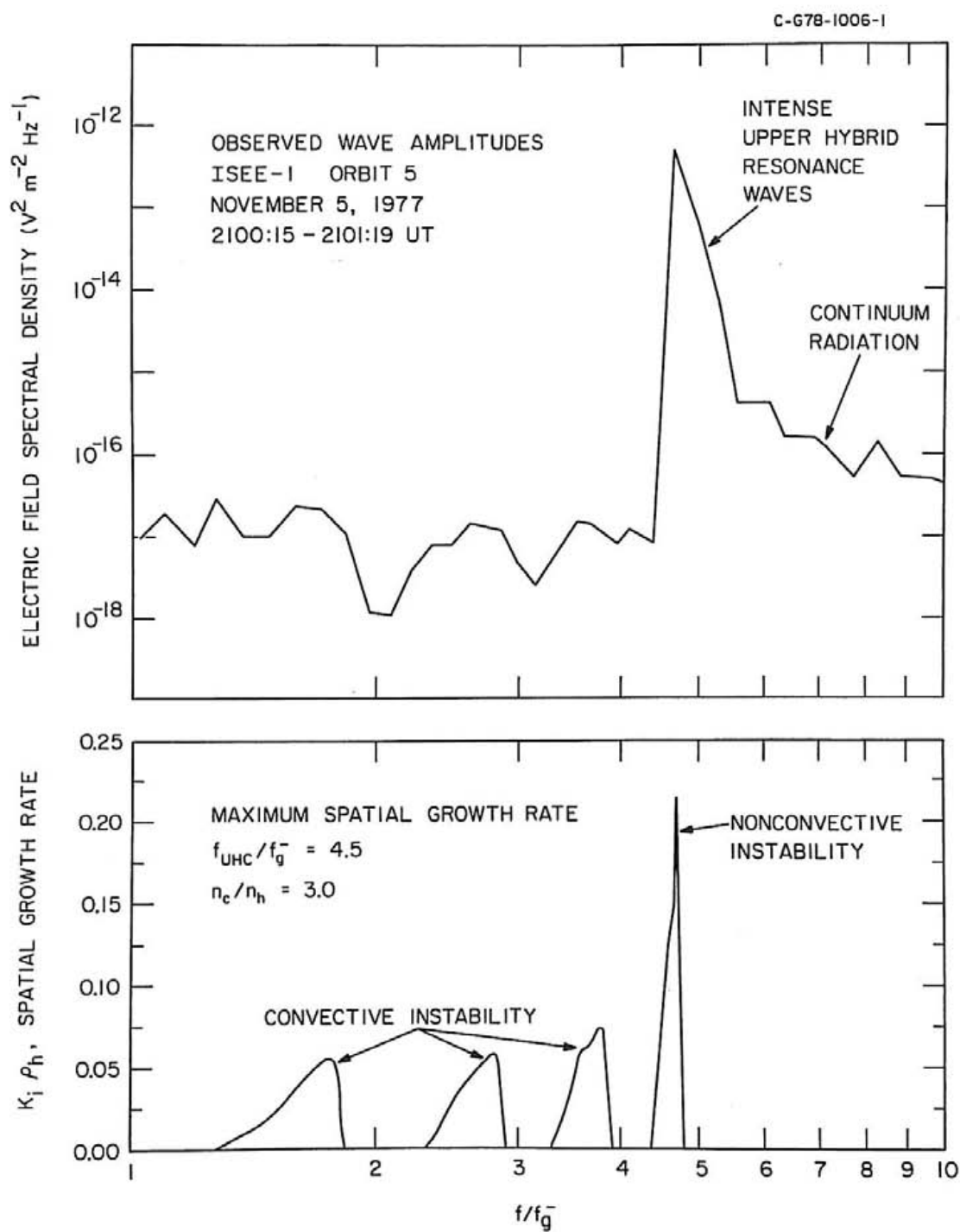


Figure 23



Figure 24 A demonstration of an intense electrostatic wave event as a local, compact source of nonthermal continuum radiation. Power flux plotted as a function of radial distance from the earth in the center panel does not show the  $R^{-2}$  dependence expected for a source centered at the earth. However, the plot of power flux as a function of the distance from the intense event centered at  $4.3 R_E$  shows a definite  $(R-R')^{-2}$  dependence.

D-G78-161

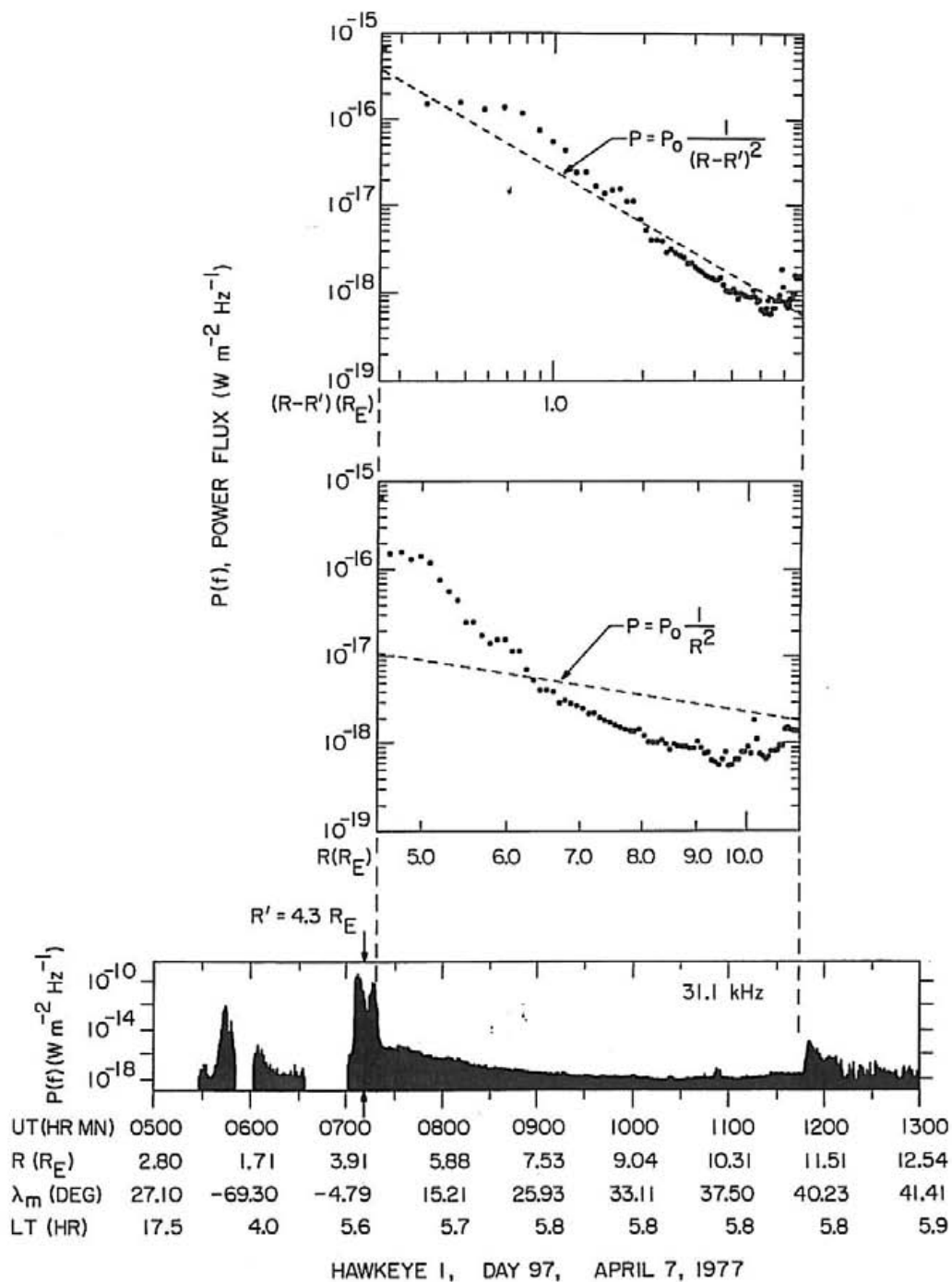


Figure 24